STUDY OF NANOSTRUCTURED GLASS SURFACES FOR PHOTOVOLTAIC APPLICATIONS

SON JAE SUNG

(*B. Sc. Sungkyunkwan University, Korea*)

A THESIS SUBMITTED FOR
THE DEGREE OF DOCTOR OF PHILOSOPHY

DEPARTMENT OF ELECTRICAL AND
COMPUTER ENGINEERING

NATIONAL UNIVERSITY OF SINGAPORE

2013

DECLARATION

I hereby declare that the thesis is my original work and it has been written by me in its entirety. I have duly acknowledged all the sources of information which have been used in the thesis.

This thesis has also not been submitted for any degree in any university previously.

Son Jaesung

1 August 2013

ACKNOWLEDGEMENT

At the end of the long journey, first and foremost, I praise and thank to the God for preparing all the ways throughout my research works and making me complete the long journey.

I would like to express my sincere gratitude to my supervisor Professor Yang Hyunsoo for the continuous support in my Ph.D study and research and for his patience, motivation, enthusiasm, and immense knowledge. His invaluable guidance helped me stay committed to my researches and writing of this thesis. I am grateful to Professor Charanjit Singh Bhatia and Professor Aaron Danner for their encouragements, insightful comments, and hard questions. Without their great guidance, my doctoral research would not have been the same. I remember the awkward moment when I gave my first English presentation in my life in front of them. They have endured and waited for me to grow up. I hope that they have enjoyed past years watching me to grow up step by step.

I thank my lab-mates in the Spin and Energy Lab for stimulating discussions, for many sleepless nights being together, and for all the fun we have had during the last four years. I want to thank Robert Jung for his enthusiastic help and for sharing of his life experience. He taught me the great value of diligence, which is the best lesson I have learnt from him. My special thanks go to COE staffs, Mr. Tan and Ms. Musni for their kind help and sharing their invaluable experiences in frequent collaborations. I am deeply indebted to my friends in my church and NUS, who always encouraged me and prayed for me whenever I was frustrated and depressed.

Last but not the least I want to thank my family for their love and support. My sincere thanks and appreciation go to my parent for supporting me spiritually throughout my life with their endless love and praying for me all the time. I thank my brother who has given me spiritual comfort as well as financial supports. Lastly, I would express my deepest gratitude to Amanda Woori Kim for her unconditional supports. Any words of acknowledgement are not enough to express my deepest gratitude to her. Her continuous love, support, encouragement, and prayer have allowed me to pursue my way.

TABLE OF CONTENTS

ABSTRACT

Learning from nature will give us important inspiration to develop new techniques to construct artificial advanced materials. These approaches of designing novel materials are called “biomimetics”. It has been developed rapidly in the past decade due to advancements in nanotechnology. A large area of biomimetic research deals with functional micro- and nano- structures for water repellence, self-cleaning, energy conversion, and antireflection through the fabrication and functionalization of the biomimetic artificial nanotextured surface.

In this thesis, we have mostly studied the antireflective property and self-cleaning effect of a nanotextured glass surface and its applications for photovoltaic devices. Anodized aluminum oxide (AAO) membrane, which is an attractive nanotemplate for low-dimensional structures, is utilized to form the nanopores due to its excellent dimensional controllability. The multifunctional properties are characterized not only in indoor but also outdoor environments for long-term.

First, numerical studies have been conducted to confirm the effect of nanostructures on optical properties and find optimal dimensions of the nanostructures. Based on the simulation studies, the antireflective glasses are fabricated by using the AAO membrane as an etching mask. We demonstrate an enhancement of optical transmission by creating randomly distributed nanoholes in a glass surface. Moreover, the V-shaped holes with a sub-100 nm diameter enhance the optical transmission exhibiting broadband and omnidirectional antireflection properties.

In addition to the enhanced optical properties, the self-cleaning effect of nanotextured superhydrophilic surfaces has been studied. Various hydrophobic, hydrophilic, superhydrophobic, and superhydrophilic glasses are evaluated by monitoring the variation of water contact angle, optical transmittance, and photovoltaic performance under outdoor conditions for 12 weeks. Our results show a nanopatterned superhydrophilic glass without surface chemical treatment exhibits more efficient self-cleaning and antireflective effects, leading to only 1.39% of drop of solar cell efficiency

during an outdoor test, while the solar cells with bare glass packaging and fluorinated superhydrophobic packaging show 7.79% and 2.62% of efficiency drop, respectively. Unlike other methods where the chemical coatings play a main role for the self-cleaning effect, our non-coated superhydrophilic glass system will be particularly useful for practical outdoor applications, in which both the self-cleaning and antireflective effects are of concern, and where degradation of a chemical coating over time will not be of concern.

Subsequently, we have demonstrated a modified anodizing method to fabricate an antireflective surface on a large area glass. The difficulty of thin film anodization on an insulating substrate is overcome by introducing grid line contacts, leading to complete anodization of the 6×6 inch^2 aluminum films on glass substrates. The transferred nanoholes on the glass substrate exhibit the broadband and omnidirectional antireflective properties. We have showed the 6 inch textured glass improves the short circuit current of a 5 inch solar cell by 11.34% than that of the planar glass cell, and increases the power conversion efficiency from 7.9% to 8.57%. Moreover, the enhanced optical properties continue for long term under outdoor environments. The proposed anodizing method can be an alternative nanolithography for fabrication of large area nanostructures.

Along with increasing concerns for the environment and renewable energy, our study has focused on and contributed to the photovoltaic applications. We have shown that the smart surface can work well in real outdoor applications for long-term. Moreover, the technique for large area fabrication can be considered as a reliable candidate for mass production after fine tuning of the texturing processes.

LIST OF TABLES

LIST OF FIGURES

LIST OF ABBREVIATIONS

AAO : anodized aluminum oxide

AR : antireflection

CA : contact angle

DTMS : decyltrimethoxysilane

EDX : energy-dispersive X-ray spectroscopy

EVA : ethylene vinyl acetate

FAS : fluoroalkyl silane

FDTD : finite difference time domain

HDFS : heptadecafluoro-1,1,2,2-tetrahydrodecyl-trichlorosilane

HDTMS : hexadecyltrimethoxysilane

ICP-RIE : inductively coupled plasma-reactive ion etching

IPA : isopropyl alcohol

I_{sc} : short circuit current

LED : light emitting diode

LIL : laser interference lithography

NIL : nanoimprint lithography

NSL : nanosphere lithography

OTS : octyltrimethoxysilane

PDMS : polydimethylsiloxane

PFOS : perfluorooctyl tricholorosilane

PFPE : perfluoropolyether

PFTS : 1H,1H,2H,2H-perfluorodecyl trichlorosilane

PML : perfect matched layer

RIE : reactive ion etching

SAM : self-assembled monolayer

SEM : scanning electron microscopy

TE : transverse electric

TM : transverse magnetic

TMES : trimethylethoxysilane

V_{oc} : open circuit voltage

η_{eff} : power conversion efficiency

Chapter 1: Introduction

1.1 Nanotechnology in nature

Generally, nanotechnology deals with structures, materials, or devices with a dimension on nanoscale. The transition into the "nano-world" is described as "much more than just an ongoing miniaturization", because the world has its own rules within which quantum effects become relevant, which has no analogies in the "micro-world".[1] Nanotechnology is very diverse, ranging from extensions of conventional device physics to completely new approaches for developing new materials within nanoscale. Thus, nanotechnology is able to create many new devices and materials with a vast range of applications, such as medicine, electronics, biomaterials, and energy production, overcoming the barriers of microtechnology. For instance, the discovery of quantum effects in semiconductors enables to achieve highly integrated MOSFET circuits as well as development of optoelectronic devices such as light emitting diodes (LEDs) and solar cells, leading to innovation in human's life.

Before recent emerging of the nanotechnology, the "nano-world" exists in nature. Nature has gone through a numerous process of trial and error to refine its living organisms. Humans have been looking for the optimized nature to solve our problems and take inspiration from it. Recently there has been a substantial progress in mimicking nature which may pave the way to many practical applications with the advance of fabrication techniques at nanoscale.

Some special "nano" features in biology have received intense attention as shown in Figure 1.1. For example, the attachment mechanism of geckos,[2] the self-cleaning effect of lotus leaves,[3] the superhydrophobic forces exerted by a water strider's legs,[4] and many other natural phenomena are all related to unique nanostructures on surfaces.[5] Not only chemical phenomena of the previous cases, but also unique optical properties have been also discovered from the nature. In Figure 1.2,

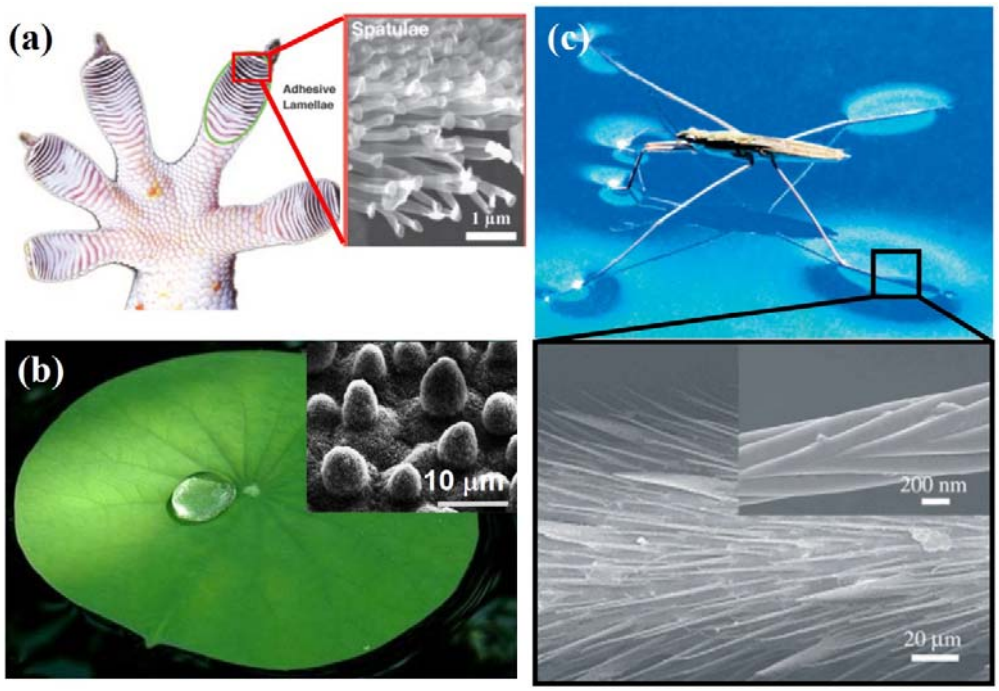

Figure 1.1 Nano-world in biology. (a) Highly adhesive properties of Gecko's feet.[2] (b) Self-cleaning effects of lotus leaves.[6] (c) Non-wetting property of water striders.[5] In each case, the inset shows scanning electron microscopy (SEM) images of micro- and nano-scale structures.

two of the well-known biology are shown, which is have the unique optical functions. One of the discoveries is the coloring effect on butterfly wings, which is different from the intrinsic color of pigmentation.[7] The periodic structures on the butterfly wings which is able to reflect a narrow range of wavelength.[8] Efforts for producing artificial photonic crystals are motivated by the structures on the butterfly, enabling developments of optical devices such as optical filters, optical couplers, and lasers.[9, 10] In addition, the well-developed visual system of a fly and moth has the superior capacity of seeing motion, colors, and patterns of objects around them. As shown in Figure 1.2(b), their eyes are covered with hexagonal arrays of bumps smaller than the wavelength of visible light, exhibiting ultimately low reflections.[11, 12] This allows the moth to see well in the dark without reflections, hiding its location against predators. The antireflective structures also give rise to a large variety of technological applications such as solar cells, photodiodes, flat panel displays, and many other optical components.[13]

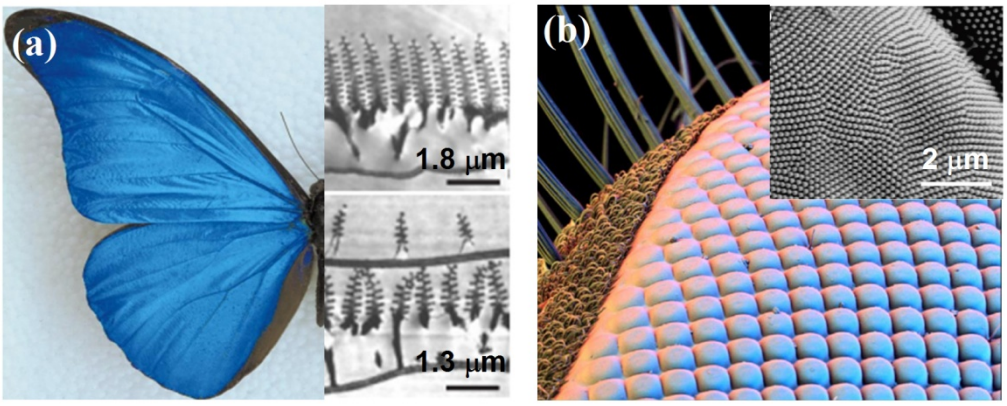

Figure 1.2 Nanoworld in biology. (a) Color through structure on butterfly wings[7] and (b) optical antireflective properties on moth compound eyes.[8] In each case, the inset shows SEM images of corresponding micro- and nanometer-scale structures.

The investigation of the natural nanostructures leads to artificial biomimetic materials with reduced engineering efforts. Namely, researchers can find a shortcut for real applications. One of the widely studied areas is the optical and optoelectronic application, inspired by a moth, fly, and butterfly. For example, the reduced reflection by the structured layers can be used to enhance the energy conversion efficiency in optoelectrical applications. In this thesis, the works focus on the optical interaction of light with sub-micron structures for optoelectrical devices. In addition, the unique anti-wetting (or self-cleaning) properties induced by the surface structures and surface waxing as seen on a lotus leaf is one of the major topics for outdoor applications of the photovoltaic devices. In the following sections, theoretical background of the optical and chemical properties existing in nature will be introduced, followed by experimental achievements and its applications.

1.2 Literature review

In this review, theoretical explanations for the antireflection and the self-cleaning effects will be given. Then, various experimental methods of achieving the antireflection and self-cleaning properties for optoelectronic applications, specifically for photovoltaic applications, will be explored from the conventional thin film antireflection coatings to a more recent idea of sub-micron texturing.

1.2.1 Highly transparent surface – principle, fabrication and application

Over five decades ago, Bernhard & Miller discovered that the outer surface of moth-eyes consists of an array of sub-100 nm nipples.[14] The nipple array considerably reduces the ~4% of reflection at the eye's surface to less than 1%, therefore, transmission increases up to more than 99%. The increased transmission helps to be more light-sensitive for the light-craving moths. A moth with large and glittering eyes is quite conspicuous and is vulnerable for predation. However, the optical action of the nipple array is a severe reduction of the reflectance on the eyes surface, and moths can hide their eyes even in darkness.[7] Further researches demonstrate that nipple arrays of nanostructures are widespread among insects, not only moths and flies.[15] In a comparative survey, Bernhard *et al*. inspected the eye's surface of 361 insect species and they found the antireflective strategy to hide themselves.

The idea behind an antireflective coating can be realized from a single layer dielectric thin film. Fresnel's theory suggests a simple antireflective model with a single layer of thin film.[16] The refractive index is a property of a material, which characterizes it according to the velocity of light in the medium with respect to that in air.[16] The change of the refractive index on a path of light changes the velocity of light and causes optical disturbance making an object visible. The refractive index is a tool to tune optical behaviors on a medium surface along with the thickness of the film on the surface.

As presented in Figure 1.3(a), the single layer leads to a creation of double interfaces (air/film and film/substrate) resulting in two reflected waves. When two or more light waves overlap, according to the principle of superposition, the resultant electric field intensity is equal to the sum of the intensities from each wave. If two waves are out-of-phase with respect to one another, superposition results in the canceling out their electric field intensities. This destructive interference is a main mechanism behind the single layer antireflective thin film coatings. The requirements for the destructive interface are that the thickness of the thin film must be an odd number of quarter wavelength ($\lambda/4$). Even though the film meets those conditions,

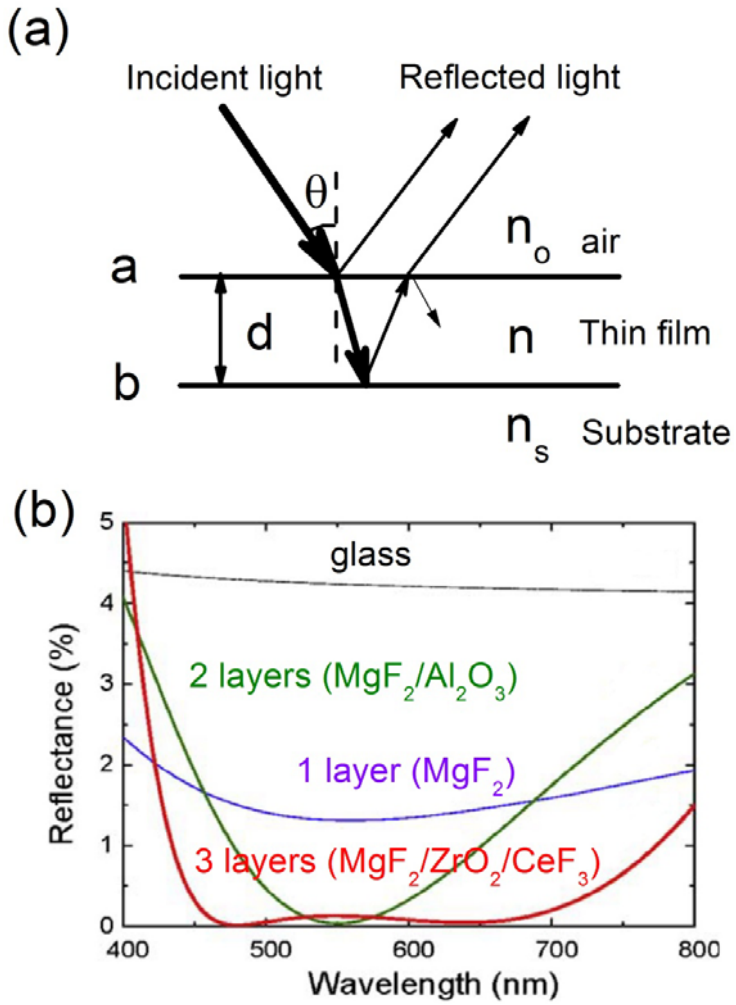

Figure 1.3 (a) Schematic of a single layer thin film antireflective coating. (b) Reflectance of different antireflective coatings. Here, the refractive index of MgF_2, Al_2O_3, ZrO_2, and CeF_3 is 1.38, 1.69, 2.05, and 1.64, respectively.[17]

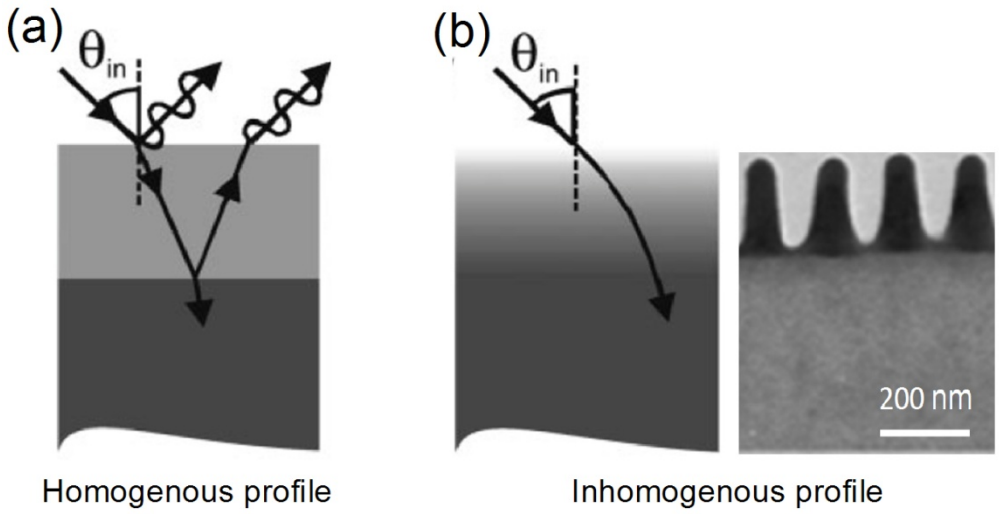

Figure 1.4 Schematics of (a) homogeneous refractive index profile and (b) inhomogeneous refractive index profile and the imaginary light paths in each film.[18]

zero reflection on the single layer film can be achieved only at a target wavelength and incident angle.

Further studies reveal that increasing the number of layers or introducing an inhomogeneous layer can improve the performance of the antireflective coating by achieving relatively wider spectral coverage with close to zero reflection as seen in Figure 1.3(b).[17, 19] Instead of the homogeneous single- or multi- layer film, gradient refractive index antireflective coatings show a desirable characteristic, which can overcome current limitation of the homogeneous antireflective layer such as monochromatic and normal incident angle limits.[13]

In line with that point, moth eyes give an inspiration for the different antireflection mechanism. Arrays of subwavelength features blur the properties at the interface between two media as if the light encounters a homogeneous layer whose 'effective' optical properties are a spatial average of the two media as shown in Figure 1.4.[20] Actually, the advanced antireflection properties of moth eyes are attributed to the shape of the structures.[21] As depicted in Figure 1.4(b), the textured layer with tapered nanostructures can be considered as a single layer of inhomogeneous film with a refractive index profile varying monotonically along its thickness. The gradually varying refractive index can guide more light into the back side, and show broadband and omnidirectional antireflective properties.[22]

Early researches proposed various refractive index profiles to achieve a perfect antireflective coating. Xi *et al*. calculated wavelength-dependent reflectivity for linear, cubic, and quintic index profiles.[23] The calculated index profiles and reflectivity are presented in Figure 1.5. Generally, the quintic index profiles are widely accepted as nearly optimum profiles of gradient refractive index as demonstrated in Figure 1.5(b) and (c). Since a linear profile is easy to achieve on various substrates, many studies have reported that the antireflective coating with a linear index profile suppresses the reflection in a broadband spectrum as well as omnidirectional reflection.[24]

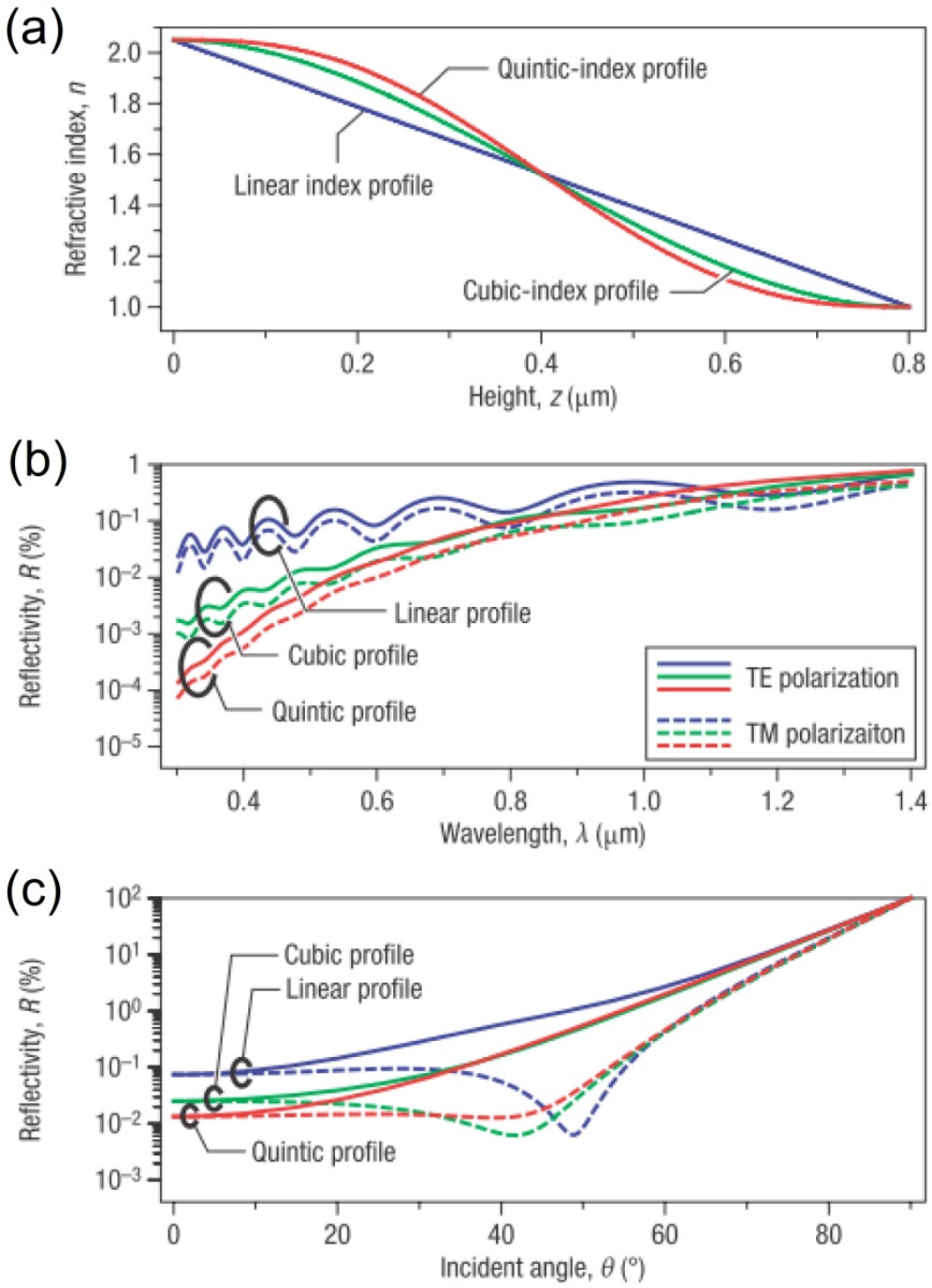

Figure 1.5 Different index profiles for gradient refractive index coatings on a substrate with refractive index 2.05; (a) linear, cubic and quintic index profiles. (b) Calculated reflectivity for each index profiles as a function of wavelength. (c) Calculated reflectivity as a function of incident angles at the wavelength of 628 nm.[23]

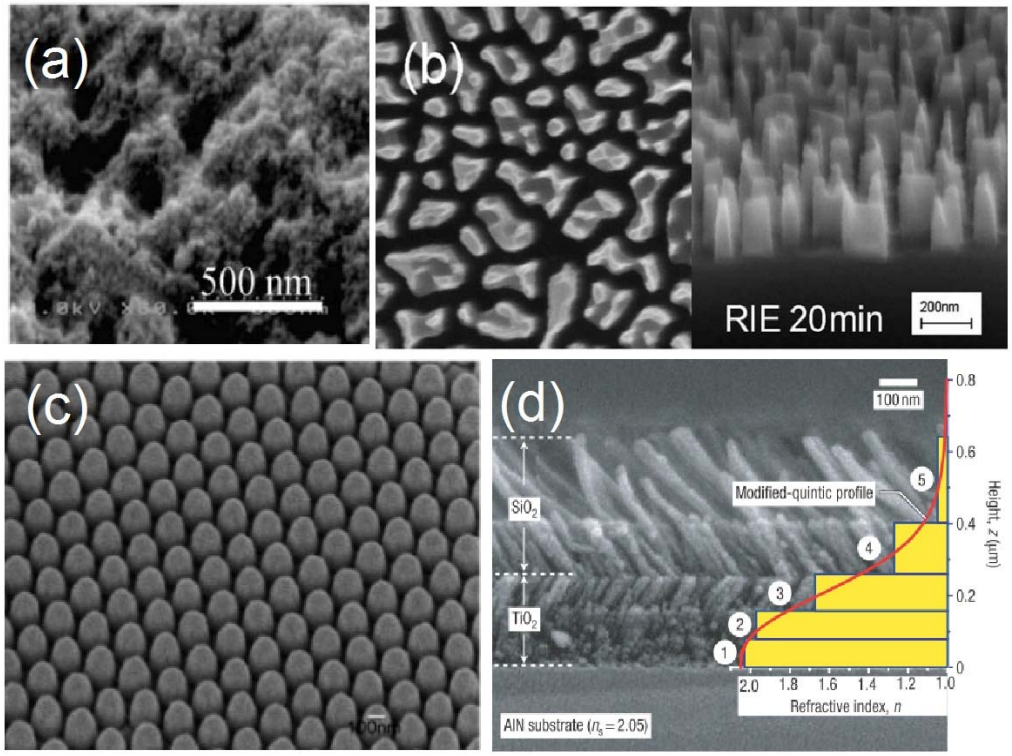

Figure 1.6 SEM images of nanopatterned surface with different methods; (a) Chemical etching with Ag catalyst.[25] (b) Reactive ion etching(RIE) etching using metal nano-islands as an etching mask.[26] (c) 2D colloidal crystals as an etching mask[27] and (d) oblique angle deposition for multilayer antireflective layer.[23]

Various techniques have been reported for implementation of the antireflective coatings in nanoscale. Generally, the fabrication routes can be classified into bottom-up and top-down approaches. Top-down technologies, such as electron beam lithography, interference lithography, and nanoimprint lithography are commonly used to generate subwavelength structures.[28, 29] However, top-down methods require sophisticated equipments and suffer from limited size of sample and expensive processing cost. On the other hand, bottom-up process provides a much simpler and cheaper alternative in creating nanostructures overcoming the disadvantages of top-down techniques.

In the Figure 1.6(a)-(c), various results from bottom-up processes are shown, such as chemical etching,[25, 30] thermal annealing of thin metal films,[26, 31] and sol-gel process.[27] Since tapered shape can take advantage of its gradient index profile for effective antireflection, it has been mostly tried to texture the various tapered structures including pyramids,[32] porous structures,[33, 34] nanorods,[35] nanocones[36, 37] and nanotips[38] as

shown in Figure 1.7. The structures with a taller height and higher packing density are desirable since the structural features are more desirable to enhance the antireflection properties in the broadband range.[38, 39] Omnidirectional antireflective characteristics on disordered nanostructures and ordered nanostructures are also reported.[39]

However, the practical application of the bottom-up technologies is still restricted due to the low through-put and incompatibility with standard fabrication processes. Recently, oblique angle deposition has been developed and utilized to fabricate antireflective surfaces.[23, 40] As a compatible process with standard fabrication technologies, the modified deposition method shows that extremely low reflection can be achieved over a broadband range of wavelengths with the graded index multi-layers stacks using the TiO_2 and SiO_2 nanorod layers as seen in Figure 1.6(d), leading to a minimum refractive index of 1.05.[23]

The antireflective performance of various textured surface is shown in Figure 1.7. For photovoltaic applications, the broadband antireflection may enable efficient light collection leading to efficient harvesting of solar energy.[35] The classical design for efficient light trapping in crystalline solar cells is the pyramid structure which allows a significant reduction in the thickness of active solar cell materials, as it increases the chance of light absorption in a thin solar cell.[41, 42] The feature sizes of these pyramid arrays are typically around tens of microns. The theoretical limit of a single crystalline silicon solar cell is 30%, and the highest power conversion efficiency is almost reaching 25% using the light trapping schemes.[43, 44] However, this approach should be distinguished from the antireflective property. The micro-scale pyramidal features work as increasing light path in silicon substrates, not suppressing the reflection at the surface. Recently, a few studies reported that antireflection layers on a solar cell can enhance conversion efficiencies.[45, 46]

A conventional method for reducing the reflection is to add silicon oxide or silicon nitride on top of solar cells. In order to overcome the limitation of the thin film based antireflective coatings such as monochromatic transparency and limited incident angle of incoming light, surface texturing on

the nanoscale has been studied to find appropriate graded index profiles as shown in the previous section.

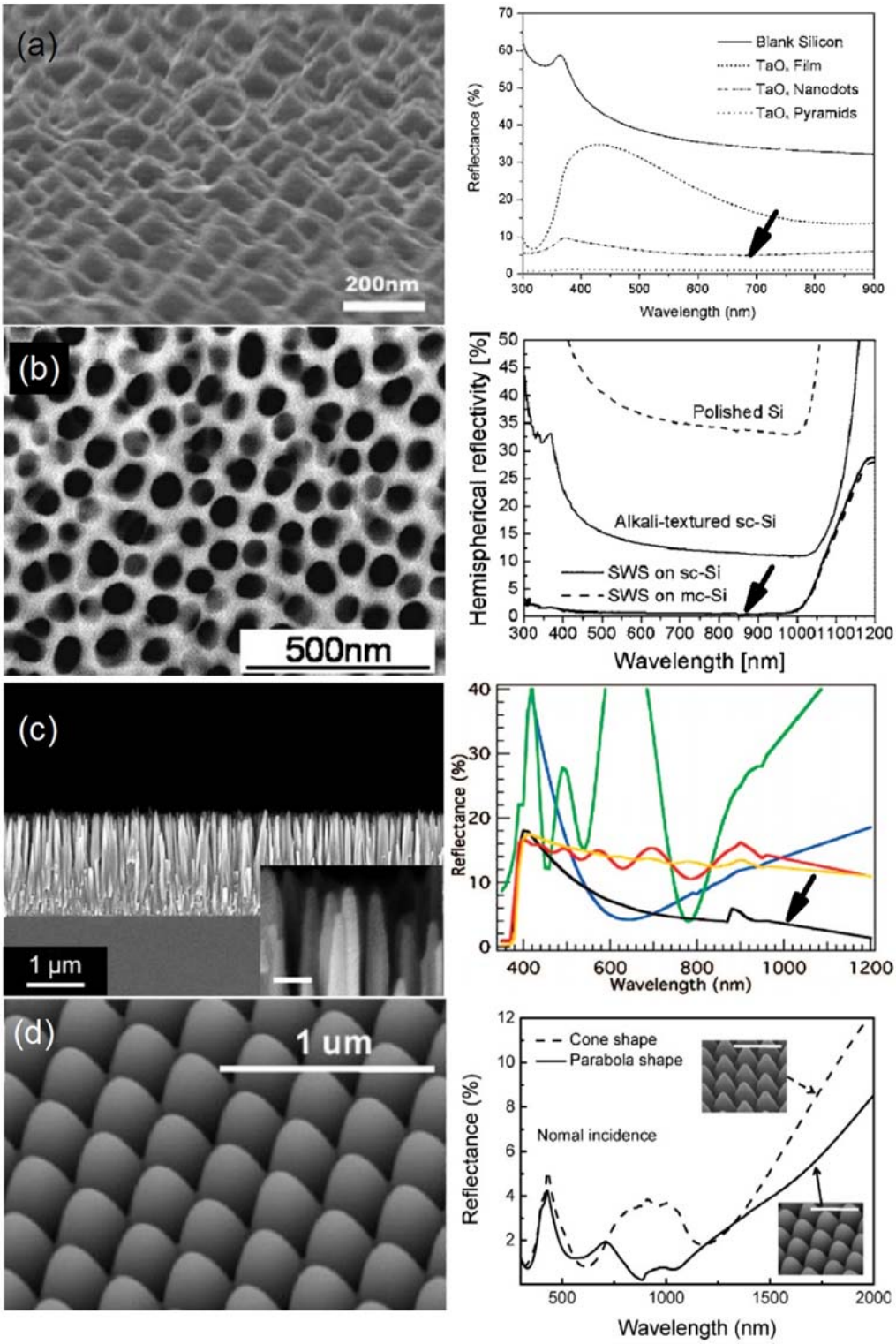

Figure 1.7 SEM images and corresponding reflectance spectra of (a) pyramids,[32] (b) nanopores,[33] (c) nanotips,[35] and (d) nanocone textured surface.[37] Arrows in the figures indicate the reflection spectra after surface texturing.

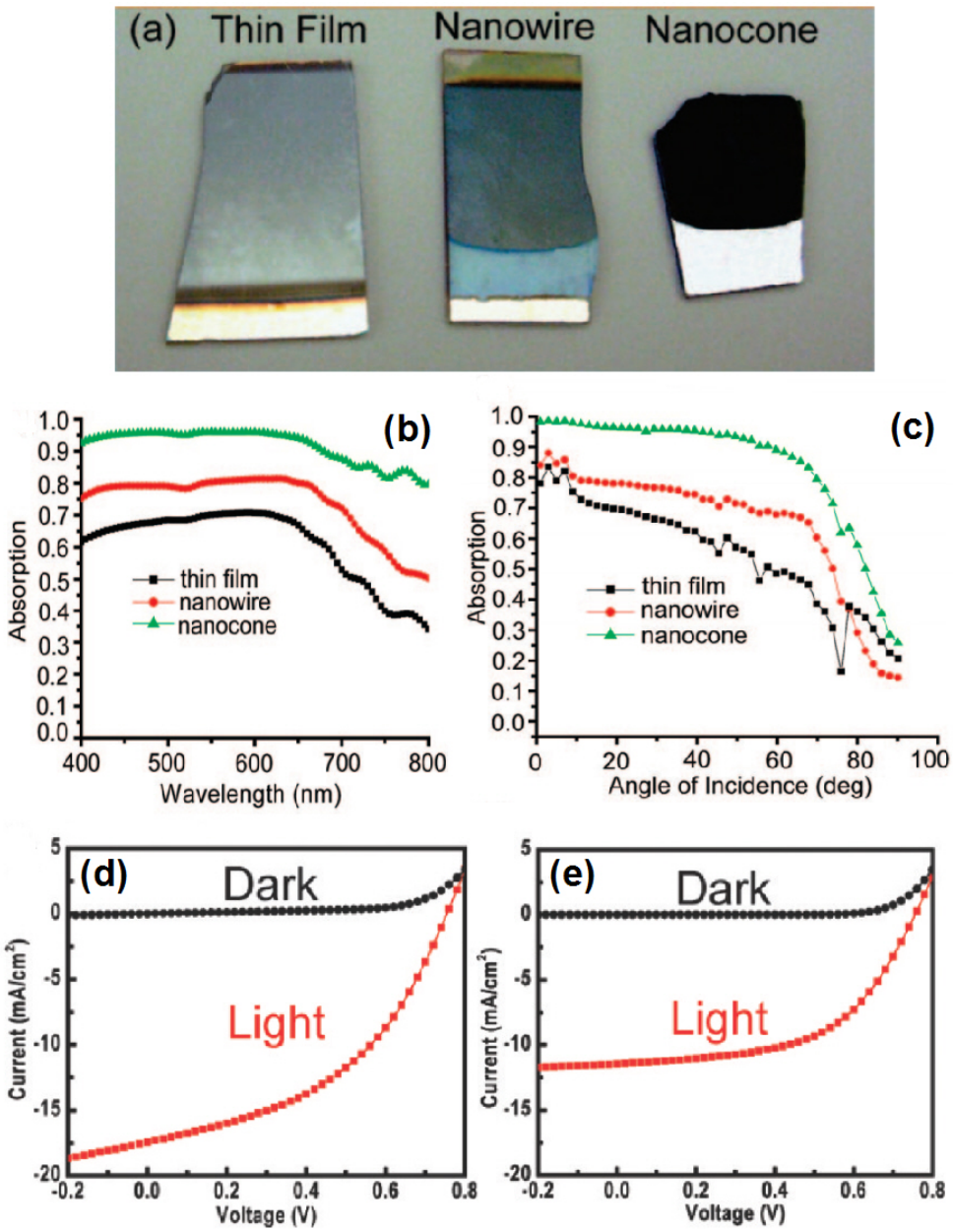

Figure 1.8 (a) Photographs of amorphous silicon with three different nanostructures. (b) Optical absorption measurement as a function of wavelength and (c) incident angle. Power conversion of a-Si:H solar cells with (d) nanodome and (e) flat substrate.[36, 45]

Figure 1.8(a) shows the amorphous silicon samples with an antireflective surface. As the textured layer has a more gradient index profile with the nanocones, it is clear that reflection is dramatically suppressed. The broadband antireflection as well as omnidirectional absorption is also demonstrated in Figure 1.8(b) and (c), respectively. Although the most of the antireflection studies have focused on the optical properties of nanostructured layer, the effects of antireflection on the photovoltaic performances are shown

in Figure 1.8(d) and 1.8(e). The antireflection coating allows more photon to reach to the active region of silicon, and more electrons and holes can be extracted, resulting in the increased short circuit currents. Furthermore, the cost effectiveness and scalability for large area texturing should be considered for the photovoltaic applications.

1.2.2 Self-cleaning surface – principle, fabrication and application

The study on wetting behaviors of solid surfaces by liquid is a very important in surface chemistry due to the variety of possible practical applications.[47, 48] On a typical solid surface, a drop of water slides across and leaves most of dirt particles sticking to the surface as shown in Figure 1.9(a). However, mysterious surface wettability of lotus leaves, water-strider, and animal furs inspires researchers for the surface energy engineering.[3, 5]

Lotus leaves are one of the most well-known examples among the natural water repellent surfaces. When a liquid droplet drops on a lotus leaf, it remains as a droplet rolling on the surface. The surface wetting properties are normally characterized using contact angle measurements. When the contact angle of water is larger than 150°, it is called superhydrophobic. On the other hand, the water droplet can spread out on the surface showing a water contact angle of almost 0°, which is called superhydrophilic. Barthlott and Neihuis investigated the surface of lotus leaves and discovered that the structures of a lotus leaf consist of a combination of two scale roughness: one around 10 μm (rough structure) and the other around 100 nm (fine structure).[4] In addition, the hydrophobic surface arises from the epicuticular wax crystalloids. The wax has a contact angle of 110°, which is not highly hydrophobic. However, the lotus leaf shows superhydrophobicity with the aid of the enhanced roughness.[4] As shown in Figure 1.9(b), the rolling of water droplets and sweeping the contaminants on the lotus leaf result in a very low degree of contamination, which is referred as the lotus effect or self-cleaning effect. The non-wetting surface can prevent moisture and dirt accumulation, and make the surface slippery and abrasion-resistance.[49]

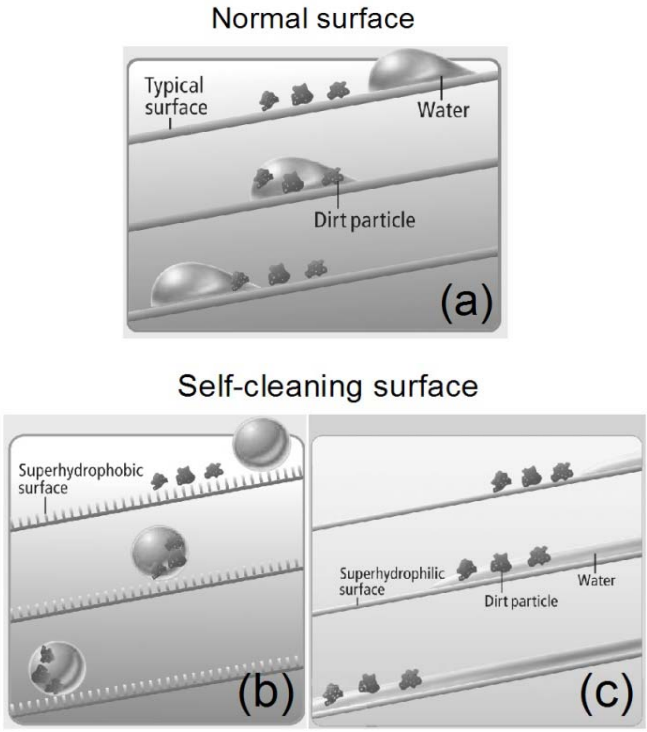

Figure 1.9 Slip of water droplet from an inclined surface with (a) hydrophobic (b) superhydrophobic and (c) superhydrophilic surface. On the normal surface, the water drop crawls over the dirt particles, while the dirt particles are collected and taken away on the self-cleaning surface.[50]

The second class of self-cleaning surfaces to be discussed differs from the lotus effect. Figure 1.9(c) shows the superhydrophilic self-cleaning mechanism. The superhydrophilic surfaces are wetted easily with very low or vanishing contact angles, on which water contact angle is less than 5°.[48] Spreading of water on the superhydrophilic surface forms a layer of water across the surface, easily carrying away dust and dirt as it flows. If the surface is inclined, the spreading liquid carries contaminant along the surface.[47] In particular, most of hydrophilic coatings are based on the photocatalytic effects of TiO_2.[51] It is revealed that photocatalysis causes the coating to chemically break down organic dirt on the surface, while hydrophilicity only causes water to form sheets. Moreover, contact angles are reduced to very low values under sunlight and dirt is washed away. On the other hands, the antifogging surface based on the superhydrophilicity is also reported on patterned glass surfaces, showing the super-high surface energy can be achieved by the patterning itself on hydrophilic surfaces.[52]

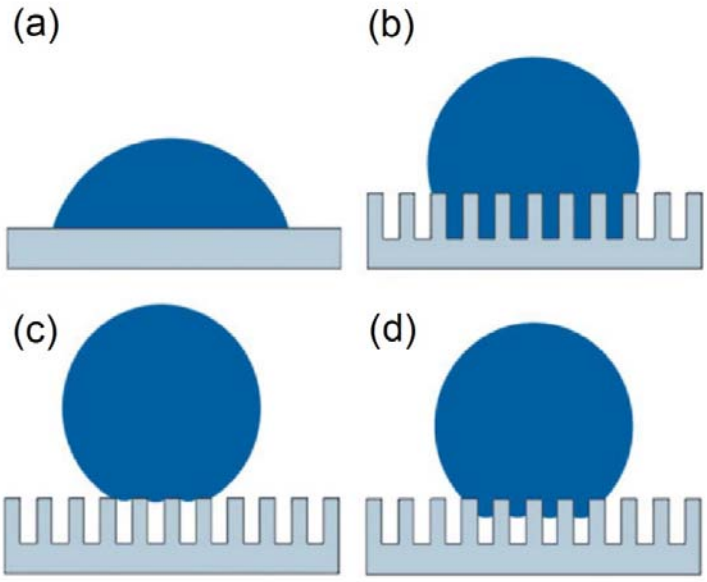

Figure 1.10 Effect of surface structure on wetting behaviors. A liquid drop on (a) a flat substrate (Young's states) and (b)-(d) structured surface. Liquid drop makes contact with a substrate by (c) Wenzel's states (c) Cassie's states and (d) Intermediate state between Wenzel and Cassie states.[3]

Figure 1.10 shows the effect of surface structures on the wetting behavior. On a flat surface, the wettability, which is quantified by contact angle of a water droplet, is given by Young's equation. The Young's angle (θ) is a result of thermodynamic equilibrium of the free energy where a liquid/vapor interface meets a solid surface, which is given by

$$\cos\theta = \frac{\gamma_{SV} - \gamma_{SL}}{\gamma_{LV}}, \qquad \text{(Eq. 1.1)}$$

where γ_{SV}, γ_{SL} and γ_{LV} refer to the interfacial surface tensions with S, L and V as solid, liquid and gas, respectively. Each interface minimizes the surface area between two different phases, so that a water droplet minimizes the contact with the surface and forms a balanced contact angle. [53-55]

However, as seen in Figure 1.10(b) and (c), roughness also affects the wettability, which is different from the one expected from Young's equation. The Wenzel and Cassie equations are commonly used to explain the role of the surface roughness on the apparent surface wettability.[53-55] In the Wenzel case (Figure 1.10(b)), the liquid completely contact with the roughened surface. Meanwhile, in the Cassie theory (Figure 1.10(c)), vapor pockets are assumed to be trapped underneath the liquid, which gives heterogeneous contact between the droplet and the surface. In either case,

much higher contact angles are observed than that of flat surface if the intrinsic surface energy of the substrate is high.

In Wenzel's states, there is a linear relationship between the contact angle and the surface roughness:

$$\cos\theta_w = r\cos\theta \qquad \text{(Eq. 1.2)}$$

where θ_w is the apparent contact angle, r is the roughness factor and θ refers to Young's angle. The roughness is defined by the ratio of actual surface area and apparent surface area, so the rough surface has $r > 1$. Therefore, the Wenzel's relation predicts that more hydrophobic surface($\theta_w > \theta > 90°$) for a hydrophobic surface, and more hydrophilic surface ($\theta_w < \theta < 90°$) for a hydrophilic surface. In the Wenzel's regime, the roughness enhances both hydrophobicity and hydrophilicity.

As the roughness factor r increases more, increased air fraction leads to the suspension of water droplet. Cassie and Bexter define new models for the case:

$$\cos\theta_C = f_s\cos\theta_s + f_v\cos\theta_v \qquad \text{(Eq. 1.3)}$$

where f_s and f_v are the are fractions of the solid and vapor on the surface, respectively. Since air fraction(f_v,) is 1- f_s and $\theta_v = 180°$, the resulting contact angle can be calculated as

$$\cos\theta_C = -1 + f_s(\cos\theta + 1) \qquad \text{(Eq. 1.4)}$$

From the equation, contact angle is a function of solid fraction for a given surface with contact angle θ. Therefore, the smaller solid fraction and a higher intrinsic contact angle are necessary in order to get a superhydrophobic surface. Unlike the Wenzel's case, this model may predict a surface cannot exist in the Cassie state for $\theta < 90°$.

The Wenzel and Cassie model predict the coexistence of two different apparent contact angles. However, the transition between two states was also reported when the physical force was applied (Figure 1.10(d)). The threshold value of the equilibrium contact angle for the transition is obtained by equating the Wenzel equation and the Cassie equation.

$$\cos\theta_T = (f_s - 1)(r - f_s) \qquad \text{(Eq. 1.5)}$$

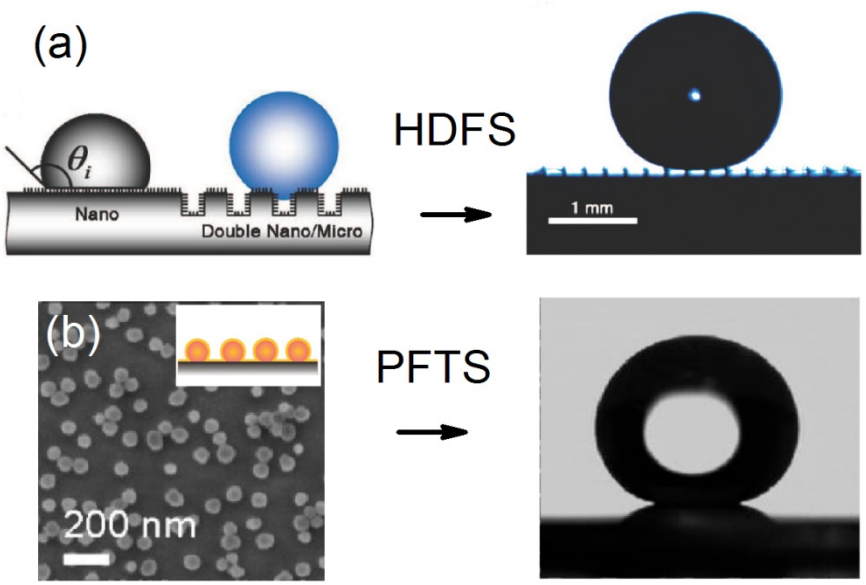

Figure 1.11 Schematics and measured water contact angle of (a) double structured surface after heptadecafluoro-1,1,2,2-tetrahydrodecyl-trichlorosilane (HDFS) coating[56] and (b) single structured surface after perfluorodecyl trichlorosilane (PFTS) coating.[57]

If the Young's contact angle is lower than the threshold value given by Equation 1.5, the Wenzel mode will be obtained. If the apparent contact angle of a liquid droplet is in the Cassie mode, the substrate must have a high Young's contact angle or θ_T must be smaller than the Young's contact angle.

The self-cleaning mechanism of hydrophobic surfaces relies on structural feature and surface chemistry.[48] Understanding the complementary roles of the two key surface parameters, surface energy and roughness, has led to the development of a number of artificial superhydrophobic surfaces. There are many ways to fabricate rough surfaces and functionalized surfaces, such as wax solidification, lithography, vapor deposition, and sol-gel methods.[58-60] Here, we will highlight the methods for surface energy modification on rough surfaces and the characterization of the self-cleaning effect in outdoor.

In general, two main approaches have been developed to generate superhydrophobic surfaces.[59] One is to increase the surface roughness of low surface-energy materials. The other is to fabricate micro/nanostructures on a certain substrate and then to modify the as-prepared surface with low surface-energy materials. In both cases, engineering surface structures plays a key role to superhydrophobicity. For example, as depicted in Figure 1.11 the

hierarchical structure (microscale array of nanopillar covered with nanoscale structures) demonstrates the superior superhydrophobicity than single nanostructured surfaces, showing the significant increase of the water contact angle from 156° to 173.3°.[56] Another study reported that a surface covered only by nanopillar arrays obtains superhydrophobicity with a water contact angle of 172° after chemical treatments.[57] Note that the surface energy modification by chemical treatment is no longer limited to low surface-energy materials, but it can extend the formation of superhydrophobic surfaces to many other systems.

Self-assembled monolayers (SAMs), which is molecular assemblies that are formed by immersion of an appropriate substrate into a solution or by gas-phase evaporation, is introduced as a coating method to make the surface energy low. The various SAM coatings to realize superhydrophobicity on a rough surface are summarized in Table 1. Taking advantage of the hydrophobicity of alkyl chain and perfluorinated silanes, an organic silane was used to modify surfaces bearing hydroxyl groups, such as silicon wafers, glass slides, and silicon nanoparticles, to create low surface-energy coatings.[59] For example, the surface wetting behavior changes from superhydrophilicity (~3°) to superhydrophobicity (~154°) after surface modification with octyltrimethoxysilane (OTS).[61] The development of the coating technique overcomes the limitation to get a super-low surface energy even on the hydrophilic surface.

Table 1.1 Methods for producing superhydrophobic surfaces.

Roughness formation	**Low-surface-energy chemicals**	**Contact angle (°)**
Nanoparticle	perfluorodecyl trichlorosilane (PFTS)[57, 62]	170
	poly(dimethylsiloxane) (PDMS)[63]	165
Sol-gel process	trimethylethoxysilane (TMES)[64]	151
	hexadecyltrimethoxysilane (HDTMS)[65]	153
	perfluorodecyl trichlorosilane (PFTS)[66]	151
Hydrothermal growth	decyltrimethoxysilane (DTMS)[67]	161
Etching	perfluorodecyl trichlorosilane (PFTS)[56]	173

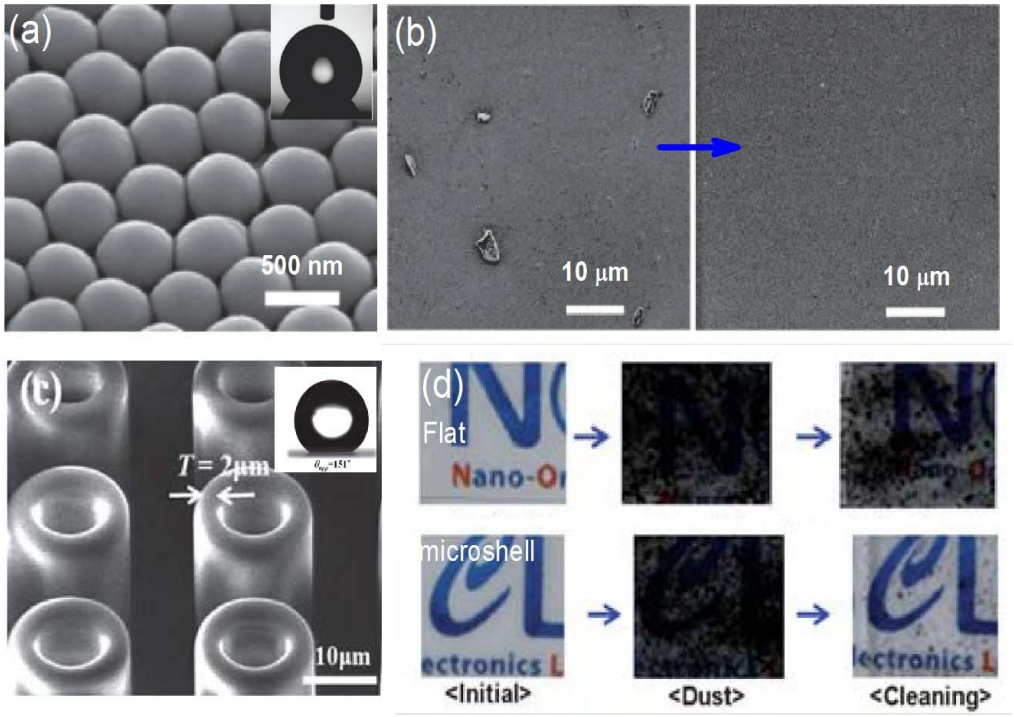

Figure 1.12 Surface morphology and water contact angle of (a) nanodome and (c) microshell structured surface. (b, d) shows the self-cleaning effect induced by superhydrophobicity by comparing before and after water wash.[45, 68]

The integration of the surface cleaning effect with the photovoltaic device is desirable, since solar cells are operated in outdoor environments and accumulation of dust on the solar panel blocks the sunlight, reducing the energy conversion efficiency. Zhu *et al*. shows that nanodome solar cells possess the self-cleaning capability via superhydrophobicity due to the nanodome morphology.[45] The nanodome surface is modified with hydrophobic SAM, perfluorooctyl tricholorosilane (PFOS) and the water contact angle shows almost superhydrophobicity with 141° as shown in the inset of Figure 1.12(a). The accumulated dust is cleaned up by simply rolling a water droplet across the surface and the SEM image in Figure 1.12(b) exhibits a huge difference after cleaning. The self-cleaning effect by superhydrophobic surface was also shown by Park *et al*.[68] A perfectly ordered microshell array in Figure 1.12(c) is fabricated on a transparent and flexible PDMS elastomer surface. The superhydrophobic microshell PDMS shows a superior dust cleaning effect compared to that of flat PDMS as shown in Figure 1.12(d). The anti-wetted surface is expected to prevent degradation of the solar cell efficiency by dust accumulation. Even though the self-cleaning effect has been

shown in laboratories, further studies are needed to verify the feasibility of superhydrophobic surfaces in the real applications of optoelectronic devices, since the transparency and durability of the coatings should be taken in account for outdoor uses.

1.2.3 Scaling of the smart surface

Next generation coatings must aim to combine the self-cleaning properties with additional functionalities such as antireflection, which can be named "smart coating". Moreover, scaling-up the multifunctional coatings is preferable in terms of market potential. For this purpose the coating should be inexpensive and sufficiently durable for industrial applications. To meet these criteria, numerous approaches have been attempted. Until now, procedures of surface texturing followed by hydrophobization or transforming low surface-energy materials into rough surfaces have been commonly used to produce superhydrophobic surfaces. Moreover, few methods have been suggested for industrial-scale mass-fabrication of multifunctional nanotextured coatings, including nanoimprint, laser interference lithography, spin coating of colloidal crystal and sol–gel processing.[69]

Figure 1.13 shows the photographs of the large area nanotextured surface on various materials. Recently, a large-scale nanopillar array was developed using wafer scale production of non-closed packed colloidal crystals on 4-inch silicon substrates.[13] After modified with fluorosilane, the surface can obtain superhydrophobicity with a water contact angle of 160°, which is required for the self-cleaning effect. The Langmuir–Blodgett method is known as one of the techniques to coat a monolayer of nanoparticles over a large area.[70] As shown in Figure 1.13(b), Langmuir–Blodgett assembled nanoparticles was used as a mask for RIE to fabricate nanopillars with uniform coverage over an entire 4-inch wafer. Another large area nanotexturing method using nanosphere lithography is shown in Figure 1.13(c). Silica cone arrays were fabricated for antireflective and antifogging surfaces on a transparent glass substrate. The rough silica surface exhibits the antireflection as well as superhydrophilic property which can prevent the water condensation on the surface.[52] Nanoimprint lithography is also well developed techniques

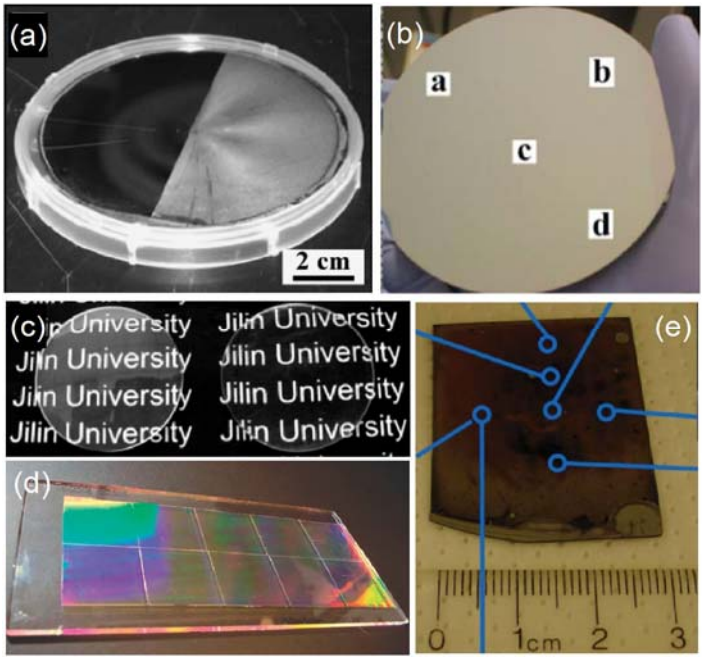

Figure 1.13 Photographs of nanotextured surface fabricated by (a) colloidal crystal (spin coating),[13] (b) Langmuir-Blodgett method,[71] (c) colloidal crystal (interface method),[52] (d, e) nanoimprint (roll - to - roll),[72] and nanoimprint followed by deep RIE etching.[73]

for large area nanotexturing. Figure 1.13(d) shows a PDMS film on a glass substrate patterned by a 4-inch wide and 10.5-inch long 700 nm period grating using the continuous roll-to-roll techniques.[72] Antireflective moth-eye effect on silicon was also demonstrated by the wafer-scale nanoimprint technique and antireflection at large incident angles was achieved with an average reflection below 8% at 60°.[29]

However, the availability of the large scale smart surface in real environments is not fully confirmed due to the potential risk of degradation of the unique functions, especially under UV exposure. Thus, the outdoor test is very important to know the long term durability of the multifunctional coatings in real environments. As shown in Figure 1.14, a few outdoor exposure tests have been reported. In Figure 1.14(a), TiO_2 thin films coated by (fluoroalkyl)silane (FAS) initially have a contact angle more than 150°.[74] The surface can maintain a higher contact angle after 1800 hrs outdoor exposure, when the sample is fabricated in the low TiO_2 concentration condition, where photocatalysis prevents the accumulation of stain. In Figure 1.14(b), more longer monitoring has revealed that the stability and durability of the superhydrophobic surface.[75] The superhydrophobic surface coating

comprising of silicone nanofilaments is slightly affected by the outdoor exposure during 1 year observation. Both rain and snow do not adhere to the surface. The durability of the surface coating can be improved after annealing. Until now, few studies show the durability and stability of the smart surfaces for real applications, even though many research works successfully exhibit the excellent surface properties in the laboratory level experiments.

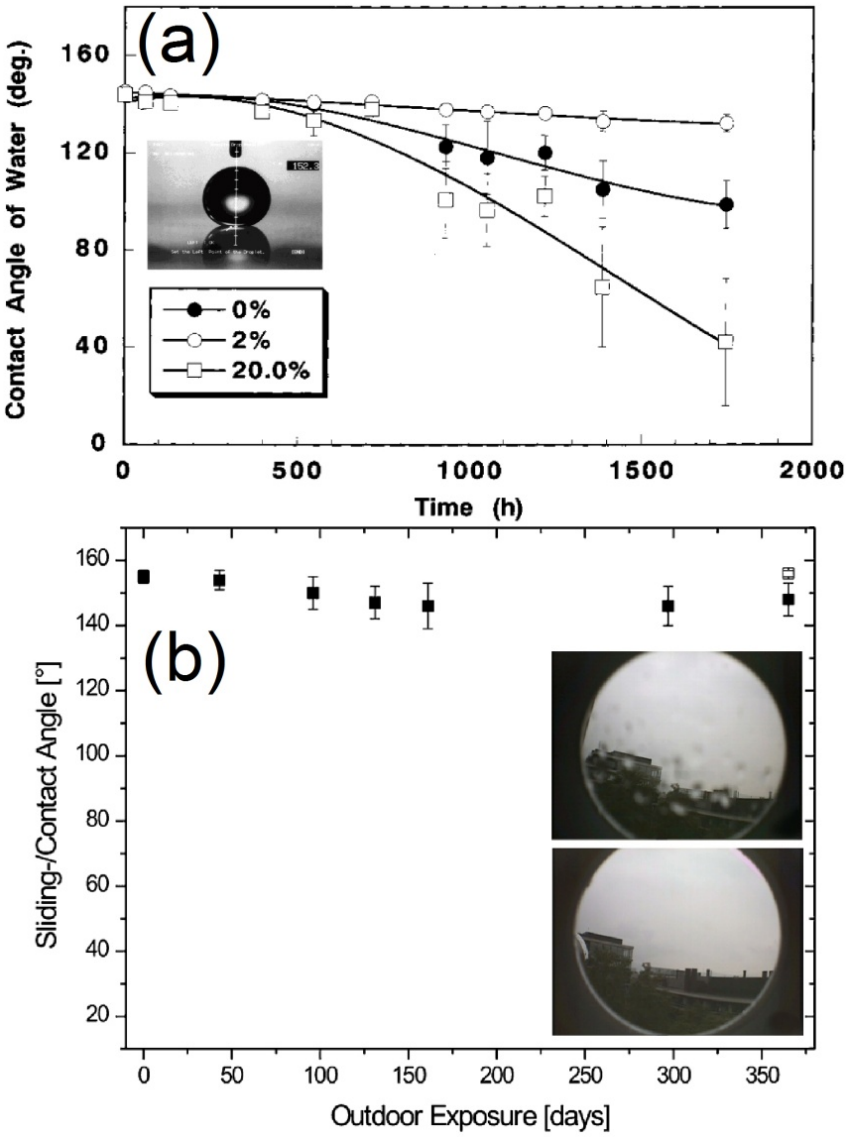

Figure 1.14 Long-term characterization of surface coating. (a) Change of water contact angle for the films under UV illumination. (Inset) Water droplet on the transparent superhydrophobic film with 20 wt% TiO_2[74] (b) Change of water contact angle as a function of outdoor exposure time. (Inset) Webcam images taken through an uncoated (top) and coated (bottom) glass slide during rainfall after 12 months of outdoor exposure.[75]

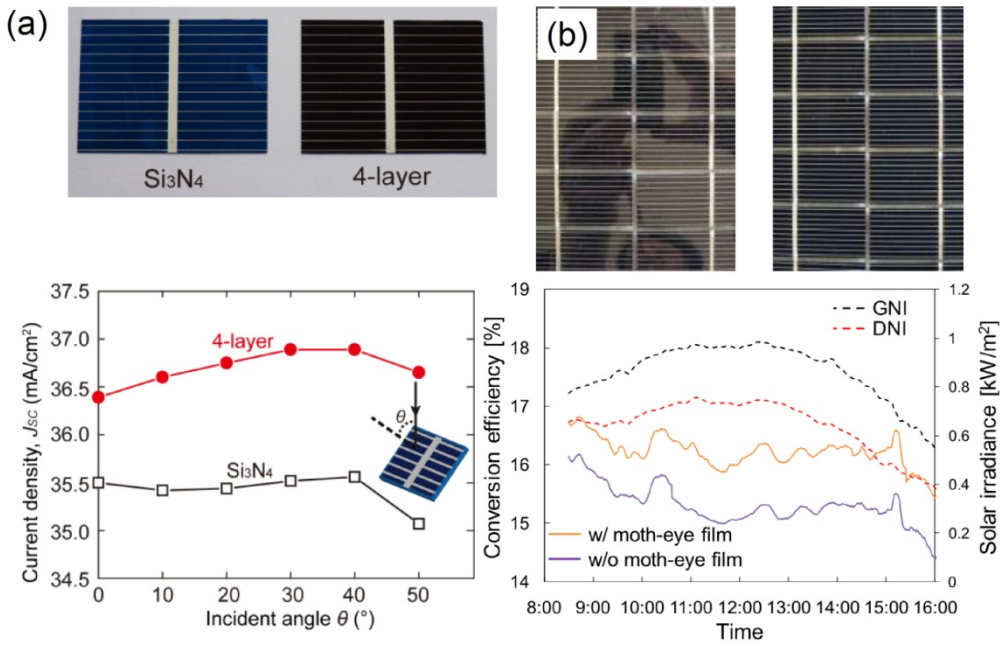

Figure 1.15 Antireflective coating tested on solar cells or modules. (a) Photograph of polycrystalline Si solar cell with the Si_3N_4 and the 4-layer antireflective coatings and measured short circuit current density of the samples.[40] (b) Photograph of the tested crystalline Si modules with the normal glass and the antireflective glass and daily variations in conversion efficiency of the modules.[76]

As a promising applicable area of the smart coatings, a few studies show the large area multifunctional coating on photovoltaic devices as seen in Figure 1.15. Using co-sputtered $(SiO_2)(TiO_2)$ thin film layers, the antireflective layer with an optimized graded index profile is achieved.[40] As shown in Figure 1.15(a) the 6 × 6 $inch^2$ solar cell is coated by low refractive index multilayers. The optimized multilayer antireflective coating shows a reduced total reflection, leading to the high conversion efficiency over a wide range of wavelengths and incident angles. In Figure 1.15(b), solar module is covered by the antireflective glasses. Moth eye structures were fabricated by using nanoimprint on acrylic resin. The overall efficiency increases with an aid of the antireflective coating. Interestingly, the efficiency is improved due to the omnidirectional behavior of the antireflective coating.[76]

As shown in Figures 1.14 and 1.15 the self-cleaning effect of individual superhydrophobic coating has been characterized in outdoor environments for a long duration and the antireflective properties are confirmed with photovoltaic devices. However, the effects of the self-cleaning and antireflection coating on solar cells are not fully proved under long-term

outdoor conditions. Moreover, the durability and robustness of the superhydrophobicity and antireflective property need to be seriously studied.

1.3 Motivation and objective

Inspired by the living organisms in Nature, optically and chemically unique surfaces have been studied and fabricated.[77] As reviewed above, chemical treatment with elevated roughness can offer the potential to develop a smart surface for photovoltaic devices. However, many questions still remain regarding the realization of the smart surface for photovoltaic applications. As shown in Figure 1.16, we suggest five requirements to design the smart surface for industrial purpose. Until now, the basic properties of the self-cleaning and antireflective properties have been studied widely and realized in laboratory scale using numerous methods as reviewed, but only a few studies show how the superhydrophobic surface, which is known to have the self-cleaning effect, works to remove dust and dirt in practice. Studies on the durability of surface coating is even less.

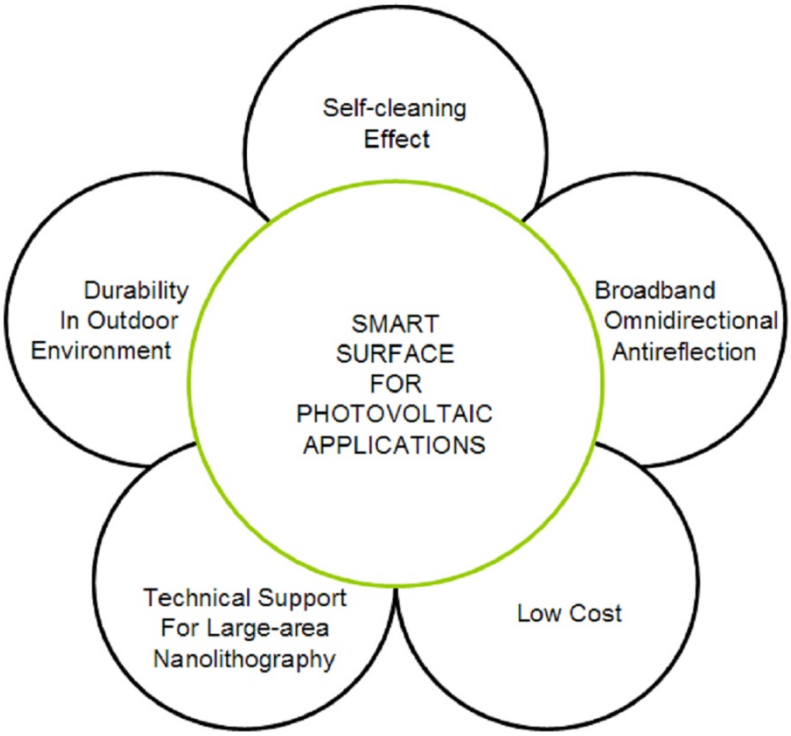

Figure 1.16 Requirement to achieve the smart coating for industrial applications.

Although the durability and sustainability of the smart surface is very important aspect for real applications, little attention has been paid. In addition, there are still many challenges to be settled to realize the large area nanotexturing. Only a few mature techniques can be used to fabricate nanostructures on large substrates. Hence, we have aimed to realize large area smart coatings and its characterization in real environments.

The research activities presented in this thesis are limited to transparent glass materials and its application only for photovoltaic devices, even though the research results have wide applicable areas. Along with increasing concerns for the environment and renewable energy, our study has focused on and contributed to the photovoltaic applications. We have provided the results that the smart surface can work with real devices in real outdoor environments. Moreover, the technique for large area fabrication can be considered as a reliable candidate for mass production after fine tuning of the texturing processes. Reducing the fabrication cost furthermore and compatibility with an existing the semiconductor fabrication process are one of the critical aspects for future works.

The subjects to be covered in this thesis are multi-functional surfaces with special transparency and wettability, and its application for photovoltaic devices in real environments. The scaling-up for large area solar cells is also demonstrated at the last section. The major parts of this thesis are organized in five chapters. In chapter 2, the background of simulation works and a fabrication process used in this thesis is introduced as well as an overview on the characterization methods used for this work is presented. In chapter 3, a brief introduction about the principles behind the antireflective coating is given followed by simulation results. We have studied the dimensional effects of nanostructures on optical transmission as well as the effects of shape of nanostructures. The optical behavior on the nanostructures are calculated for a wide range of wavelengths and various incident angles by a finite difference time domain (FDTD) method in order to get an optimized dimension of the nanostructures. In chapter 4, based on the numerical studies, an antireflective surface is experimentally realized on a glass substrate by using an anodizing method and plasma etching. The structural controllability of the nanopatterning was also shown. In addition, the nanoholes of V-shape behave

as a layer with gradual refractive index, which is a preferable feature for the antireflection effect. Transmittance of the patterned glass is compared to the calculated data. In chapter 5, samples with various surface energies were prepared to monitor their antireflective property along with its self-cleaning effect. A chemically treated patterned glass, which is superhydrophobic, is monitored together with a patterned glass which shows superhydrophilicity. Because of the durability or stability issues of the chemical treatment, the superhydrophilic substrate, on which no chemical process is introduced, shows the most promising performance among the monitored samples. In chapter 6, an advanced fabrication method to scale up the texturing area on a large glass is reported. The large area nanopatterned glasses are packaged with real size solar cells and their superior properties are confirmed by long term outdoor experiments. Finally, in chapter 7, the thesis is concluded by summarizing the accomplishments of this work and proposing future directions.

Chapter 2: Simulation and Experimental Methods

2.1 Simulation method

2.1.1 Finite difference time domain method

Since the early work by Yee,[78] finite difference time domain (FDTD) method has been developed as one of the most effective computational methods in electromagnetism. FDTD method is a robust and powerful solution of the Maxwell equations both in time and space.[79] In particular, FDTD technique gives explicit solutions for a complex geometry over frequency domain without complicated computation, because of its ability to define arbitrary shapes and inhomogeneous properties on the grid-space.[80] Another advantage of the FDTD technique is its capability to visualize the real-time pictures of the electromagnetic waves.

Considering a two-dimensional (2D) structure in anisotropic media, as shown in Figure 2.1(a), FDTD method considers all x, y, and z components of each field variable, because of the anisotropy of the media, which can produce more accurate results for electromagnetic interactions in a medium.[80] Another important feature in the FDTD method is boundary conditions. The schematic in Figure 2.1(b) shows two types of boundary conditions. When the structure is periodic, the dimension can be reduced to one period by applying periodic boundary conditions. Another boundary condition is an absorbing boundary to truncate the simulation space without artificial reflections. The perfectly matched layer (PML) can be defined as absorbing boundaries. We limit ourselves to a 2D structure, but this method can be extended to 3D in a straightforward manner due to the advantages of the FDTD method.

2.1.2 MEEP simulation

MEEP is a free FDTD simulation software package developed at MIT to model electromagnetic systems.[81] The MEEP enables to compute the transmission or scattering spectra from some finite structure with a broad-spectrum source via a single computation. The MEEP software

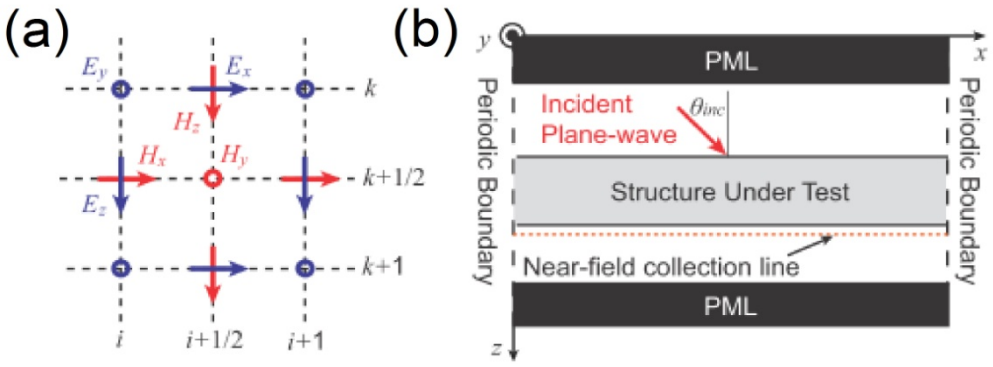

Figure 2.1 Schematic views of (a) a 2D FDTD grid with field variables and (b) a computational space with two types of boundary condition.

takes care of all of flux integration and Fourier transform on the defined grid-space automatically.[81] Since the computed power flux by itself is not very useful, it needs to be normalized, dividing by the incident power at each frequency, in order to get the transmission or reflection spectrum. Practically, this is done by running the simulation twice: one with only the incident wave and no scattering structures, and the other with the scattering structure, where the first calculation is used for normalization.

Figure 2.1(b) illustrates most of the essential factors which should be defined for MEEP simulations in 2D. Using the libctl/Scheme scripting interface, we can define structures, sources, field integrating region, and boundary conditions with more flexibility.

2.1.3 Basic simulations with Fresnel's equations

The Fresnel equations describe the behavior of light when light travels between two media with different refractive index. At the interface, both reflection and refraction of the light occur and the optical behaviors can be predicted by the Fresnel equation. Transmission coefficient and reflection coefficient of the transverse electric (TE) mode and the transverse magnetic (TM) mode are given by

$$t_{TE} = \frac{2n_i \cos\theta_i}{n_i \cos\theta_i + n_t \cos\theta_t} \qquad \text{(Eq. 2.1)}$$

$$t_{TM} = \frac{2n_i \cos\theta_i}{n_t \cos\theta_i + n_i \cos\theta_t} \quad \text{(Eq. 2.2)}$$

$$r_{TE} = \frac{n_i \cos\theta_i - n_t \cos\theta_t}{n_i \cos\theta_i + n_t \cos\theta_t} \quad \text{(Eq. 2.3)}$$

$$r_{TM} = \frac{n_t \cos\theta_i - n_i \cos\theta_t}{n_t \cos\theta_i + n_i \cos\theta_t} \quad \text{(Eq. 2.4)}$$

where θ_i and θ_t is angle of incidence and refraction, respectively, and n_i and n_t is refractive index of incident medium and refracted (transmitted) medium, respectively. From the given equations, we can calculate the reflectance and transmittance at the interface by

$$R = \frac{r_{TE}^{\ 2} + r_{TM}^{\ 2}}{2} \quad \text{(Eq. 2.5)}$$

$$T = \frac{t_{TE}^{\ 2} + t_{TM}^{\ 2}}{2} \quad \text{(Eq. 2.6)}$$

As shown in Figure 2.2, the simulation results by MEEP are compared with the predicted reflectance, calculated from the Eq. (2.5) as a function of angle of incidence. To generate a light source with a tilted angle, we modified the k-vector of light source as shown below. (See Appendix I for the full script used in this simulation study)

```
(define-param kdir (vector3 (sin theta_rad) (cos theta_rad)))
(define k (vector3-scale (* 2 pi fcen) (unit-vector3 kdir)))
(define ((pw-amp k x0) x)
        (exp (* 0+1i (vector3-dot k (vector3+ x x0)))) )
(set! sources
  (list
        (make source
          (src (make gaussian-src (frequency fcen) (fwidth df) ))
            (component source-component)
        (center 0 (* 2 y_spacer) 0)
                (size sx 0 sz)
                (amp-func (pw-amp k (vector3 0 (* 2 y_spacer) )))
)))
```

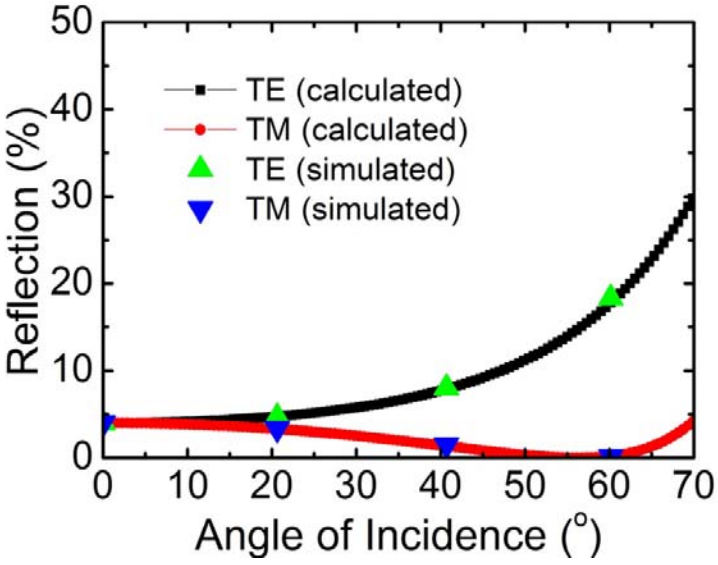

Figure 2.2 Comparison of simulated result with calculated values. The angle dependent reflectance of a glass obtained by using the Fresnel's equation.

The reflectance of light traveling from air to a flat glass substrate with a tilted incident angle is calculated at 0, 20, 40, and 60°. We confirm that simulation results are well matching with the predicted TE and TM polarization from the Fresnel's equations. However, as the angle increases more than 75°, the deviation from the equations increases. This is because we did not allocate enough space to propagate with an oblique angle, due to the required large computing resource.

One of the convenient features of MEEP is the visualization of wave distribution in time domain. In Figure 2.3, simulation studies show the wave propagation from a line source to a structured surface. Taking the advantage of the visualization of the real time images, we can intuitively understand the behaviors of light at the surfaces.

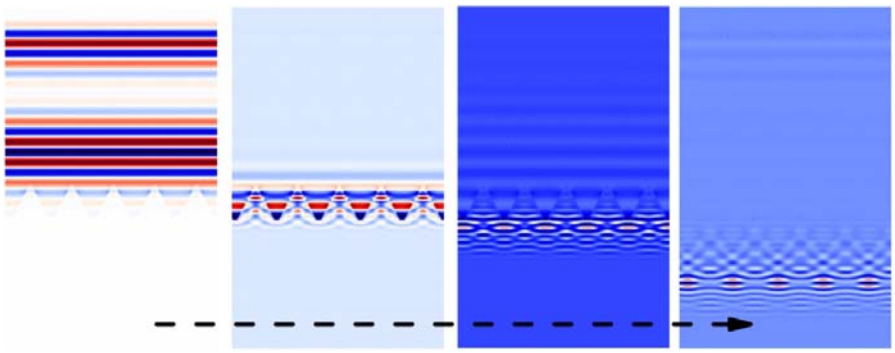

Figure 2.3 Visualization of the real-time pictures of the electromagnetic wave propagating from top (air) to bottom (glass) via structured surface.

2.2 Techniques for nanopatterning

2.2.1 Anodic aluminum oxide formation

As an alternative path to the formation of low-dimensional structures, such as ordered and densely packed arrays of nanostructures, anodic aluminum oxide (AAO) has attracted considerable interest, since the formation of the nanopores in AAO can be controlled precisely, exhibiting highly ordered arrays with an uniform diameter and spacing.[34]

The principal behind the AAO electrochemical process has been well studied. When an aluminum film is covered with a native oxide layer, the increased voltage across the oxide layer without initiating current flow introduces movements of aluminum and oxygen ions through the oxide layer. The ionic transport across the oxide layer under a high field plays an important role in oxide formation during the anodization of aluminum.[82] Once a sufficient high voltage is applied, hydrogen ions are reduced to produce hydrogen gas at the cathode and aluminum is oxidized into Al^{3+} cations at the anode. The current through the oxide is an ionic current driven by the high field.

In Figure 2.4 the overall chemical reaction during the anodization of aluminum is shown, the chemical reaction can be written as[83]

$$2Al + 3H_2O \rightarrow Al_2O_3 + 3H_2$$

At the metal/oxide interface, Al^{3+} ions form and migrate into the oxide layer:

$$Al \rightarrow Al^{3+} + 3e$$

The Al^{3+} ions migrate outwards under the electric field across the oxide from the metal/oxide interface toward the oxide/electrolyte interface.

$$2Al^{3+} + 3H_2O \rightarrow Al_2O_3 + 6H^+$$

At the oxide/electrolyte interface the water-splitting reaction occurs.

$$H_2O \rightarrow 2H^+ + O^{2-}$$

The O^{2-} ions migrate inwards under the electric field across the oxide from the oxide/electrolyte interface toward the metal/oxide interface, to form Al_2O_3

$$2Al + 3O^{2-} \rightarrow Al_2O_3 + 6e^-$$

In the acidic electrolyte where the oxide is soluble, the film dissolution happens:

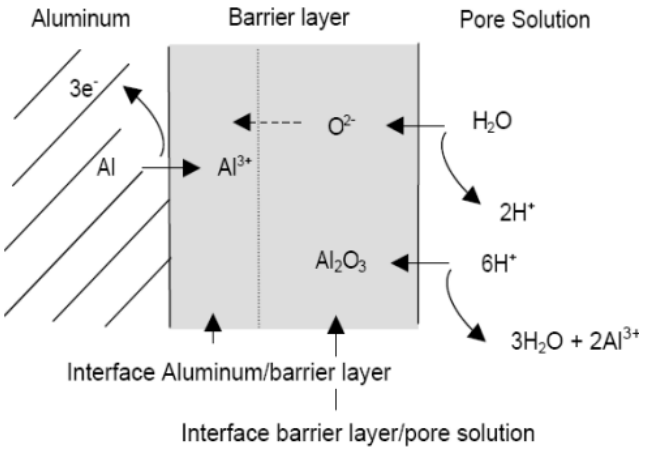

Figure 2.4 Migration of Al^{3+} and O^{2-} ions through the barrier and formation of alumna across the barrier layer.[83]

$$Al_2O_3 + 6H^+ \rightarrow 2Al^{3+} + 3H_2O$$

In addition to the above principle reactions, some anions in the electrolyte may be also incorporated in the aluminum oxide layer.

Those characteristic or properties can be controlled by the anodizing parameter such as anodizing voltage, time and temperature, electrolyte's concentration, and types of electrolyte as well as pre- and post-processes that are implemented before and after the anodizing process. The commonly practiced pre-processes are annealing, degrease, pre-etching, and electropolishing where all the processes are functioned for favoring the formation of AAO film during anodization process. In addition, the ordered AAO can be fabricated by two step anodizing method. At the beginning of the first anodizing process, the pores are randomly distributed. The initial oxide layer is removed but the pre-structured aluminum surface remains. The remained aluminum structures are used as a template for the subsequent second anodizing. During the second anodization the pores arrange in a hexagonal pattern. However, in our experiments, we moved directly to anodization without pretreatment because we prefer disordered array of nanopores. The post-process (post-etching) is for widening the pores. In the acidic electrolyte where the oxide is soluble, the film dissolution happens:

$$Al_2O_3 + 6H^+ \rightarrow 2Al^{3+} + 3H_2O$$

All of anodizing parameters depend on each other to determine the final features of nanoholes, and a suitable combination of those parameters will lead to desirable nanotemplates.

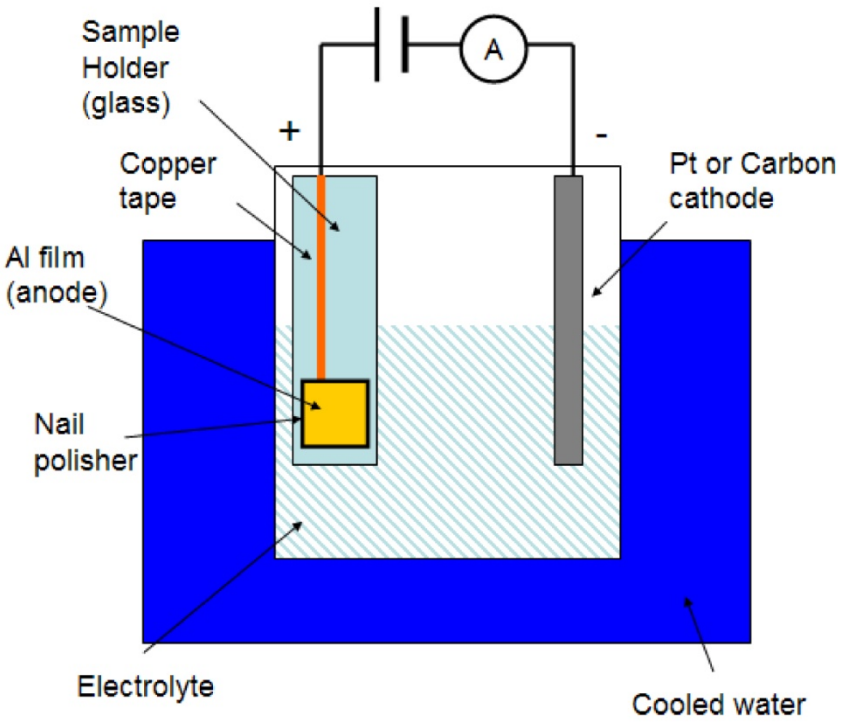

Figure 2.5 Experimental setup for aluminum anodization.

2.2.2 AAO experimental setup

Nanoporous alumina membranes are made from an aluminum film using common anodizing method. A 250 nm thick aluminum film is deposited by electron beam evaporation on glass substrates. In Figure 2.5 the experimental setup for anodization process is shown. Since we observe that the unprotected edges of the thin aluminum film is more easily anodized than the center of the film, we apply nail polisher along the edge of the thin film before proceeding to anodization steps in order to get uniformly anodized surface. A thin copper tape is used for electric connection between the aluminum film and a sourcemeter. The copper tape is also isolated from the electrolyte by nail polisher to prevent the reaction of copper in the electrolyte and ensure stable supply of voltage. The sample size up to 2 cm × 2 cm can be anodized using this technique with good uniformity. All the anodizing processes are conducted at 2 °C in stirred electrolyte. More advanced techniques for large area anodization will be discussed in chapter 6.

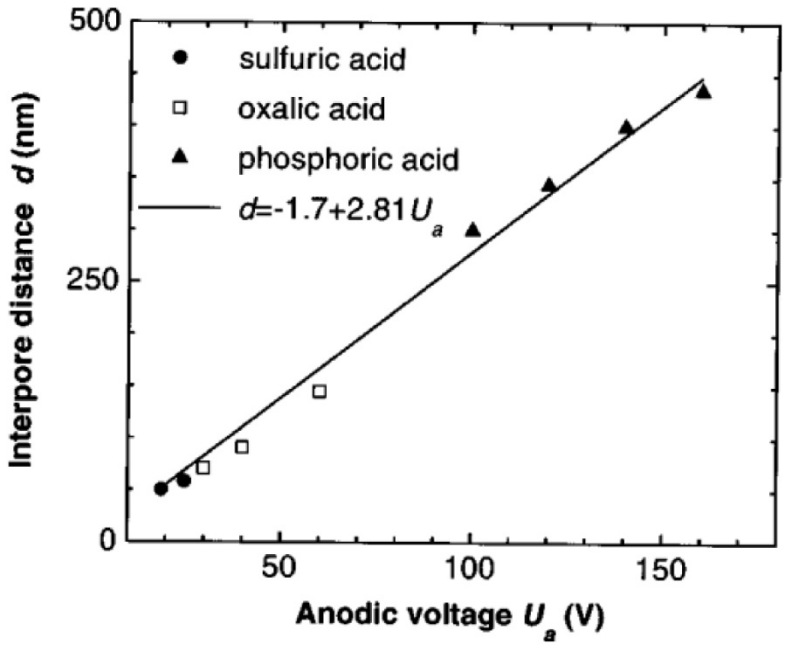

Figure 2.6 Interpore distance in self-organized porous alumina vs. anodic voltage for sulfuric, oxalic and phosphoric acid solution.[34]

We prepared a solution of 0.3M oxalic acid as an electrolyte since the oxalic acid shows a good controllability of interpore distance near 100 nm,[34] which is desirable range for filling fraction control by the following phosphoric acid etching. As shown in Figure 2.6, the interpore distance is controlled near 100 nm with ~40 V of the anodic voltage. The size of the nanopores is controlled by soaking the sample in a solution of 5 wt% phosphoric acid for different durations. Approximately, the etching rate of AAO is 2 nm/mins in the phosphoric acid. Note that the thickness of initial aluminum film is 250 nm and the thickness of AAO may be in a similar regime, thus the pore-widening time should be carefully controlled to prevent a removal of the whole AAO layer. The AAO membrane is finally used as an etching mask to create nanoholes in glass substrates.

2.2.3 RIE etching of glass

Reactive-ion etching (RIE) uses chemically reactive plasma to transfer a pattern by removing materials exposed to the plasma. The plasma is generated under a vacuum by an RF electromagnetic field (13.56 MHz). A so-called dark sheath is formed in the neighborhood between plasma and the surface of the wafer as well as chamber wall. The ions are accelerated by the

potential difference across the dark sheath, and the high energy ions from the plasma attack the wafer surface and react with it. Due to the mostly vertical delivery of reactive ions, RIE can produce very anisotropic etch profiles, which contrast with the typically isotropic profiles of wet chemical etching.

RIE using SF_6 gas is performed in an inductively coupled plasma-reactive ion etching (ICP-RIE) system, and the pattern depth is controlled by adjusting the etching time from 1 to 5 min. As far as silica glasses are concerned, various plasma chemistries, such as CHF_3/SF_6,[84] CHF_3/CF_4,[85] and SF_6/Ar[86] have been previously utilized. In general, sidewalls are expected to be free from any contamination or passivation during an etching process, which is advantage of fluorocarbon-based etchant for anisotropic etching profile. In our experiment, however, tapered structure is more desirable, which can be achieved by deliberating control of the side wall passivation. The metallic oxides contained in silica glasses often result in the production of nonvolatile compounds such as AlF_3 and NaF. In our case, the AAO mask as well as the metallic contaminant in glass substrate is expected to provide the nonvolatile compounds which is useful for the profile control. Fluorine-based plasma is generated by following conditions in RIE-ICP chamber (SLR-770, Plasma-therm) ; 10 mTorr pressure, 20 SCCM of SF_6 (or CF_4), 5 SCCM of Ar, 150 W RIE and 500 W ICP RF power.

2.3 Measurement technique

2.3.1 Spectral transmittance measurement

Figure 2.7 shows the light path from the monochromator to the integrating sphere through a transparent sample in the spectrophotometer (SolidSpec 3700, Shimadzu). A single wavelength light from the monochromator shines the sample positioned on the horizontal stage and pass through the sample. The transmitted light is collected in the integrating sphere.

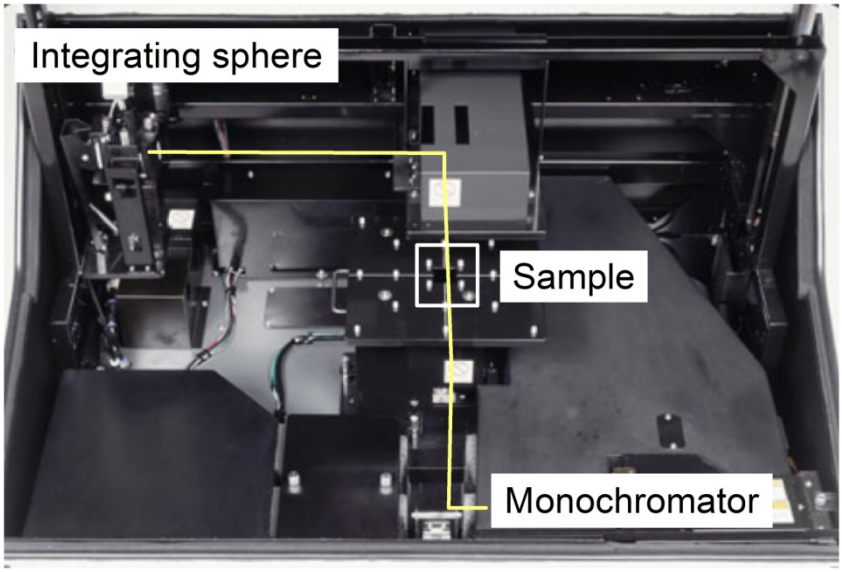

Figure 2.7 Simplified optical paths (yellow line) from the source to the detector. The sample is located on a horizontal stage, which enables the measurement of large samples.

The monochromator selects a narrow band of wavelength of light from a wider range of wavelengths from a 50 W halogen lamp. The white source from a halogen lamp is aimed at an entrance slit. The slit is placed at the effective focus of a collimator so that the light from the slit reflected from the mirror is collimated. The collimated light is diffracted from the grating and then is collected by another mirror which refocuses the light, is then dispersed on the exit slit. At the exit slit, the colors of the light are spread out like a rainbow and finally a narrow band of light can be selected at the exit of the monochromator. A rotation of the diffraction grating causes the band of colors to move to the exit slit, so that the desired wavelength is extracted and form the white beam. The monochromatic wave is guided by mirrors to shine on a specimen.

The transmitted light is collected by integrating sphere before detection. An integrating sphere consists of a hollow spherical cavity with its interior covered with a diffuse white reflective coating, with small holes for an entrance port. Light incident on any point on the inner surface is, by multiple scattering and reflections, distributed equally to all other points. Thus the effects of the original direction of light are minimized. Since all the light incident on the input port is collected, a detector connected to an integrating sphere can accurately measure the sum of the entire ambient light incident on

a small circular aperture. Two types of detectors are used to cover the wide range of wavelength. A photomultiplier tube detector for the visible wavelength (300 – 800 nm) and an InGaAs detector for NIR (800 – 1200 nm) are switched for the respective wavelength.

2.3.2 Angular transmittance measurement

Mimicking the path of the sun during a day, a homemade tool is designed for a light source to move along the edge of a half circle. A photograph of the homemade tool is shown in Figure 2.8(a). The tool consists of two half-circle frames. One is fixed to guide the other half circle part. A waveguide guides the broadband white beam from a halogen lamp. At the end of the waveguide, light faces a photodetector which is placed at the center of the setup. For the detection of incident light, a Si photodetector (DET 36A, Thorlabs), which is sensitive for the wavelength from 0.35 – 1.1 μm, is used and the DC voltage-out from the photodetector is monitored with a digital multimeter. Since the voltage from the photodetector by itself is a relative value, it needs to be normalized, dividing by the incident light without any material for every angle. This normalization procedure is similar to that has been done for simulations.

In Figure 2.8(b) the normalized transmittance of a bare glass is compared with the calculated values by Fresnel's equation. Even though the measured value is always lower than the predicted value at each angle, probably due to the additional optical losses from guided modes in the glass slab, the curve of the measured transmittance shows the similar angle dependence to the predicted curve. As the angle increases, the gap between two curves become larger, which implies that the guided modes throughout the glass slab become more significant.

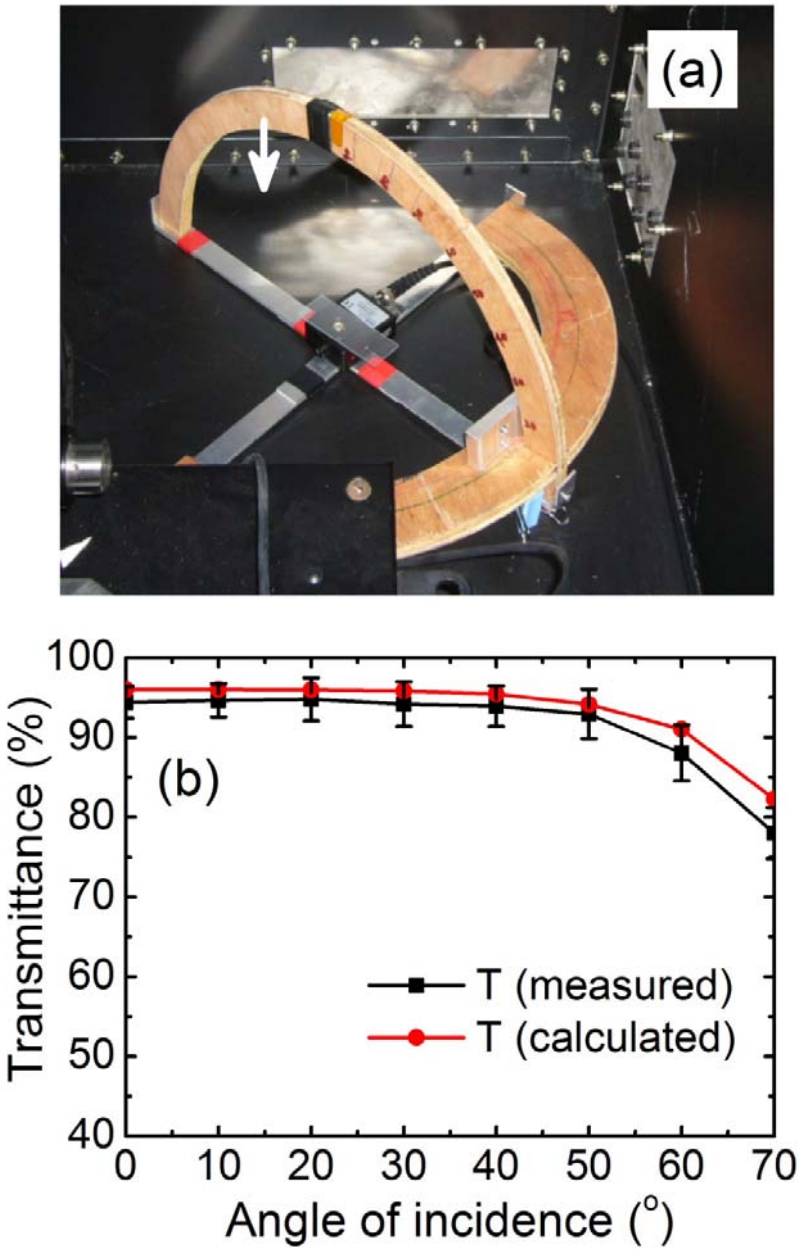

Figure 2.8 (a) A homemade tool for angle dependent transmittance (the arrow indicates the position of light source) and (b) the comparison of measured transmittance with Fresnel's calculation at every 10°.

2.3.3 Solar cell measurement

A solar simulator provides artificial light approximating natural sunlight. The purpose of the solar simulator is to enable controllable indoor test of solar cells under laboratory conditions. However, the definition of artificial solar radiation can vary significantly with locations, atmospheric conditions (including cloud cover, aerosol content, and ozone layer condition), time of day, earth/sun distances, and solar rotation and activity.[87] Since

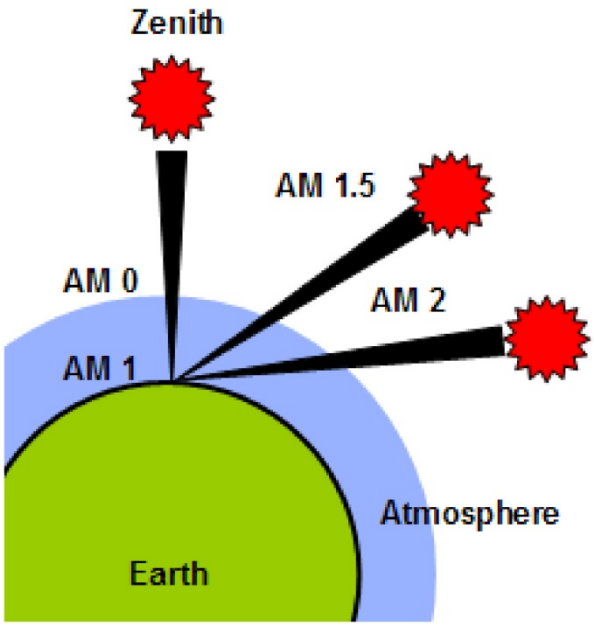

Figure 2.9 The path length in units of Air Mass changes with the zenith angle.

the solar spectra depend on so many variables, standard spectra have been developed to provide as a basis for simulator design. The American Society for Testing and Materials (ASTM) published three spectra,[88] AM 0, AM 1.5 Direct, and AM 1.5 Global as shown in Figure 2.9. When sunlight passes through no air mass, the extraterrestrial spectrum is called the "Air Mass 0" spectrum. With the sun overhead, direct radiation that reaches the ground passes straight through all of the atmosphere and all of the air mass. We call this radiation "Air Mass 1 Direct" (AM 1D) radiation and for standardization purposes a sea level reference site is utilized. The global radiation with the sun overhead is similarly called "Air Mass 1 Global" (AM 1G) radiation. AM 1.5 Global is corresponding to the radiation at a zenith angle of 48.2°.

A solar simulator uses AM 1.5 filter to modify the spectrum of Xenon lamp for a better match to the standard solar spectra. The solar-like spectrum is collimated, simulating the direct terrestrial beam and allows the characterization of solar cells. Using the solar simulator, the performance of solar cells can be electrically characterized. A solar cell is basically a PN junction diode which can generate electrical power when illuminated. The typical IV characteristic of a diode is observed without illumination.

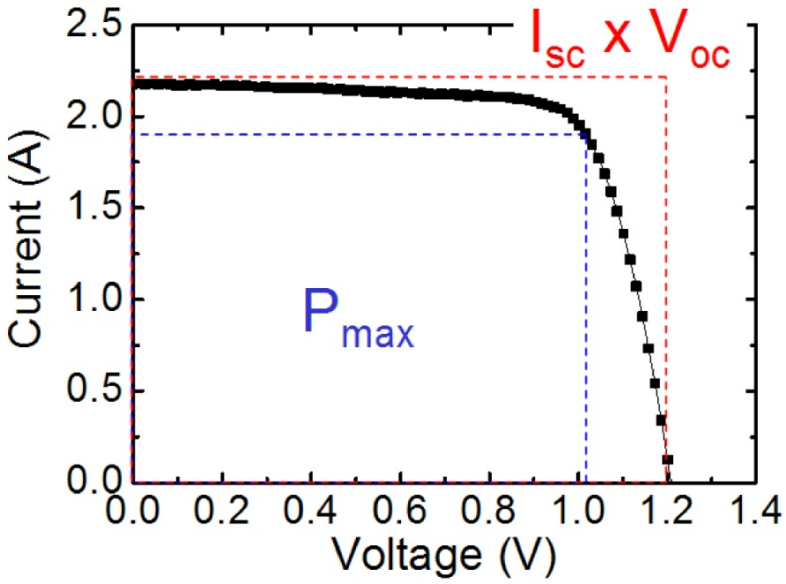

Figure 2.10 Forward bias IV measurement of a solar cell under illumination of AM 1.5.

There is no current flow through the diode, unless there is external potential applied. With irradiation, the IV curve shows non-zero current without any external field as shown in Figure 2.10. Several parameters are used to characterize the efficiency of solar cells, including the short circuit current (I_{sc}), the open circuit voltage (V_{oc}), the maximum power (P_{max}), the energy conversion efficiency (η_{eff}), and the fill factor. The fill factor is a measure of how far the IV characteristics of an actual PV cell differ from those of an ideal cell which is defined the ratio of P_{max} to the product of I_{sc} and V_{oc} namely, inner blue square to outer red square in Figure 2.10. A large fill factor is desirable with square-like IV curve but the loss by series and shunt resistance decreases the fill factor and efficiency. Among the characteristic parameters of a photovoltaic device, we focus on the measurement of I_{sc}, since I_{sc} is the most sensitive parameter to the amount of incident photons, and it is easily and directly measurable. Moreover, I_{sc} is directly measurable in outdoor environments using a transducer which converts the current to the voltage in order to measure high currents in solar cells. Packaging a solar cell and electrical characterization under outdoor environments will be discussed in chapter 6.

Chapter 3: Design of Highly Transparent Glass

3.1 Introduction

Glass is an optically important material for solar cell applications, as it is one of the few hard solids which can transmit most of light in the visible spectrum. Although the optical loss by reflection on a transparent glass surface is ~4% at normal incidence,[16] which seems negligible since the glass still looks transparent, the reflection is considerable for photovoltaic devices. Furthermore, the reflection dramatically increases with increasing the angle of incidence. Thus, improving the optical property by surface treatment is attractive to achieve higher performance of photovoltaic devices.[17] Learning from nature, a textured surface with subwavelength structures is known to show omnidirectional and broadband antireflective properties.[77] Designing proper dimensions of nanostructures on a glass is highly desirable to realize the highly transparent surface. Here, numerical studies for the dimensional optimization have been carried out using a finite difference time domain (FDTD) method and the results are compared with theoretical formula.

3.2 Simulation method

The simulations are carried out by the software MEEP, which can calculate reflectance and transmittance of electromagnetic waves in dielectric and metallic media.[81] We focus on the study of dimensional effects of nanostructures on optical transmission. The schematic diagram of the modeling structure is shown in Figure 3.1. Electromagnetic waves with a broadband spectrum are generated over the textured medium and the propagating angle varies from 0 to 75°. A perfect matched layer (PML) is applied in the *x* and *y* axis to decrease the error induced by the reflected waves from the boundary of the simulated area.[89] Moreover, the wider *x* dimension is used in order to minimize the error due to absorption at both side walls. The shape of structures is defined either as cylinder or cone with

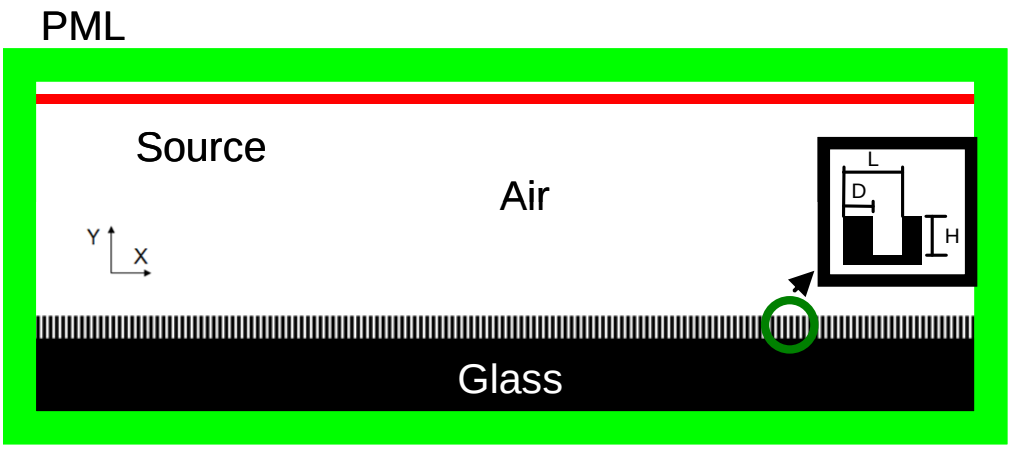

Figure 3.1 Schematic of the simulated antireflective structure. Outer closed line (green) represents PML and the upper line (red) near top PML indicates the place where electromagnetic waves are generated. The black color shows the area with higher refractive index, which is glass of refractive index 1.5 in this simulation. In the inset, dimensions of nanostructures are given with lattice spacing (L), diameter (D) and height (H), respectively.

various dimensional factors such as diameter, height, and spacing between two structures. We choose the refractive index, $n_0 = 1$ for air, and $n_s = 1.5$ for a glass substrate. The dispersive refractive index and the effect of extinction coefficient are ignored in this study, assuming loss-free and wavelength independent propagation in the given space. The transmittance is the average values of TE and TM polarized waves, assuming unpolarized light.

3.3 Comparison of nanostructured layer with a single antireflective film

First, we calculate transmittance through a single layer of antireflective coating which has a thickness of a quarter wavelength of light. The ideal refractive index of single antireflective coating can be found by[16]

$$n^2 = n_0 n_s \qquad \text{(Eq. 3.1)}$$

In addition, the maximum transmittance can also be obtained, if the thickness satisfies

$$d = \frac{\lambda}{4n} \qquad \text{(Eq. 3.2)}$$

where d and λ are the thickness of a thin film and wavelength of light, respectively.

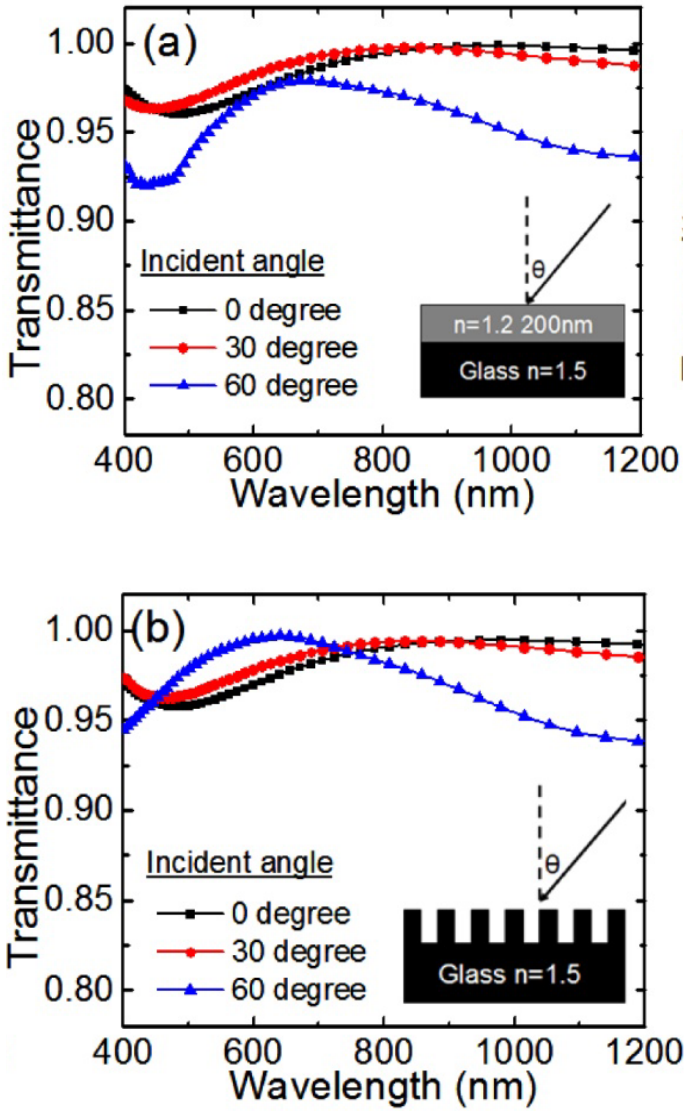

Figure 3.2 Transmission spectrum (a) for single layer thin film coating with refractive index 1.22 and 200 nm thickness and (b) for nanostructured surface with H = 200 nm, D = 80 nm and L = 200 nm. (Inset) Schematic drawing of simulation structure with (a) a thin film and (b) nanostructured layer.

As expected from the equations above, the antireflection is effective only at a target wavelength for the normal angle of incidence. For example, a 200 nm thick film with a refractive index of 1.22 shows maximum transmittance at the wavelength of ~970 nm between glass and air. The simulation results in Figure 3.2(a) agree well with the theoretical prediction. Transmittance drop is also observed with the increase of incident angle. With a single antireflective film, the transmittance abruptly decreases with an angle more than 60°. In Figure 3.2(b), a nanostructured layer is simulated to compare the antireflection effect with a single layer coating as shown in Figure 3.2(a). According to the effective medium theory,[16]

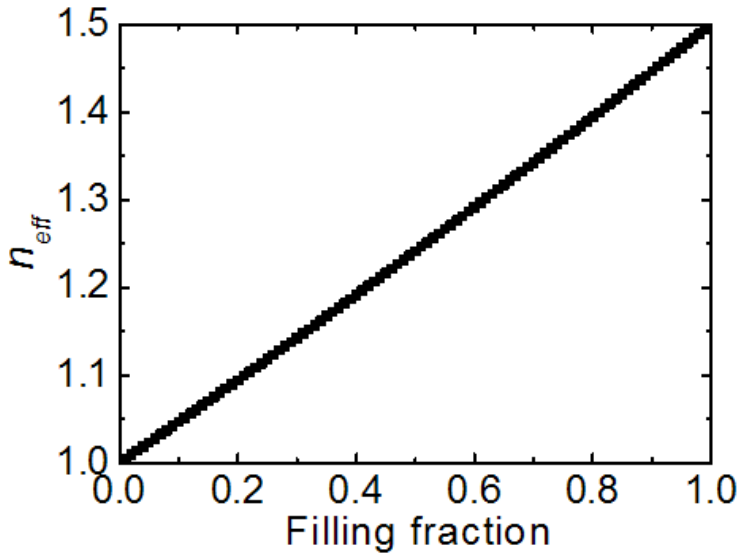

Figure 3.3 Predicted effective refractive index (n_{eff}) of the layer with cylindrical structures as a function of filling fraction (f).

we assume that the layer with cylindrical structures can be considered as a thin coating, since the dimensions are smaller than the wavelength of incident light and the cylindrical shape induces the uniform filling fraction along the thickness. A glass surface is covered with cylinders with a diameter of 80 nm, a height of 200 nm and a spacing of 200 nm, where the effective refractive index of the layer can be defined as 1.2. Here, as shown in Figure 3.3, the effective refractive index of the structured layer is calculated by

$$n_{eff} = \left[f n_s^q + (1 - f) n_{air}^q \right]^{\frac{1}{q}} \qquad \text{(Eq. 3.3)}$$

where q = 2/3,[13] and f is the filling fraction. In Figure 3.2(b), we find that the transmittance curves of the nanostructured layer are similar to that of a single film in Figure 3.2(a) for normal incident and 30° tilted angle. Therefore, the cylindrical layer is acting as a homogeneous medium whose effective refractive index is the same as a single film with the calculated refractive index based on Eq. (3.3). In both cases, similar antireflective properties are observed for wide wavelength ranges and for the incident angles less than 60°. However, the transmittance shows a difference at 60° of incident angle as presented in Figure 3.4. The structured homogeneous layer

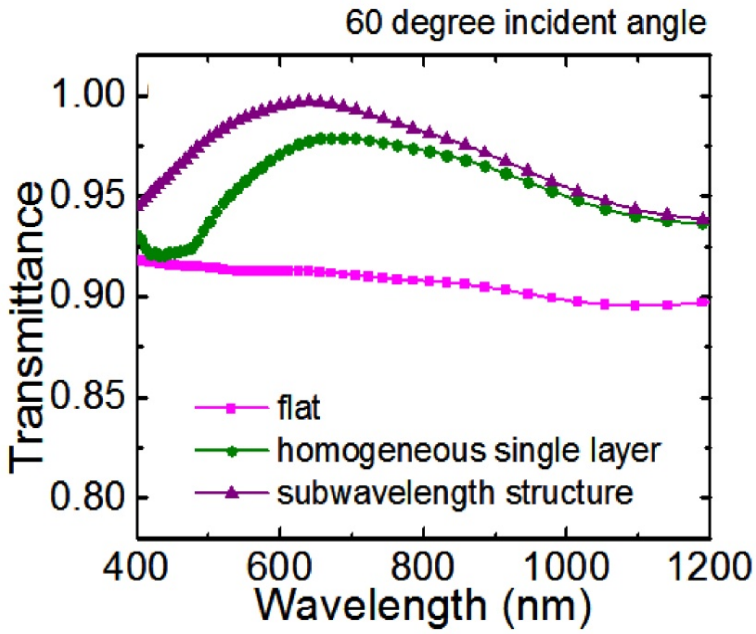

Figure 3.4 Comparison of transmittance for different surface structures at the 60° of incident angle.

exhibits better transmission at the given spectral ranges than the non-coated case or single layer coating for the oblique incidence of light. In short, the cylindrical structured layer has a uniform effective refractive index across the thickness and behaves like a single film, suppressing the reflection only at particular wavelengths. However, the nanostructured layer is more effective for the omnidirectional antireflective purpose than a single layer antireflective film.

3.4 Effects of the dimensional parameters

We investigate the effects of the dimensions of nanostructures such as the height and filling fraction (diameter and lattice constant) on optical transmittance for various incident angles and wavelengths. First, the height of the cylindrical structures varies from 0 to 800 nm with a fixed filling fraction (200 nm of space between two cylinders and 80 nm of the diameter). As shown in Figure 3.5(a), the best omnidirectional antireflective property is observed from the 200 nm height condition with ~3% increase of transmission at all angles. For the normal incident light, the broadband antireflective property is observed at the wavelength from 600 to 1200 nm from the structure with 200 nm height as depicted in Figure 3.5(b).

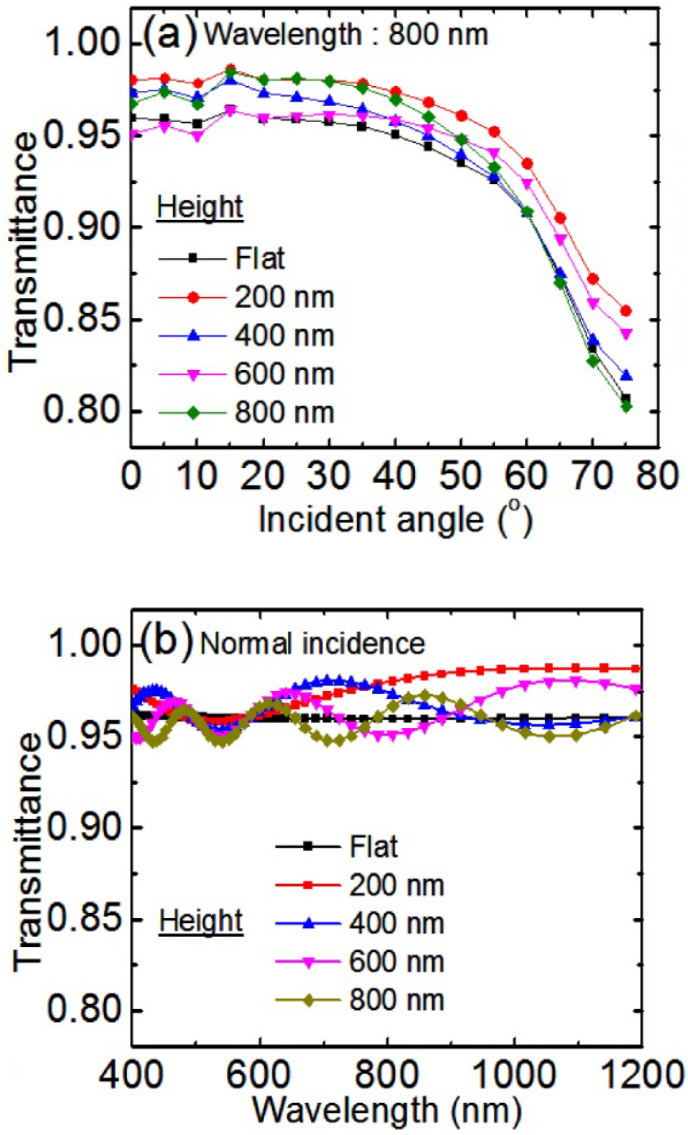

Figure 3.5 Effects of structural dimensions on (a) omnidirectional and (b) broadband transmittance. Height of the nanostructures varies from 0 to 800 nm, while diameter (40 nm) and lattice spacing (200 nm) are fixed.

The effect of filling fraction is also studied by changing the diameter of structure from 0 to 160 nm. The height of the structure is fixed with 400 nm. In Figure 3.6(a), the omnidirectional antireflective property is observed from the structures with diameter ranging from 40 to 80 nm, which is corresponding to 1.09 and 1.19 of the effective refractive index (Figure 3.3). The transmission spectrum in Figure 3.6(b) shows

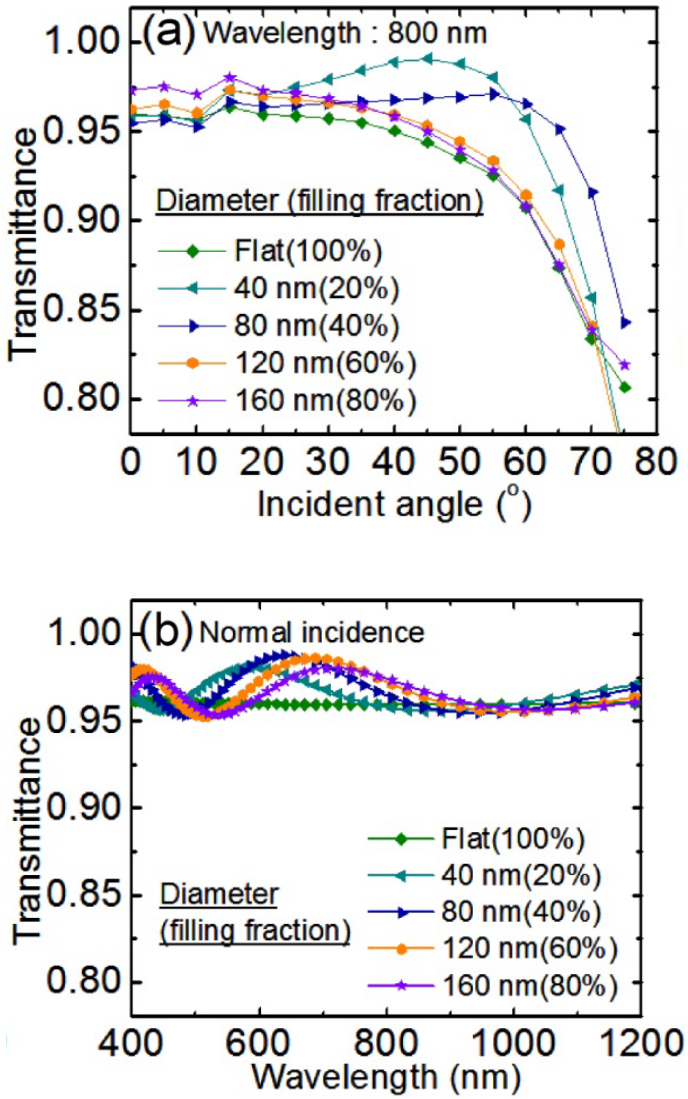

Figure 3.6 Effects of filling fraction of nanostructures on the transmittance as a function of (a) incident angle and (b) wavelength. Diameter of the nanostructures varies from 0 to 160 nm with fixed height (400 nm) and lattice spacing (200 nm).

only a slight shift of the resonance peak by the variation of the effective refractive index and no significant enhancement is observed. This might be attributed to the homogeneous property originated from the cylindrical shape which has an uniform effective refractive index across the thickness. From the previous calculations, we extract the optimal dimension of cylinders for broadband and omnidirectional antireflection such as a height of 200 nm, a spacing of 200 nm and a diameter of 80 nm.

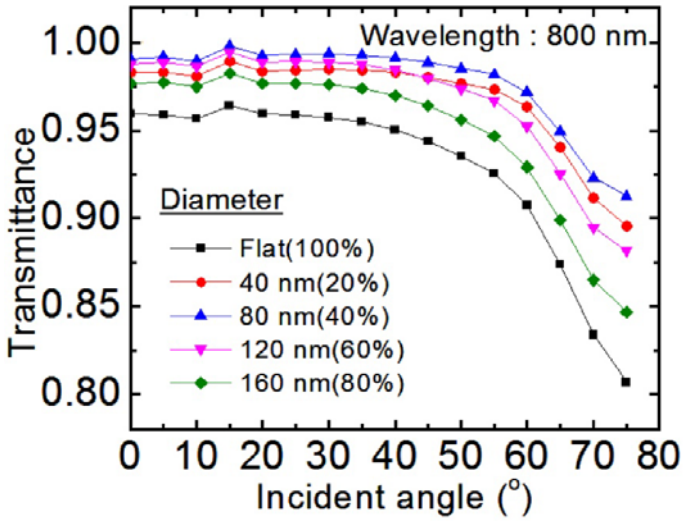

Figure 3.7 Omnidirectional antireflective property of nanostructured surface with optimized dimensions of a cylinder.

3.5 Proposal for optimized dimension for antireflective structures

The omnidirectional antireflective property is also studied with the optimal dimensions as seen in Figure 3.7 by changing the filling fraction. With a fixed lattice spacing of 200 nm, the filling fraction can be varied by changing the diameter of cylinders. In Figure 3.7, the transmittance of the nanostructured layers show the enhanced transmission in all cases. Especially, the optimized structure with a diameter of 80 nm demonstrates an enhancement of 10% in transmittance at angle of incidence of 75° compared to that of flat surfaces. The effect of the enhanced transmission property is more prominent in the oblique angles of incidence.

The notable feature of the cylindrical shape is a homogeneous antireflective layer, which can be considered as a single layer film. Generally, the gradual change of the refractive index is more effective for omnidirectional antireflection due to the optical impedance matching at the interfaces, which reduces reflection.[18] Even though the antireflection property is not fully optimized with the cylindrical structures, the nanostructured cylindrical layer shows the omnidirectional property. For the further studies, we compare the nanostructured cylindrical layer with a gradual index varying layer, such as a conical structure.

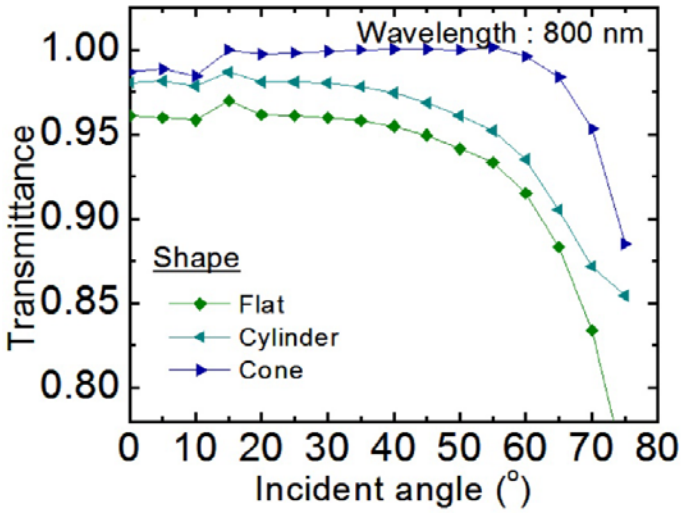

Figure 3.8 Effect of shape of nanostructure: cylinder and cone shaped structures with same dimensions.

The gradual variation of the refractive index from air to the substrate maximizes the optical transmission. In Figure 3.8, conical shapes, with the same base diameter, height and spacing used for cylindrical shapes, present a higher transmittance at all angles than the optimized cylindrical strictures, since the refractive index increases gradually by the gradual variation of the effective filling fraction. However, the practical fabrication techniques are still challenging to fully support the graded index profile with nanostructures.

3.6 Conclusion

We have performed simulation works to confirm the effect of nanostructures on broadband and omnidirectional antireflective properties. According to the effective medium theory, the subwavelength structures can be considered as homogeneous media with an effective refractive index, which is determined by the filling fraction. With a fixed height of the antireflective layer, we have varied the filling fraction and compared the antireflective properties with a single layer antireflective coating. We found that the omnidirectional property is enhanced by the nanostructured layer, even though the index profile is not gradually changing across the height. In addition, we also confirm that the gradual index profile with cone-shaped nanostructures shows the superior omnidirectional antireflective properties. However, the development of nano-fabrication techniques should be mature to realize the antireflection properties with the graded index profile.

Chapter 4: Enhancement of Optical Transmission

4.1 Introduction

In order to demonstrate enhanced transparency by optimal dimensions, it is necessary to generate a graded refractive index layer on an optically transparent substrate such as glass. In practice, a gradual change of the refractive index can be achieved by changing the filling fraction of materials in the nanostructures.[18] A close-packed design is commonly used to achieve a nominally continuous variation of filling fraction from top to bottom of nanostructures without any abrupt change in the refractive index thus resulting in an suppression of reflection.[90] Herein, the tapered profile of the V-shape nanohole arrays provides more continuous variation of the refractive index on the glass for antireflective purpose. Besides, direct patterning of glasses, unlike other methods where residual organic materials play a role as antireflective structures,[39, 91] exhibits higher mechanical stability and better durability than coatings, since no foreign materials are involved, and also can be used over a broad thermal range.[92] The broadband and omnidirectional antireflective effect of the proposed nanostructures is confirmed by measuring the transmittance of the patterned glasses and also tested with a solar cell.

4.2 Preparation and experiments

The schematic diagram of the fabrication process for the antireflective structures is shown in Figure 4.1. Bare borosilicate glass substrates are cleaned with acetone in an ultrasonic bath followed by isopropyl alcohol (IPA) and deionized (DI) water rinse. After cleaning, 250 nm thick aluminum film is deposited by electron beam evaporation on cleaned glass substrates (Figure 4.1(b)), followed by anodization under a constant voltage of 40 V in 0.3 M oxalic acid solution to created porous aluminum oxide with randomly distributed pore patterns (Figure 4.1(c)).[34] The size of the nanopores is

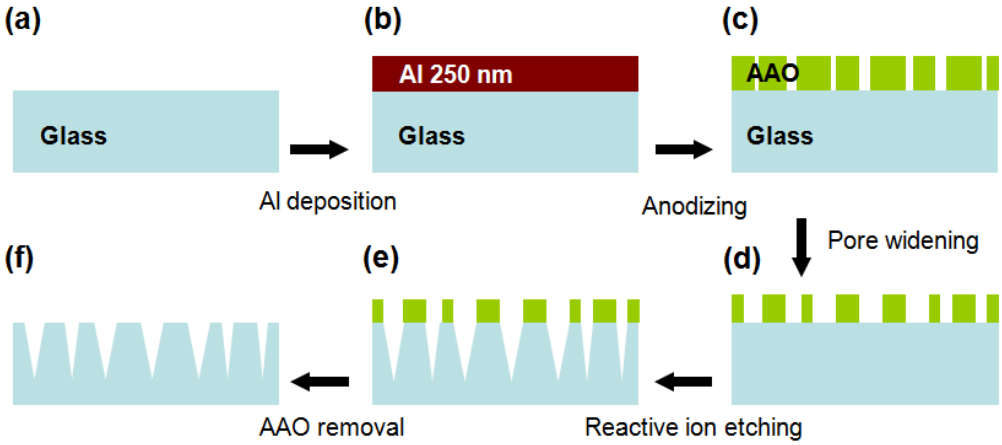

Figure 4.1 Schematic illustration of the process for preparing antireflective structures.

controlled by soaking the sample in a solution of 5 wt% phosphoric acid for different durations (Figure 4.1(d)). The anodized aluminum oxide (AAO) structures are used as an etching mask to create nanoholes in the glass substrates via reactive ion etching (RIE). Thin AAO layer is also etched slowly during the RIE etching process, however, it is thick enough to be used as an etching mask. Reactive ion etching using SF_6 gas is performed in an inductively coupled plasma-reactive ion etching (ICP-RIE) system, and the pattern depths are controlled by adjusting the etching time from 1 to 5 min (Figure 4.1(e)). Finally, AAO template is removed by phosphoric acid (Figure 4.1(f)).

4.3 Fabrication results

Figure 4.2 shows SEM images of nanohole arrays formed by the AAO process after the pore widening process (Figure 4.1(d)). Although it is reported that a highly ordered pattern can be generated by a two step anodizing method,[93] we used an one step anodizing method to simplify the fabrication and to generate randomly distributed nanostructures. The randomized structures are reported to have a better broadband transmission which is undesirable for filter applications, but very useful for solar cell applications.[39]

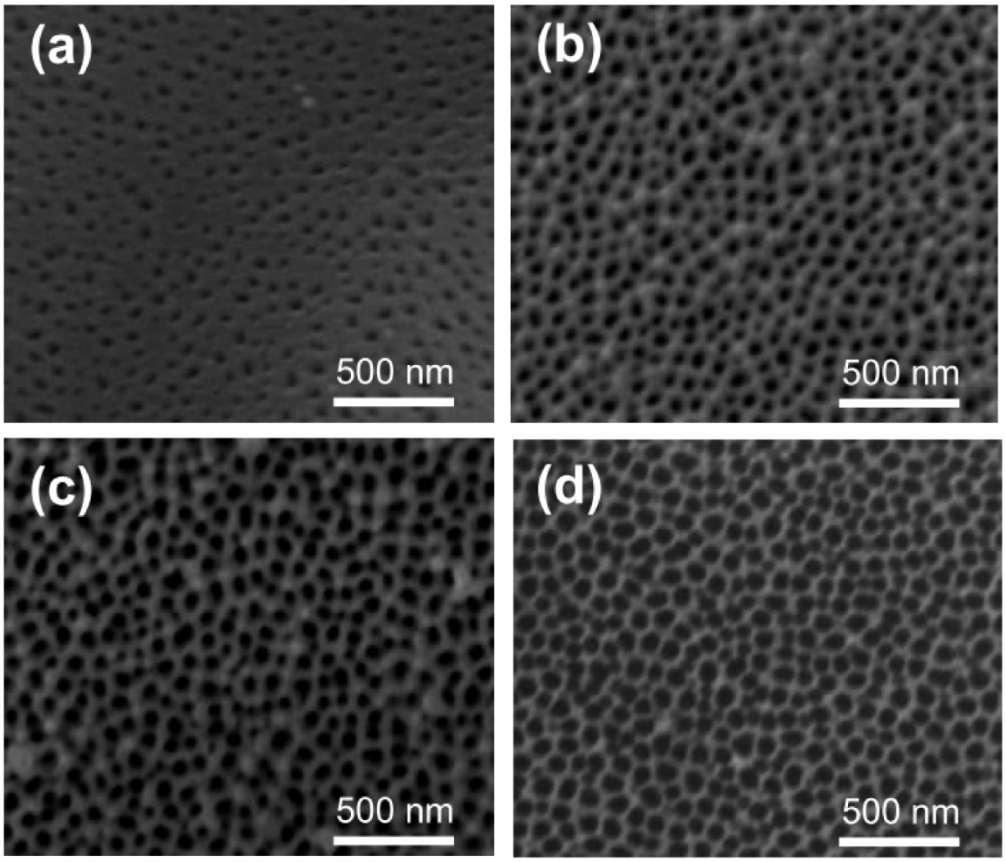

Figure 4.2 SEM images of the AAO nanohole structures formed by different pore widening conditions, leading to various diameters of (a) 51.5 nm, (b) 66.8 nm, (c) 74 nm, and (d) 85.6 nm.

Table 4.1 Mean diameters, standard deviations of diameters, and filling fraction of holes at the top surface of AAO layers for different pore widening times.

Pore widening time (min)	Hole diameter (nm)	Standard deviation (nm)	Fraction of holes at surface (%)
50	51.5	22.52	23.33
60	66.8	25.07	37.55
70	74	34.66	39.17
80	85.6	39.10	54.66

The prepared samples in Figure 4.2 have an array of nanoholes with diameters ranging from 51.5 to 85.6 nm. The holes are distributed randomly on the whole surface with an average spacing of 100 nm between the holes regardless of the pore widening time. Table 4.1 shows the dependence of the hole diameter on the pore widening time. The air filling fraction of

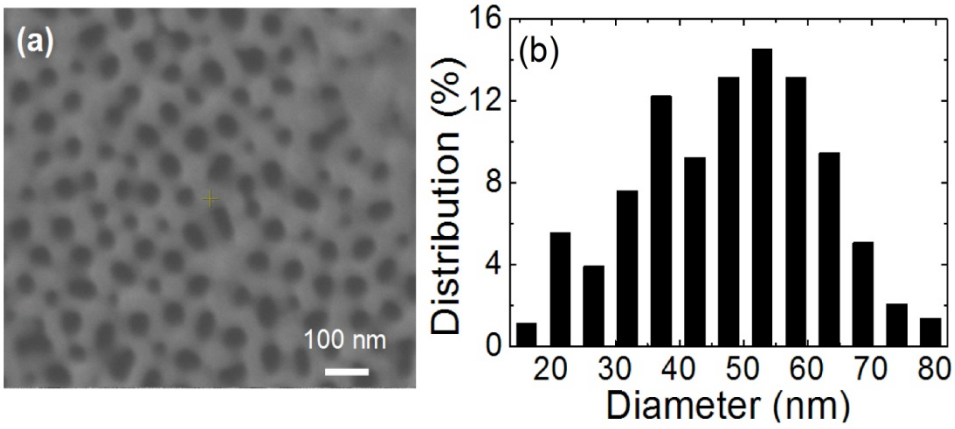

Figure 4.3 (a) SEM images of glass surface after etching for 4 min. AAO pattern is formed with 50 min of pore widening time and removed after etching. (b) Size distribution of nanoholes on glass.

the AAO templates changes from 23.33 to 54.66% as the soaking time, thus the hole diameter, increases. Though larger holes are preferred in the AAO patterns in order to obtain an effective refractive index close to that of the air after transferring the patterns to glass, longer duration of pore widening causes the thinning of AAO layers, which is undesirable for etch masks.

Figure 4.3(a) shows the top view of the etched patterns after 4 minutes of etching and Figure 4.3(b) shows the size distribution of nanoholes with a mean diameter of 48 nm, which is smaller than the diameter (51.5 nm) of the AAO template. In order to confirm there is no residual AAO in our samples after removing by phosphoric acid, we performed energy-dispersive X-ray spectroscopy (EDX) as shown in Figure 4.4. The element analysis shows the remaining amount of aluminum after whole fabrication processes is negligible, which means that no residue affects the optical transmission.

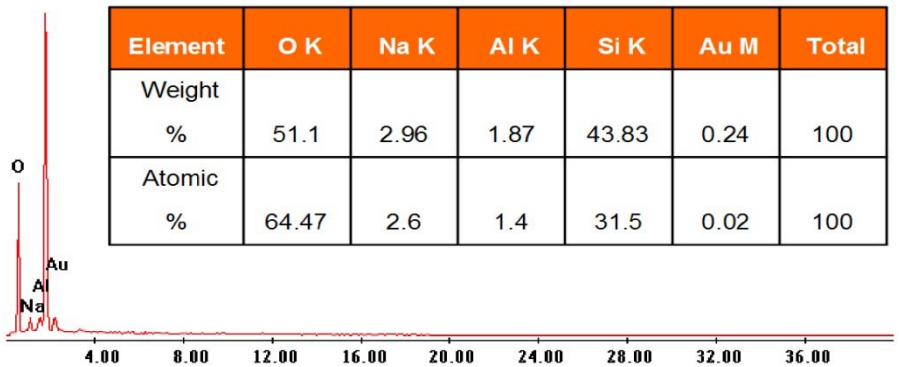

Element	O K	Na K	Al K	Si K	Au M	Total
Weight %	51.1	2.96	1.87	43.83	0.24	100
Atomic %	64.47	2.6	1.4	31.5	0.02	100

Figure 4.4 EDX analysis after AAO removal. No residues are detected on a nanohole-patterned device.

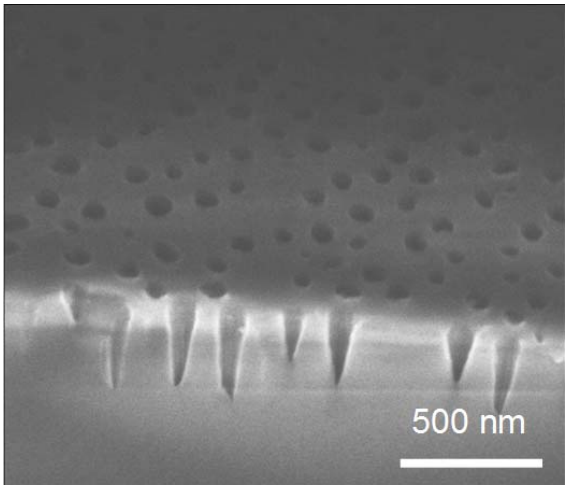

Figure 4.5 SEM images of 45° oblique view of etched pattern in glass substrate.

The profile in Figure 4.5 demonstrates the 400 nm deep nanoholes are generated. The nanohole arrays are normal to the surface with a V-shape profile, which creates the gradual variation of refractive index at the both ends of nanostructures. Fluorine based gas has been known to generate etch inhibitor during the etching process and the inhibitor is deposited on the side wall to protect the wall from reactive ions.[94] Excessive use of SF_6 prohibits side wall etching which relatively increases the etching reaction at the center of nanoholes, leading to the V-shaped patterns.[95]

4.4 Broadband and omnidirectional antireflective property

In Figure 4.6, the spectral transmittance of glass substrates patterned on one surface with different widening times and etching times is compared with that of the bare glass. The optical transmission through the glass increases from 92.0 to 94.5% with nanopatterning as shown in Figure 4.6. By increasing pore widening time (Figure 4.6(a)), the samples exhibit a higher transmission of 93%, 94%, and 94.5% corresponding to the hole diameters of 51.5 nm, 66.8 nm, and 85.6 nm in the AAO layer, respectively, in the wavelength range above 500 nm. Close-packed nanoholes with a larger diameter show an enhanced antireflective behavior due to more smooth change of the refractive index between the glass and the air. Figure 4.6(b) shows

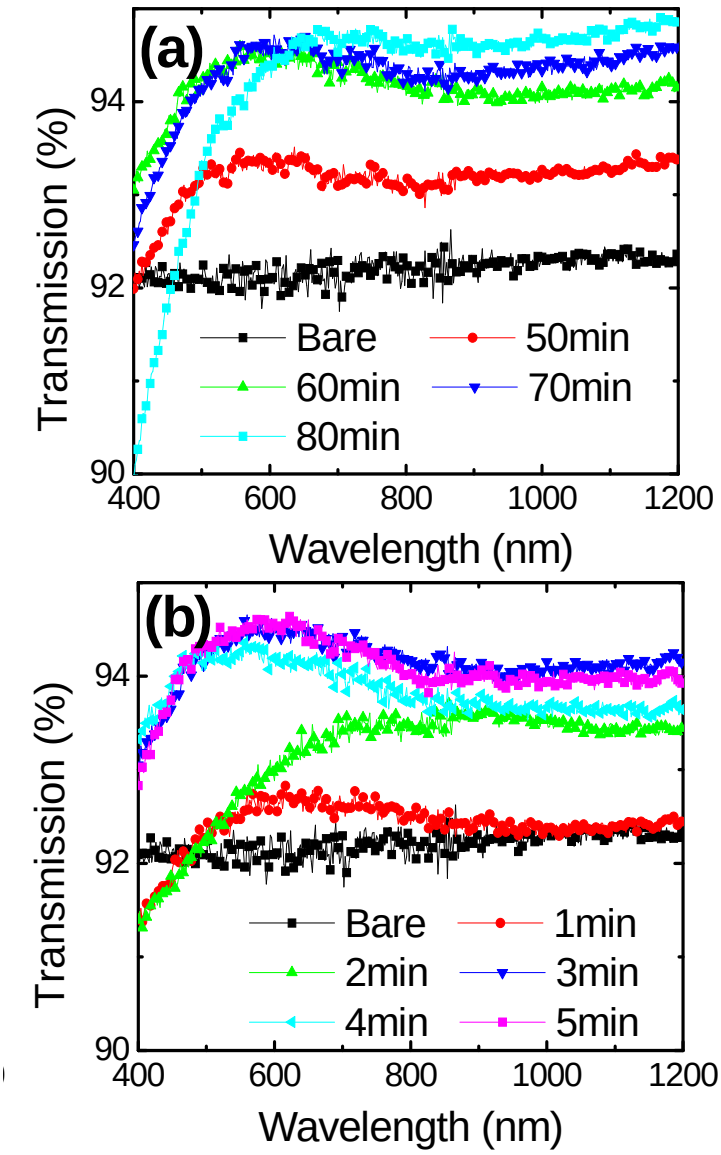

Figure 4.6 (a) Optical transmittance of patterned glass at normal incidence for different diameters adjusted by pore widening time from 50 to 80 min followed by 4 min of etching. The bare glass data is shown as a reference. (b) Transmittance comparison for different hole depths etched for 1 to 5 min. Pore widening time is 60 min.

the depth dependence of antireflective property of nanohole structures with a pore widening time of 60 min. The samples with more than 3 min etching time show similar transmittance of 94.5% in the wavelength range above 500 nm. It indicates that an etch depth of 300 nm (3 min etching) is sufficient due to the gradual variation of the refractive index at the bottom of V-shaped nanoholes. It is reported that the height of pyramidal nanostructure has less dependence on antireflective characteristic.[22] For a better transparency,

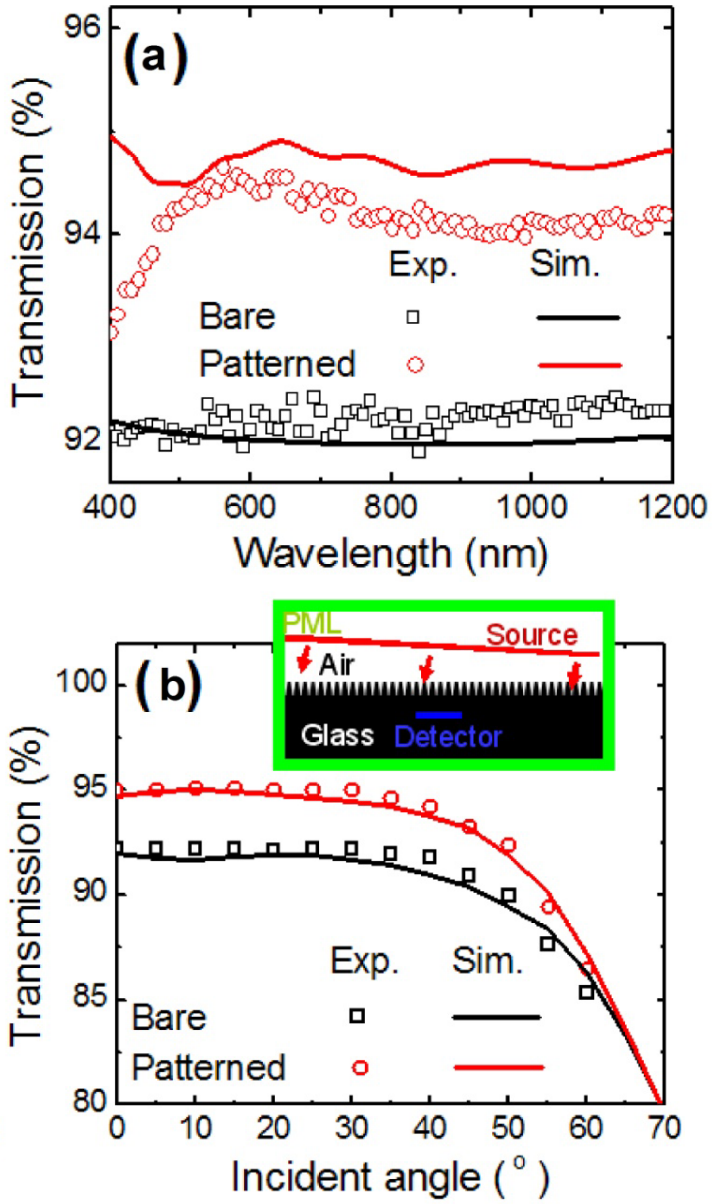

Figure 4.7 (a) Transmission comparison between the experimental data (symbols) and the simulated data (lines) of the optimal antireflective structure. (b) Incident angle dependence of transmittance (Inset) Schematic illustration of the simulated structure.

double sided patterning in glasses can be employed to reduce the transmission loss at both interfaces. The reduction of transmission at a range less than 500 nm is explained by light scattering and absorption loss, induced by the fabrication process and defects on the surface.[52] Figure 4.7(a) shows the comparison of spectral transmission for the bare glass and the optimized patterned glass, along with the simulation results of the same structures in the

case of normal incident angle. The dimensions of the nanohole array in the optimized sample are ~60 nm diameter and 300 nm depth. In the finite difference time domain simulations, the periodicity is fixed at 100 nm and the height of the structure is 300 nm with a refractive index of 1.5, which represents that the 60% of surface is glass and 40% is filled with nanoholes in two dimensional simulation structures. The computational geometries are shown in the inset of Figure 4.7(b). Another advantage of the antireflective structures with gradually varying refractive index is an omnidirectional antireflective property. We have performed angle dependent transmission measurements, where a photodetector is placed under the glass and a white light source is located above the sample simulating the movement of the sunlight. In Figure 4.7(b), the enhancement of transmission of the patterned glass is clearly shown at all angles. There is at least 2% better transmission in the antireflective structures at all incident angles. The measured results are not perfectly matched with the simulation result for incident angles above 50° due to the guided loss of light through the glass substrate.

4.5 Conclusion

Antireflective coatings based on an AAO method are studied for fabricating hole-type nanostructures on the glass substrates combined with a dry etching technique. The glasses with tapered nanoholes of sub-100 nm diameters show enhanced transmission due to a continuous variation of the filling fraction at both ends of nanostructures. The array of randomly distributed nanoholes also shows prominent improvement in optical transmittance in wide spectral and wide angular ranges, which can be directly applied in solar cell glass packaging for efficient light harvesting.

Chapter 5: Evaluation of Self-cleaning Effect

5.1 Introduction

In the past decades, there have been many attempts to obtain self-cleaning surfaces. In addition, antireflective properties of nanostructured surfaces have encouraged the convergence between self-cleaning structures and antireflective structures[57, 96-98] due to their potential use in photovoltaic cells and other outdoor applications. However, most previous studies on simultaneously pursuing both the self-cleaning effect and an antireflective property in a particular system have not examined their endurance characteristics in outdoor environments. Outdoor testing of self-cleaning and antireflective coatings is necessary to evaluate their degradation, when they are exposed to outdoor natural environments.[99, 100] Here we present the development of highly durable, antireflective, and self-cleaning glass surfaces via a simple bottom-up nanopatterning technique and consequent surface energy modifications. We evaluate the effectiveness of our self-cleaning coatings by monitoring the variation of contact angle (CA), optical transmittance, and photovoltaic performance under outdoor conditions for 12 weeks.

Both the optical transmission of bare glass and solar cell performance packaged with such a glass decrease, as dirt and dust accumulate on the glass surfaces. By utilizing superhydrophilic glasses that we have designed without any chemical coatings, we obtain less variation of transmittance and solar cell performance over long term testing compared to other hydrophilic, hydrophobic, or superhydrophobic glasses. Unlike other methods where the chemical coatings play a main role for the self-cleaning effect,[57] our non-coated superhydrophilic glass system will be particularly useful for practical outdoor applications, in which both the self-cleaning and antireflective effects are of concern, and where degradation of a chemical coating over time will not be of concern.

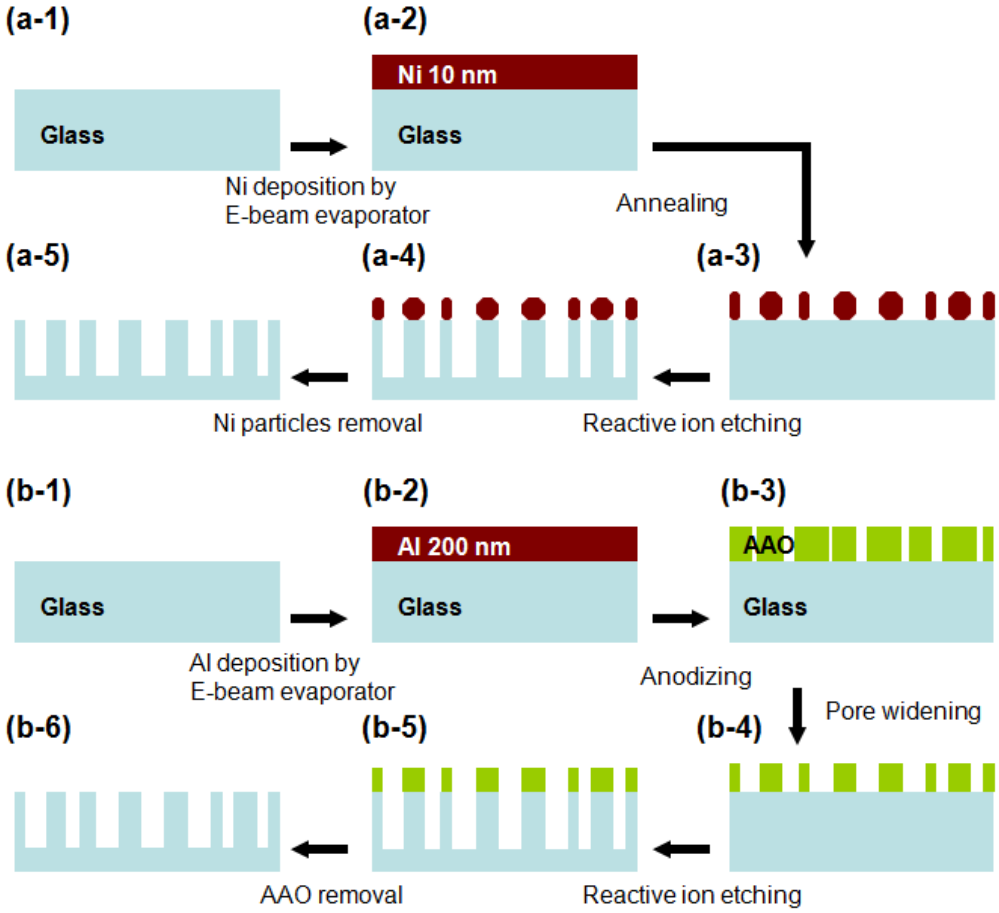

Figure 5.1 Fabrication sequences for randomly distributed (a) nanopillars and (b) nanoholes.

5.2 Sample Preparations

The schematic diagrams of nanopatterning process for randomly distributed nanopillar and nanohole patterns are shown in Figure 5.1. The nanopatterns are fabricated by inductive coupled plasma-reactive ion etching (ICP-RIE). Ni nanoparticles and anodized aluminum oxide (AAO) nanohole templates are used as an etching mask.[101, 102] For pillar structures a 10 nm thick Ni film is transformed into nanoparticles, when annealed at 600 °C for 5 min. The randomly distributed nanoparticles with diameters less than 100 nm on the glass substrate are used as a mask for dry etching, creating random nanopillar arrays. In case of hole structures, the diameter of holes is determined by the pore widening step. After the pore widening for 80 min in phosphoric acid, most of the holes have diameters from 50 to 70 nm with a ~100 nm of spacing. The hole pattern is transferred onto glass surface by dry etching. Chemical functionalization with 1H, 1H, 2H, 2H-

perfluorodecyltriethoxysilane (PFTS) for the formation of superhydrophobic surfaces on patterned glasses and bare glasses was performed subsequently by exposing the samples to PFTS through gas-phase evaporation in a desiccator under vacuum for 5 hours. Octadecyltricholorosilane (OTS) coating was prepared by dipping the patterned samples into an 1 mM solution in dry toluene for 10 s followed by sonication in toluene two times for 30s. This process of dipping and sonicating was repeated two times. Hydrophilic perfluoropolyether (PFPE) coating was deposited by using a commercial Z-Dol 4000 (0.2 wt%) in PFPE solvent (H-Galden). The samples were dipped into the PFPE solution, held for 1 min, and then withdrawn at a dipping speed of 2.1 mm/s. Surface morphology of each surface was investigated by a SEM (FEI NanoSEM 230). The images obtained from the SEM were analyzed by free software (Image J). Water CA measurements were performed with a water CA measurement system (VCA Optima, AST Products). A spectrophotometer (UV-3700, Shimadzu) is used for a transmittance measurement over the wavelength range of 400 - 1200 nm at normal incidence. The performance of a 0.28 cm^2 polycrystalline silicon solar cell with modified packaging glasses was measured with an Oriel Xenon arc lamp solar simulator (Newport) with Air Mass (AM) 1.5 filter. The filter is used to reduce spectrum mismatch between lamp and solar light of AM 1.5.

5.3 Initial optical and chemical properties

Figure 5.2 show SEM images of nanopillars and nanoholes. The dimensions such as a mean diameter and spacing of nanostructures have been determined by previous experimental studies. The height is nominally 200 nm for both nanostructures, attained by fine-tuning of the etching time. In Figure 5.3 the spectral transmittance of nanoholes and nanopillar structure arrays is evaluated by optical spectroscopy for the etched samples for 1, 2, and 3 min. The pillar nanostructures show a similar transmittance spectrum with more than 2 min of etching, while the nanohole structures require 3 min of etching to get similar transmittance.

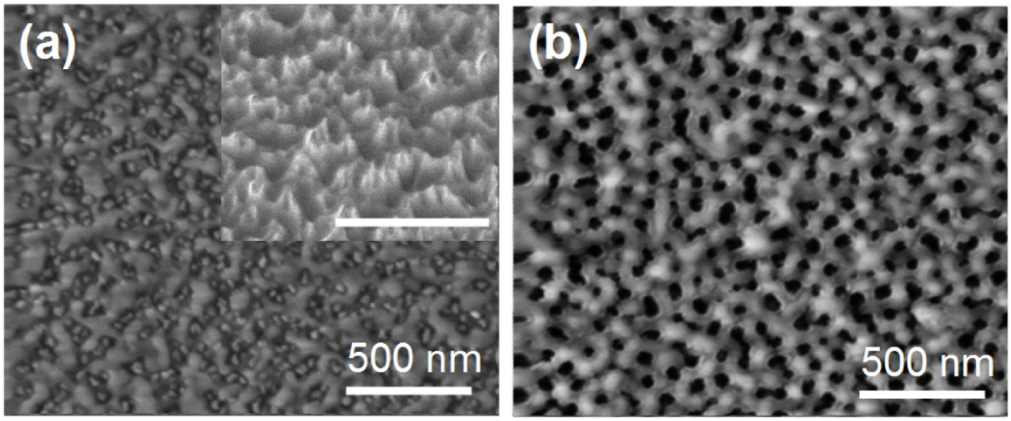

Figure 5.2 SEM images of the patterned glass surface with (a) nanopillars and (b) nanoholes. The inset of (a) is a 45° tilted image of nanopillar structures with a scale bar of 500 nm.

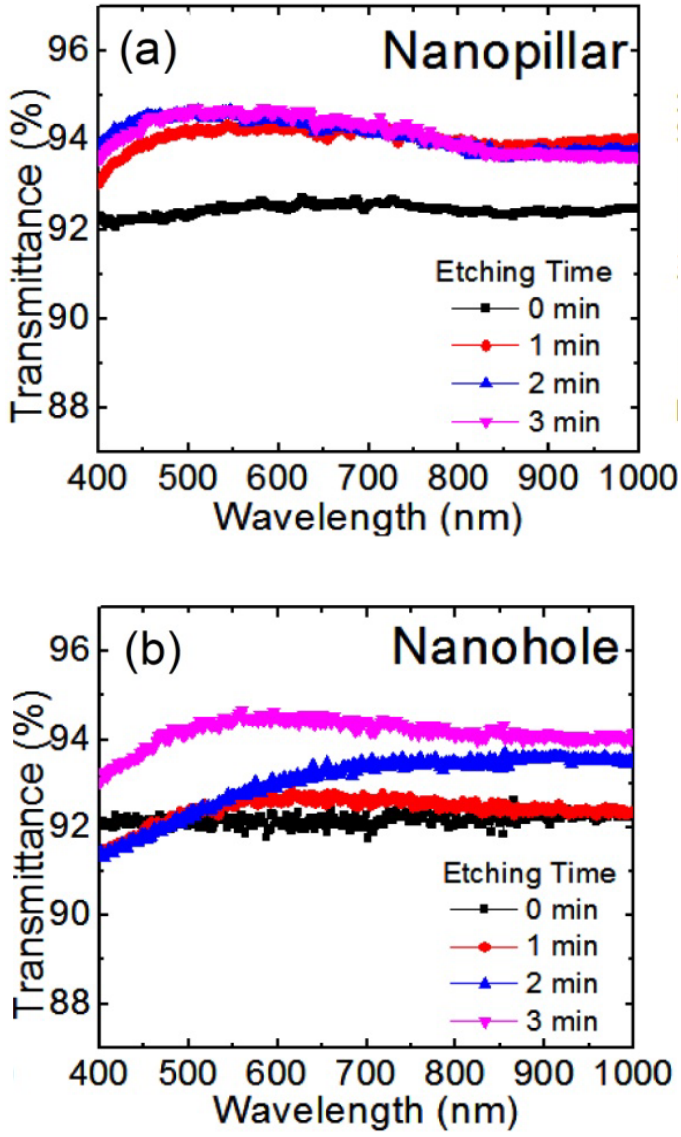

Figure 5.3 Transmittance of nanostructured samples with (a) pillar type and (b) hole type for various etching times.

The patterned samples can become either superhydrophilic or superhydrophobic by means of the coating materials regardless of their surface topography. Samples with water CAs from 3 to 170° were prepared to examine the self-cleaning effect on four distinctive surface states: hydrophilic, hydrophobic, superhydrophilic, and superhydrophobic. In Table 5.1 and Figure 5.4, the samples are classified according to the surface morphology and functionalizing materials and the CAs from the as-prepared samples are shown. Bare glasses are hydrophilic with a CA of 58°.

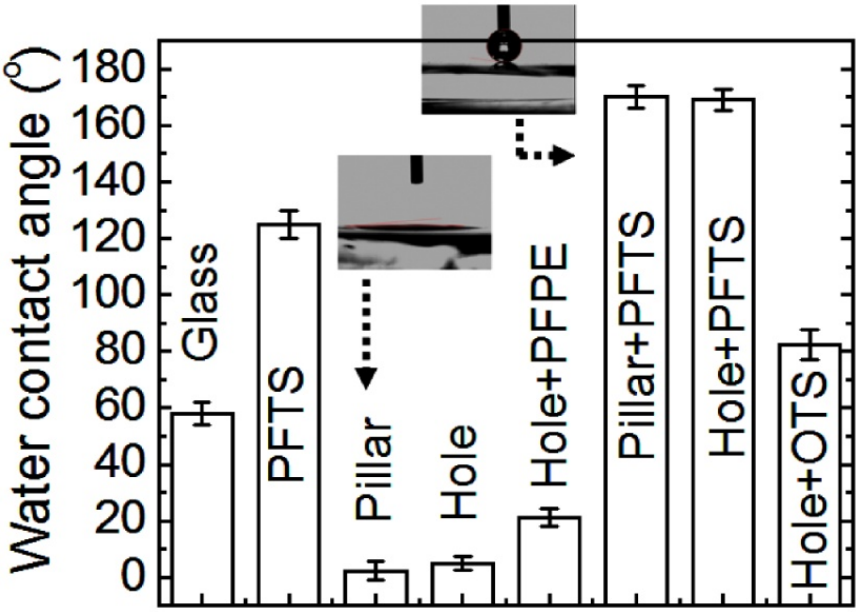

Figure 5.4 Contact angle from as-prepared samples. (Inset) static water contact angles of a superhydrophobic and a superhydrophilic surface.

Table 5.1 Classification of samples by surface properties. A water contact angle is determined by the combination of surface patterning and surface functionalization.

Surface property	Patterning	Coating	Contact angle (°)
Hydrophilic	-	-	58
Hydrophobic	-	PFTS	125
Superhydrophilic	nanopillar	-	5
Superhydrophilic	nanohole	-	2.3
Superhydrophilic	nanohole	PFPE	3.1
Superhydrophobic	nanopillar	PFTS	170
Superhydrophobic	nanohole	PFTS	167
Superhydrophobic	nanohole	OTS	82.4

The nanopatterned surface on the glass with nanoholes or nanopillars show a superhydrophilic nature with a CA less than 5°. When the PFPE coating is added on the nanohole patterned glass, the sample remains superhydrophilic due to a high surface energy of PFPE without a thermal annealing.[103] The low CAs on the nanopatterned surface without and with the PFPE coating represent a transition from the Wenzel's state to hemi-wicking state,[104] in which the increased contact area on the rough surface with a high surface energy results in spreading water through the textures and an extremely low value of CA. A critical angle (θ_c) for the hemi-wicking state is defined by

$$\cos\theta_c = (1-\phi_s)/(r-\phi_s), \qquad \text{(Eq. 5.1)}$$

where ϕ_s is the wetted fraction of solid corresponding to the islands above the film level and r is the roughness ratio of true area of the solid surface to the projected area. In case of nanohole structured surface, taking into account a diameter of ~50 nm, a spacing of ~100 nm, a depth of 400 nm, the r factor of 7.3, and ϕ_s of 0.078, θ_c is estimated to be 81°.

In contrast, a flat glass with a PFTS coating shows a hydrophobic CA of ~125° and nanopatterned glasses with PFTS coating exhibit superhydrophobicity with a CA of 167° and 170° for hole and pillar patterns, respectively.[105] Since the PFTS-coated nanohole or nanopillar patterns leave trapped air between water and the nanostructured surfaces which reduces the contact area (i.e. Cassie state), the CA becomes ~170°, which is much greater than the Young's CA of the PFTS-coated flat surface. A monolayer of PFTS coating on a textured surface can induce a transition from the Wenzel to Cassie state for both nanopillar and nanohole structures. Among the above various samples, superhydrophilic and superhydrophobic samples are expected to keep the surface clean due to spreading or rolling droplets by carrying away dust and dirt.[48]

Antireflective properties of various samples are presented in Figure 5.5. The suppression of reflection over a broad spectral range is achieved by sub-wavelength texturing at the boundary between the air and the glass forming a gradual transition of the refractive index.[52] The optical transmission of the patterned glasses is 94.0 - 94.3% while

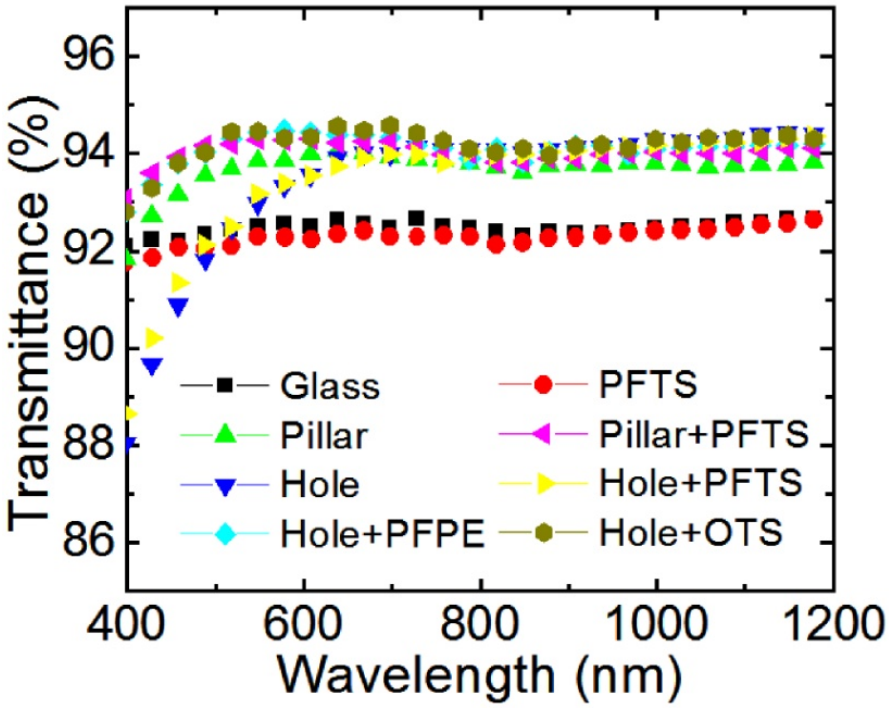

Figure 5.5 Transmission data from as-prepared samples.

that of the non-patterned glass is 92.4% in the wavelength range of 600 - 1200 nm. The nanohole or nanopillar structures on glass substrates can be considered as an effective medium which enhances the transmission by ~2% in the wavelength range above 600 nm. The effect of introducing a PFTS coating on optical transmittance is negligible. However, we observe a reduction of transmission at the short wavelength range less than 600 nm after the nanopatterning, which was attributed to wavelength dependent scattering losses in the previous report.[106]

5.4 Variation of water contact angle and transmittance by outdoor test

In order to test the outdoor durability of the different coatings and the self-cleaning effect, outdoor exposure tests have been carried out for 3 months from November 2010 to January 2011 on the roof of a 35 m tall building.[107] The samples are mounted on the roof of a building with a 23° tilting angle as shown in Figure 5.6(a) to simulate the solar module operation in Singapore (1° 18’ N) during the tested periods. The monitoring period is a rainy season in the local area with an average of 195 mm of (monthly) precipitation and the average temperature is 23 °C. In Figure 5.7, we report the variation of CAs as a function of outdoor exposure time for the various samples. The water CA of

both nanopatterned samples with PFTS coating (superhydrophobic surface) decreases below 150° during the outdoor exposure test. This implies that self-cleaning effect of the superhydrophobic surface fades away gradually, since water droplets easily stick on the surface and the dirt particles are not removed by the rolling water droplets, if the CA drops below 160°.[108]

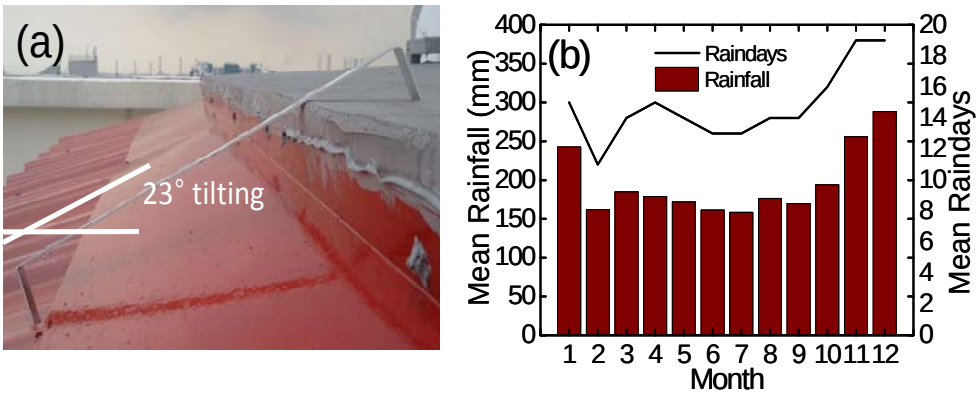

Figure 5.6 (a) Samples are mounted on aluminum bar for outdoor exposure test with a tilting angle of 23°. (b) Mean precipitation and number of rainy days in local area. The outdoor monitoring has been performed from November 2010 to January 2011.

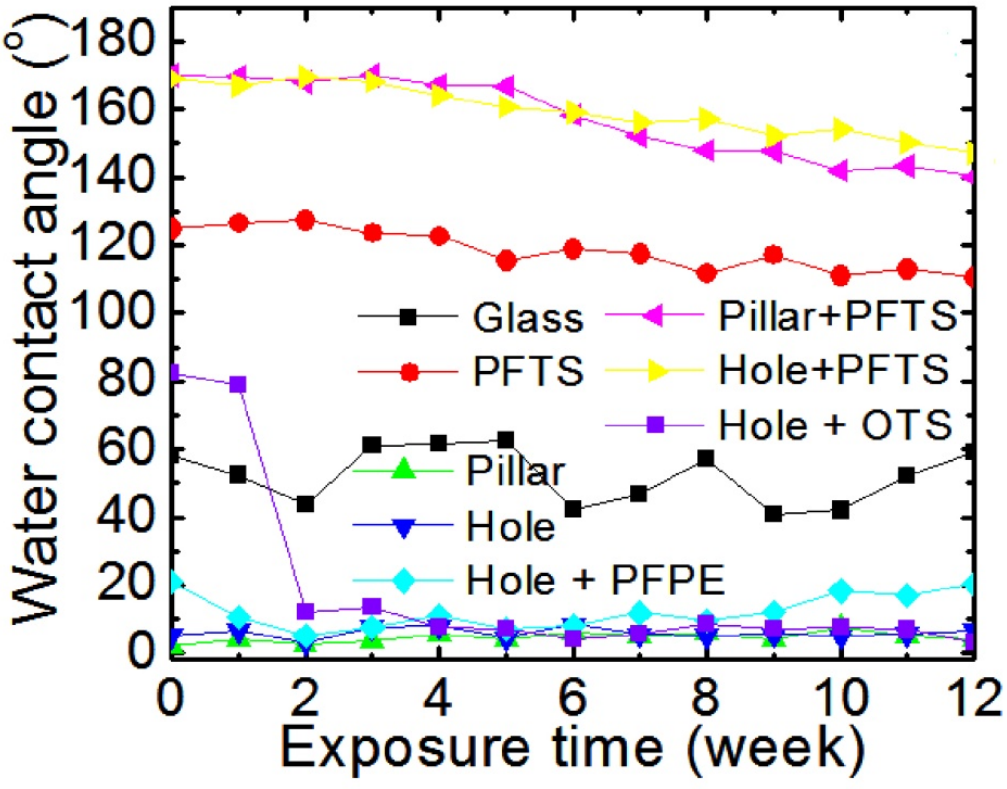

Figure 5.7 The long-term variation of water contact angle.

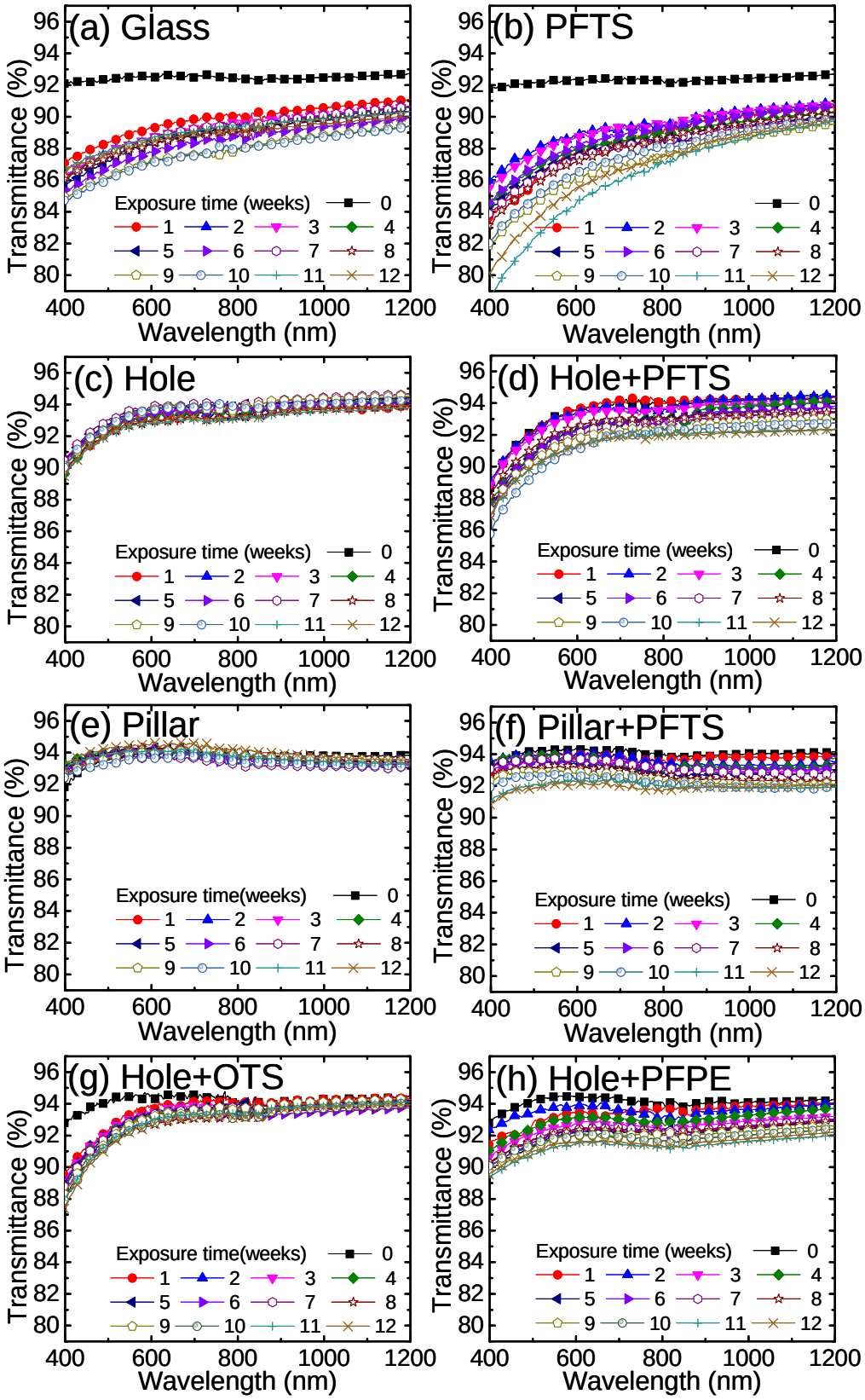

Figure 5.8 Transmittance spectra of the samples with different surface morphologies and surface coatings for 12 weeks.

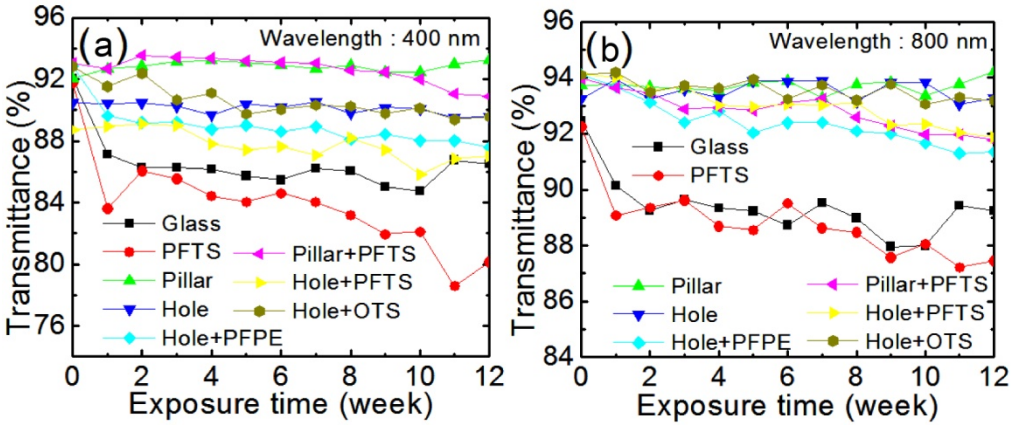

Figure 5.9 The long term variation of optical transmission monitored at (a) 400 nm and (b) 800 nm.

It is found that the CAs of the samples with PFTS coating decreases regardless of the existence of the nanostructures. According to a previous report,[109] this decrease is attributed to chemical defects of imperfect monomers that form pinholes in the coated layer. Consequently, the defects become active sites for the water adsorption at the interface between the PFTS coating and the substrate, leading to more adsorption of water. In particular, an OTS coating shows an abrupt degradation of CA resulting in the superhydrophilic state after 2 weeks, which can be attributed to unstable and weak adhesion of OTS to the substrates. On the other hand, the superhydrophilicity of the non-coated nanopatterned samples is rarely affected by the outdoor exposure, constantly maintaining a low CA around 5°. The above observation indicates that the chemical coatings may have a long term durability issue for outdoor applications.

Optical measurements are performed to test both the self-cleaning and antireflective effects over the outdoor exposure of 12 weeks as shown in Figure 5.8. Since incident light is scattered or absorbed by dust and dirt, the accumulation of those on the surface causes a reduction in the optical transmission, which reduces the efficiency of the solar cell underneath packaging glasses in solar modules.[45] In Figure 5.9, the optical transmission versus time is plotted at wavelengths of 400 nm and 800 nm, respectively, extracted from the data in Figure 5.8. The transmittance of the bare glass (hydrophilic surface) and PFTS-coated bare glass (hydrophobic surface) decreases significantly for the first 2 weeks and a gradual drop is observed

after that with a total of 4.5% transmission drop at 800 nm. The nanopatterned glasses (superhydrophobic surface) with PFTS coating also show a ~2.5% transmission drop at 800 nm. As the surface loses the superhydrophobicity, the water droplets containing dust start to stick on the surface and leave stains behind when water drops evaporate. On the other hand, the non-coated nanopatterned samples (superhydrophilic surface) show a superior self-cleaning effect, maintaining their transparency over 12 weeks regardless of the surface morphology. The transparency of the sample with superhydrophobic surfaces tends to be degraded as the CA decrease, while both transmittance and CA remain constant from the superhydrophilic samples. In the case of OTS coated sample, the transmittance drops 1-2% during the monitoring period with the CA change from 80 to ~5° in the same period.

5.5 Dust particle analysis

In order to evaluate the self-cleaning effect on superhydrophilic surfaces, SEM images of the bare glass surface and the non-coated nanohole-patterned surface after 12 weeks outdoor exposure are captured and compared as shown in Figure 5.10. Dust is collected on the bare glass surfaces, but the nanohole-patterned glass surface rarely has dust particles. Note that many small nanohole patterns in Figure 5.10(b) are visible, which are not dust particles. As seen in Figure 5.10(a) the size of dust particles on the bare glass is mainly distributed around 0.015 μm^2 (~140 nm in diameter), which falls approximately on the boundary between the Rayleigh ($\leq \lambda/10$) and Mie scattering ($\sim\lambda$) regimes, where λ denotes the wavelength of incident light.[110] As seen in Figure 5.8 and 5.9, a wavelength dependent transmission drop is observed in the bare glass after 12 weeks; 5.6% and 3.2% for 400 nm and 800 nm, respectively. Generally, the light intensity as a result of Rayleigh scattering is proportional to $1/\lambda^4$. Thus, shorter wavelengths undergo greater scattering than longer wavelengths on the bare glass due to small sized dust particles, resulting in higher transmittance drop at short wavelengths.[106] On the other hand, dust particles of much larger size ($\geq \lambda$) are collected on both the bare glass and the nanohole-patterned glass, which may cause Mie scattering. However, the effect on the transmittance is negligible since the

intensity of Mie scattered radiation is dominant not in the backward direction but in the forward direction.[16] Thus, the transmittance on the nanohole-patterned glass is rarely affected in spite of the observation of larger particles on the surface.

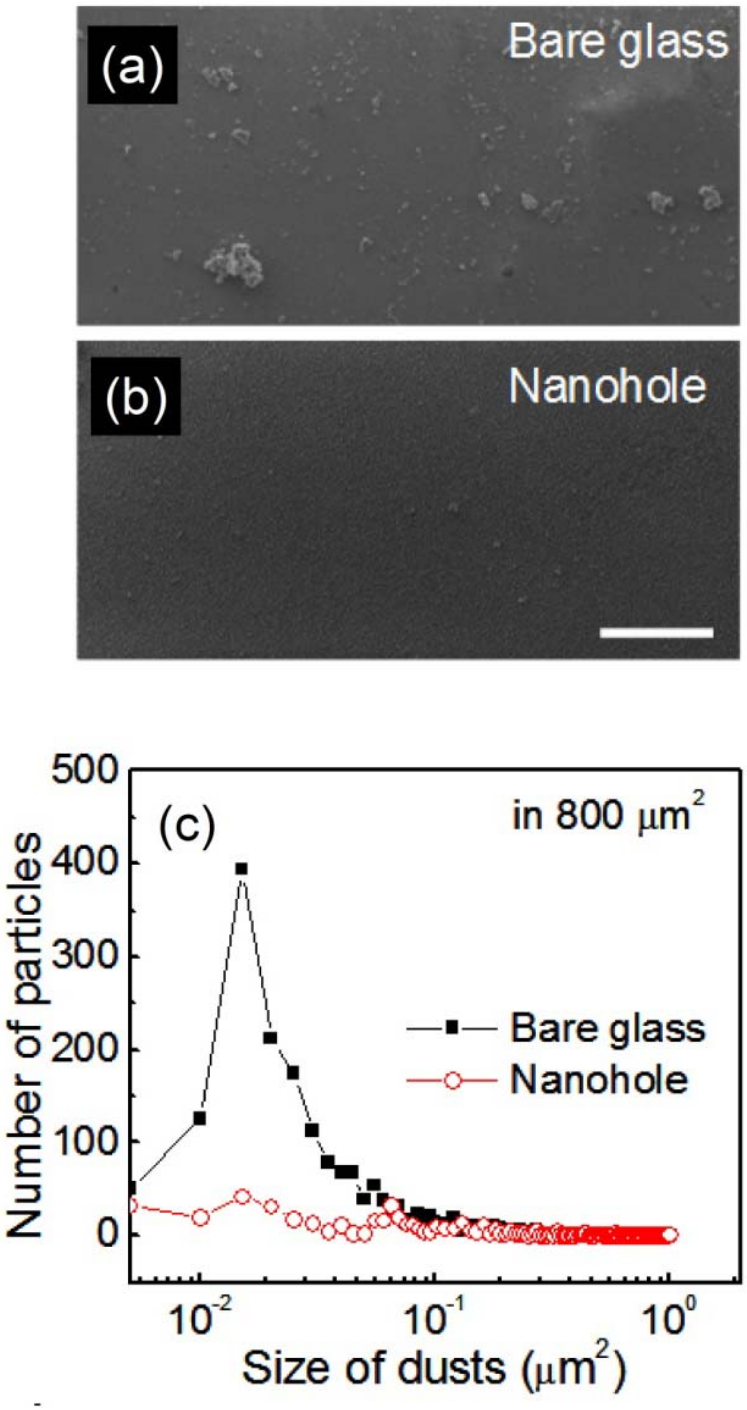

Figure 5.10 SEM images of (a) the bare glass surface and (b) the nanohole surface after 12 weeks outdoor test. (Scale bar: 20 μm) (c) The total number of the particles on the bare glass and nanohole glass remaining on the 800 μm^2 after 12 weeks outdoor test.

5.6 Variation of photovoltaic parameters by outdoor test

To evaluate the applicability of our self-cleaning glasses on solar modules, glass samples were tested when acting as packaging for a monocrystalline silicon solar cell that has an efficiency of 11.5% (before packaging glass is added). The solar cell parameters are normalized to avoid the effect of intrinsic performance changes of the solar cell during the monitoring period. It is found that the efficiency and the short circuit current of the solar cell are closely related to the reduction in the optical transmission, while the fill factor and the open circuit voltage are less influenced. In Figure 5.11, the drops of efficiency and short circuit current are correlated with the transmission, in which each number represents the measurement week. The bare glass and the PFTS-coated flat glass show a prominent decrease in the efficiency, the short circuit current, and transmission over time, whereas the PFTS-coated nanopatterned samples with a superhydrophobic property have a less abrupt but still-present degradation of the parameters. For example, bare glass and superhydrophobic (nanopatterned glass with PFTS) packaging shows 7.79% and 2.62% of efficiency drop, respectively, after 12 weeks. However, as expected from the CA and transmittance studies, the solar cells, with superhydrophilic glass packaging of non-coated nanopatterned surfaces, exhibit a relatively constant performance (1.39% drop of efficiency) during the monitoring period, as indicated by the fact that data points in Figure 5.11 are less scattered. One notable point is that the PFPE-coated nanohole-patterned sample shows larger variations of the short circuit current and the efficiency with more transmission drop than the other non-coated nanopatterned samples in spite of their common superhydrophilic property. It seems that the PFPE coating itself becomes a collection of capturing sites for more dust on the surface during outdoor testing over time, which again emphasizes that chemical functionalization is not necessary in order to achieve both self-cleaning and an antireflective glass surface.

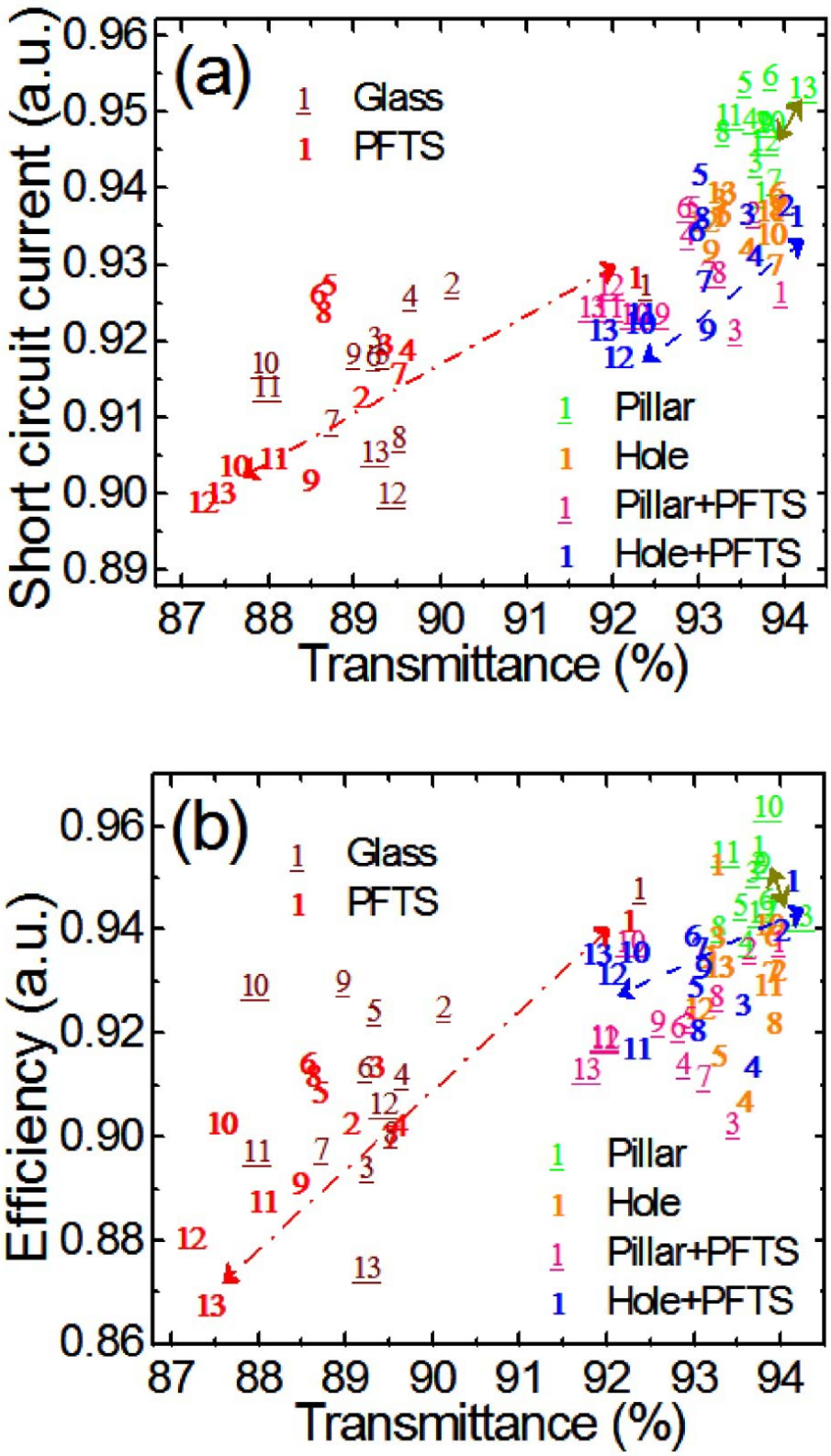

Figure 5.11 Transition of (a) the short circuit current and (b) the efficiency of a solar cell correlated with averaged transmittance, which is averaged from 400 to 1200 nm. The number '1' in the figures means the measured data as-prepared and '13' means the data after 12 weeks for each set of sample.

5.7 Conclusion

We have compared various nanostructure-based self-cleaning and antireflective glasses with and without chemical functionalization. A long term outdoor test suggests that the both effects are pronounced in the case of superhydrophilic surfaces compared to hydrophobic, hydrophilic, or superhydrophobic surfaces. In particular, a superhydrophilic glass that shows a superior performance is achieved by directly patterning a glass surface without any further surface chemical treatment. Our successful demonstration of a self-cleaning and antireflective glass surface may find potential applications in various outdoor optoelectronic devices such as packing glasses of solar modules without involving any additional chemical treatment process.

Chapter 6: Large-scale Nanotexturing of Glasses

6.1 Introduction

Since most of the reflection loss takes place at the air/glass and glass/silicon interface in a commercial Si photovoltaic device, an antireflective layer at those interfaces is expected to reduce the light loss and improve the energy conversion efficiency of solar cells. Antireflective coatings on glass are highly desirable, since glasses are widely used as a packaging material in the solar industry due to their transparency and durability. For example, an 8% reflection loss across a sheet of glass can be reduced with the aid of antireflective structures. However, the formation of an antireflective layer on a typical solar glass panel is challenging because of the large size of the glass panel, which is usually bigger than a few hundred millimeters.

Recently, the anodizing method has risen in popularity as an alternative to nano-lithography with the advantage of the dimensional controllability of dense nanoholes.[34, 111-114] The recent achievement of a two-step anodizing technique has demonstrated the formation of periodic arrays of nano-channels.[115] In addition, the direct formation of anodic aluminum oxide (AAO) on top of a substrate leads to a simpler fabrication process by eliminating the tedious AAO film transfer process.[33, 116] The directly formed AAO membrane has been utilized as a mask for the etching or deposition on conducting substrates, however the anodization of an aluminum film on a large area dielectric substrate is still challenging due to the insulating nature of the substrate.[117] Therefore, the anodizing method has not been a preferred choice for large area fabrication on a dielectric substrate compared to other nano-lithographic methods.

However, we propose a robust fabrication technique for an antireflective coating on a large area glass substrate by modifying the anodizing method. The modified fabrication method using grid line contacts facilitate anodization of a 6×6 inch^2 area aluminum film on a dielectric substrate. The antireflective effect from nanostructures has been evaluated by measuring the optical transmission and the photovoltaic performance in indoor and outdoor environments for more than 3 months.

6.2 Experimental details

6.2.1 Preliminary studies for a modified anodizing method

Two types of preliminary samples were prepared to compare the effect of contact types on thin film anodization. A borosilicate glass substrate (BOROFLOAT 33, SCHOTT) was masked with a thermal tape along the edge of the glass in order to define the size of the aluminum film. 250 nm of aluminum was deposited by electron beam evaporation (Auto 306, Edwards). An aluminum film with 3×3 cm^2 area was prepared with a point-type anode contact. 1×3 cm^2, 2×3 cm^2, and 3×3 cm^2 of aluminum films were prepared for a line-type anode contact. A copper tape and a conductive silver paste were used to connect the aluminum films with a voltage source. The copper tape and silver paste were electrically isolated from electrolyte by sealing them with nail polish. Nail polish was also injected on the aluminum film by an injector along one shorter edge of the aluminum film, serving as a line-type anode during the subsequent anodization process. The anodization was performed in 0.3 M oxalic acid under 40 V of constant voltage. Subsequently, the anodic membranes were soaked in 5 wt% aqueous phosphoric acid for 90 min to widen the nanoholes and open the pore bottoms.

6.2.2 Fabrication of large scale antireflective glasses

In Figure 6.1, fabrication procedures of a large area antireflective glass are presented. 6×6 inch^2 borosilicate glasses were cleaned with deionized (DI) water to remove dust and particles on the glasses. A 250 nm thick aluminum film was deposited on the cleaned glasses. Before the anodizing process, cross-checked grid lines with 1 inch gap were applied on an aluminum film using nail polish to protect the underlying aluminum lines from oxidization. As seen in Figure 6.1(b), the aluminum film becomes transparent from the edge to center, and the whole area becomes transparent with a sudden drop of the anodizing current. After forming an AAO membrane under the same anodizing and pore widening conditions as mentioned above, subsequently, ICP-RIE etching (SLR-770, Plasma-Therm) was conducted using the AAO layer as an etch mask. The plasma etching (5 mTorr, 100 Watt RIE, 500 Watt

ICP, CF_4 20 SCCM, Ar 5 SCCM, 4 min) transferred the array of nanoholes onto the glass surface. Finally, the remained AAO and aluminum lines were removed by soaking into 5 wt% phosphoric acid. The nail polish grid lines were simultaneously peeled off during the removal of underlying aluminum lines.

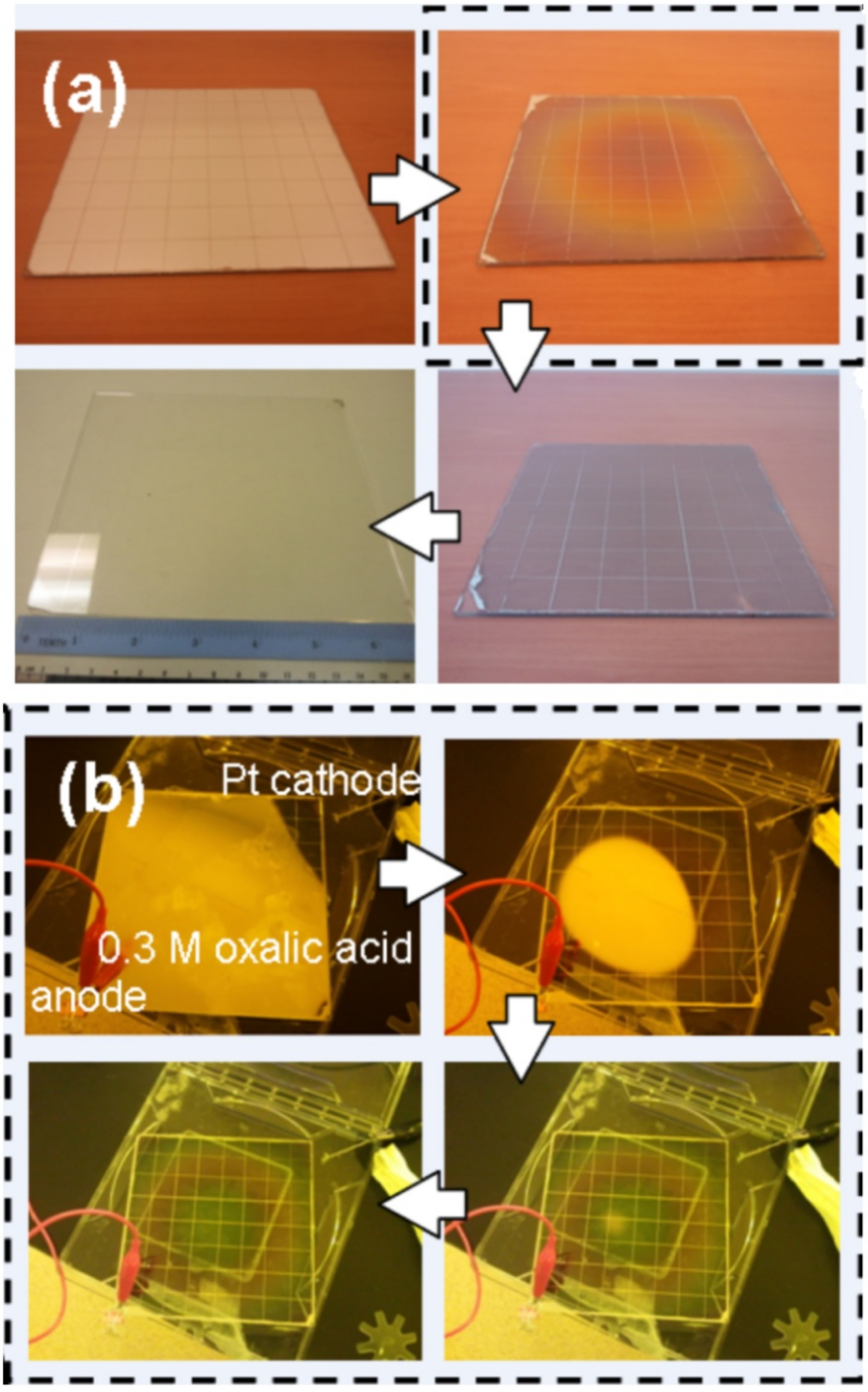

Figure 6.1 (a) Nanopatterning procedures by the modified anodizing method on a 6 inch glass substrate. (b) Anodization process of an aluminum film with the grid lines.

6.2.3 Solar cell packaging

5×5 inch^2 crystalline Si solar cells were cut into two pieces and the I_{sc} was measured by a transducer (CASR 6-NP, LEM). An experimental setup has been developed to study the effect of antireflective structures on a silicon solar cell. The schematic diagram of packaging is shown in Figure 6.2(a). Because the short circuit current (I_{sc}) is too high to be detected accurately by the current transducer, we cut the cell into half to reduce the short circuit current before packaging. The open circuit voltage becomes double due to the connection of two cells in series. It should be taken into account that the original conversion efficiency and total power remain same as the one of the original 5×5 inch^2 solar cell after cutting. The solar cell was laminated between a polymer back sheet and a front antireflective/planar glasses using Ethylene vinyl acetate (EVA), an index matching adhesive encapsulant that minimizes reflection and protects solar cells from humidity and dust simultaneously. A set of solar cells packaged with planar glass was prepared as a control sample to monitor relative enhancement because weather conditions can affect the absolute value of V_{oc} and I_{sc}. The outdoor experiments were conducted from Mar 2012 to June 2012.

6.2.4 Indoor and outdoor characterization

We measured the spectral transmission of textured glasses using a spectrophotometer (UV-3700, Shimadzu) in the wavelength range 400 - 1000 nm. The surface morphology was investigated by using a SEM (NanoSEM 230, FEI). The photovoltaic performance of the packaged cells was evaluated using a Newport class-A solar simulator under AM 1.5 illumination. The outdoor solar cell characterization was performed on the roof of a ~30 m tall building at the National University of Singapore for 4 months. Packaged solar cells were facing in a southerly direction and mounted with a tilt angle of 20°. A transducer was connected to both electrodes of a packaged solar cell, therefore I_{sc} flowing through the transducer was converted to a voltage. V_{oc} was directly measured from two electrodes of a packaged solar cell. The values of converted I_{sc} and V_{oc} were stored by a data acquisition tool (NI USB-6009, National Instrument) every 1 second.

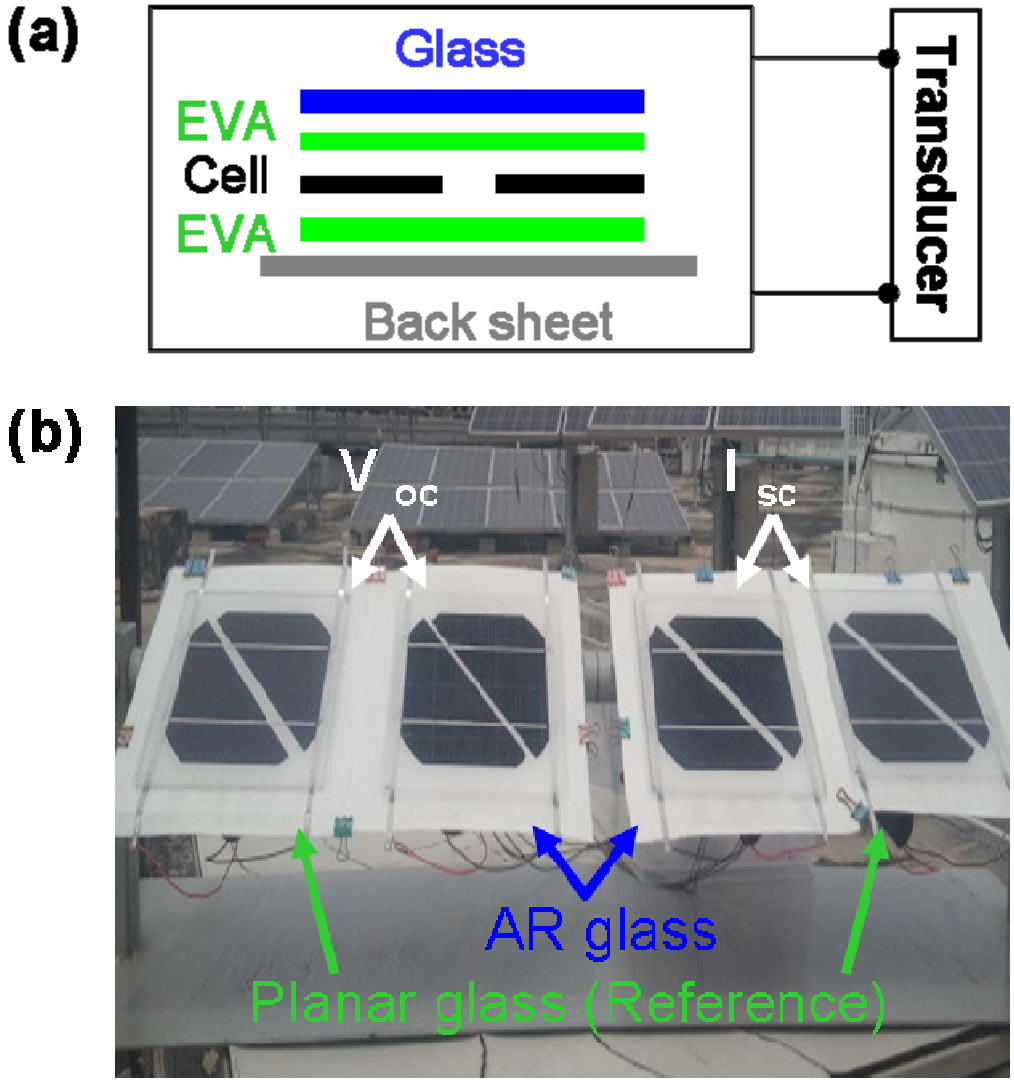

Figure 6.2 (a) Schematics of solar cell packaging with a front glass sheet and a back polymer sheet using EVA as an adhesive. (b) Experimental setup of packaged solar cells mounted on a rooftop with a tilting angle of 20°.

6.3 Results and discussion

A random array of nanoporous structures formed by anodizing an aluminum thin film provides an effective template for sub-wavelength structures on a glass surface in which a thin aluminum film on the small substrate of 1 × 1 cm^2 was completely anodized. With a large area aluminum film on an insulating substrate, however, an electric discontinuity can occur during the anodizing process and the formation of AAO can be localized near the anode contact point. In order to solve this problem, we investigate various contact designs as follows.

6.3.1 Effects of contact type on anodization of a thin aluminum film

Figure 6.3 shows two types of AAO samples to examine the effect of the contact schemes. Anodization of a 250 nm thick aluminum film was carried out with a point contact (~3 mm in diameter) and a line contact (~0.5 mm width and 1 cm long) as shown in Figure 6.3(a-d). Three different sizes of aluminum films in Figure 6.3(b-d) were prepared to determine how large an area can be fully anodized by the line contact. After the anodizing step, as can be seen in Figure 6.3(a), color gradation is observed on the 3 × 3 cm^2 point contact sample. This results from

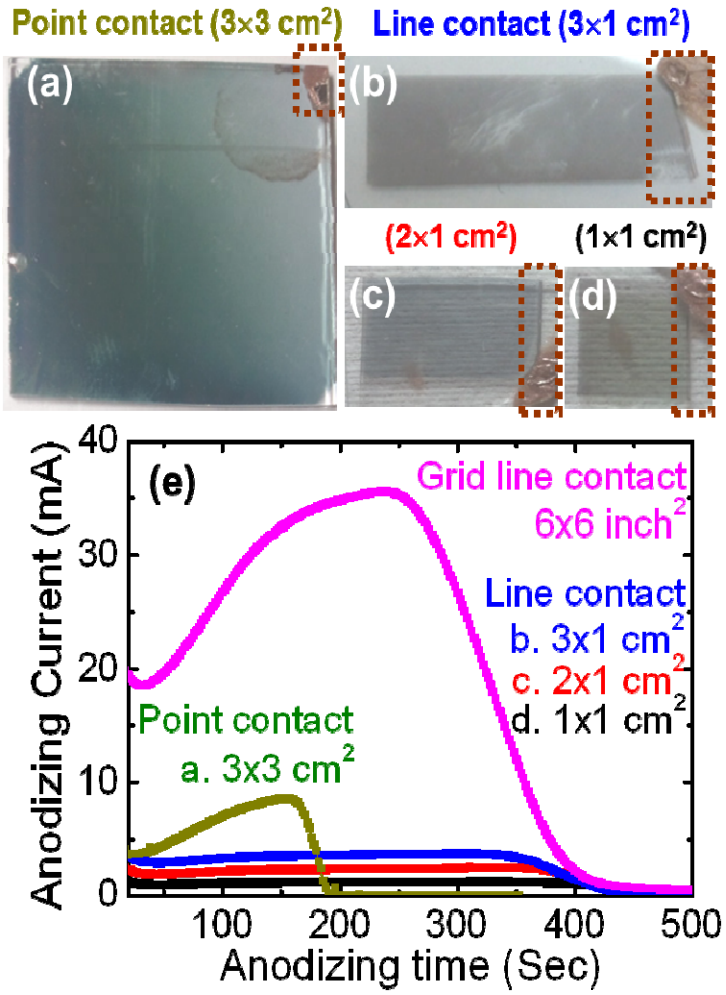

Figure 6.3 Anodized AAO thin films. (a) Point-type anode contact. (b-d) Line-type anode contact. The dotted boxes in (a-d) indicate the anode contact on each sample. (e) Anodizing current versus time curves.

the localized anodization near the electrode contact. As seen in Figure 6.4(a-c), the AAO layer formed with the line contact has a uniform distribution of nanopores near the line as well as 3 cm away from the line. However, the AAO layer formed by the point-type contact has a color variation along the surface as shown in Figure 6.4(d). The darker area away from the contact has defective holes, while the area close to the point contact is transparent. It is seen from a 45° tilted view in Figure 6.4(e) and (f) that the formation of nanoholes is defective away from the electrode, while more uniformly formed nanoholes were observed near the contact. Another piece of evidence of incomplete anodization can be found from the anodizing current curves in Figure 6.3(e). The pore formation continues until all the aluminum film is consumed and the end-point of the process is judged by a sudden drop of the anodizing current to zero. However, the anodizing current of the point contact sample in Figure 6.3(e) exhibits an early drop that is caused by electric discontinuity of the oxidized aluminum film near the point contact. Therefore, the point contact cannot be used as an anode contact for a large area aluminum film on an insulting substrate.

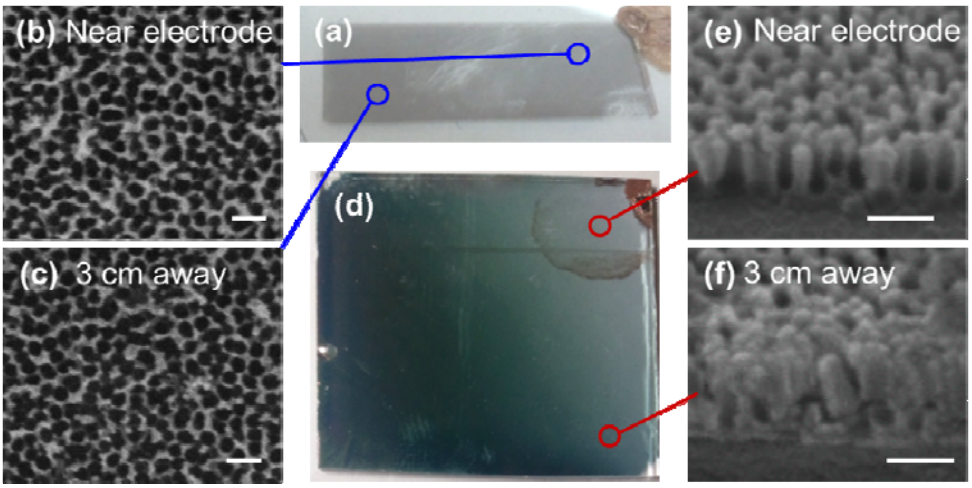

Figure 6.4 Comparison of the nanohole distribution across the AAO films which were fabricated by (a-c) a line contact, and (d-f) a point contact. Scale bar: 200 nm.

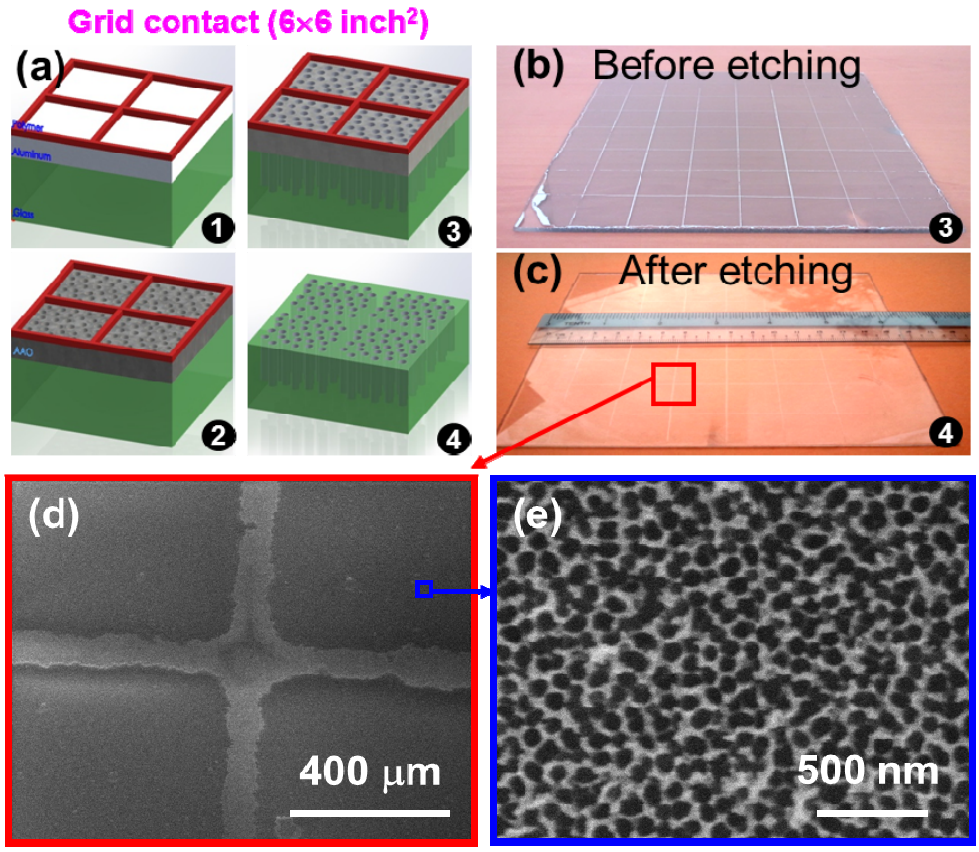

Figure 6.5 (a) Schematic diagram of the fabrication procedure for a large area antireflective glass using modified anodizing methods. (b) Photographs of the anodized aluminum thin film before etching. (c) Photographs of the textured glass after etching. (d, e) SEM images of the untextured line and the textured area, respectively.

6.3.2 Antireflective texturing using grid contacts in anodizing process

Based on the above result we choose 1 inch gaps between anode contact lines and cover a 6 × 6 inch^2 aluminum film with the cross-checked mesh polymer lines. The schematic of the modified fabrication process is illustrated in Figure 6.5(a) and the corresponding photographs are shown in Figure 6.1. As shown in Figure 6.3(e), the anodizing current of a 6 × 6 inch^2 sample drops at a similar time as observed from other samples, which indicates that the same thick aluminum film on the large glass substrate is consumed completely with the aid of the grid lines. It is important that the underlying aluminum grid lines (covered by nail polish) remain intact and conductive during the anodization process, leading to uniform anodization. Subsequently, plasma etching of the glass substrate is performed using the AAO membrane as an etching mask. Figure 6.5(b) and (c) demonstrate the

photograph of glasses before and after the etching process, respectively. Due to more reflection of light without nanostructures, unpatterned areas are seen as lines after the etching process, as shown in Figure 6.5(c). As shown in Figure 6.5(d), the glass surface under the lines remains untextured after the plasma etching. On the other hand, Figure 6.5(e) shows the morphology of other areas where the nanoholes in the AAO membrane mask are transferred onto the glass substrate. The randomly distributed nanoholes, in agreement with previous studies, have a diameter of ~80 nm and a depth of 400 nm after etching.[118]

6.3.3 Enhancement in optical performance

The optical properties of the large area (6×6 inch^2) textured glasses are evaluated by measuring transmission at a spectral range between 400 and 1000 nm. The transmission spectra of five different locations on a textured glass are shown in Figure 6.6(a). The patterned glass has an antireflective property with 2 - 3% higher transmittance than that of a non-patterned glass in the wavelength range from 550 to 1000 nm regardless of the measurement location. The drop of the transmittance at short wavelengths is attributed to wavelength dependent scattering losses.[106] The random array of nanostructures in our samples as shown in Figure 6.5(e) has an advantage for photovoltaic applications, since the irregular and dense nanohole array can give rise to a broadband transmission spectrum preferable for the solar cell applications.[39] The five transmission spectra obtained from a large antireflective glass sample are averaged and each averaged spectrum of the five different samples is shown in Figure 6.6(b). It is seen that all the fabricated antireflective glasses show 2 - 3% higher averaged transmittance than the planar one in the wavelength range above 550 nm. The untextured portion of glass (Figure 6.5(d)) may reduce the total transmission by reflection or scattering; however, no difference is observed, when the beam is focused only in the patterned area or around the grid lines.

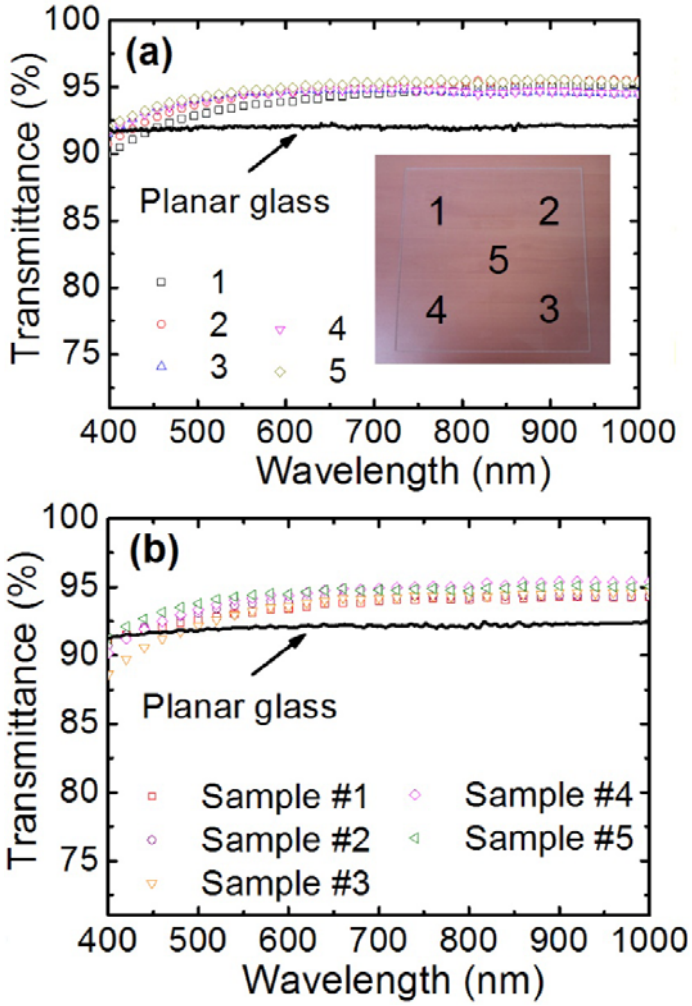

Figure 6.6 Optical transmittance of antireflective and planar glasses. (a) Transmittance spectra at 5 different locations on an antireflective glass. (b) Transmittance spectra of 5 different antireflective glasses.

6.3.4 Enhancement in photovoltaic performance

The antireflective glass and the planar glass are packaged together with a 5 × 5 inch^2 c-Si solar cell as described in Figure 6.2(a). The current-voltage curves of the packaged solar cells are measured by a solar simulator and the result is shown in Figure 6.7. The major improvement is observed for the short circuit current (I_{sc}) increasing from 1.956 A (with planar glass) to 2.178 A (with antireflective glass) due to the enhanced optical transmission of the front glass. While there is 11.34% improvement in I_{sc}, the variation in the open circuit voltage (V_{oc}) and fill factor is small. Due to the increased I_{sc}, the power conversion efficiency (η_{eff}) increases from 7.9% to 8.57%. Note that the reflection from the white back sheet can contribute to the enhancement of I_{sc} since the reflected light can be guided in the front glass. In particular, the

textured glass can be expected to behave like optical fiber due to the graded refractive index of the textured layer, which can guide the reflected light and increase the I_{sc} more than the planar glass.

For further verification of the antireflective effect of the nanopatterned glass under various outdoor environmental factors such as ultra violet light, dust, weather, and humidity, we have monitored the performance of the packaged solar cells outdoors over a period of time. The measurement setup and configuration is shown in Figure 6.2(b). Figure 6.8(a) depicts that the I_{sc} as a function of light incident angle into the solar panel characterized by a solar simulator. The omnidirectional property is observed by comparing the output from antireflective glass packaged cell and planar glass package cell. For all angles 0 - 60°, the device with antireflective glass shows ~13% higher short circuit currents. Figure 6.8(b) shows a difference of I_{sc} between the antireflective glass solar cell and the planar glass solar cell as a function of time over a day. Here the daily trends over 40 days are averaged. As the sun rises, the absolute difference becomes larger and reaches a peak around noon due to the varying intensity and incident angle of light. However, the relative enhancement ratio of I_{sc} is constant during a day regardless of the altitude of the sun. Interestingly, this indicates the omnidirectional antireflective property of the nanostructured surface.[18, 119]

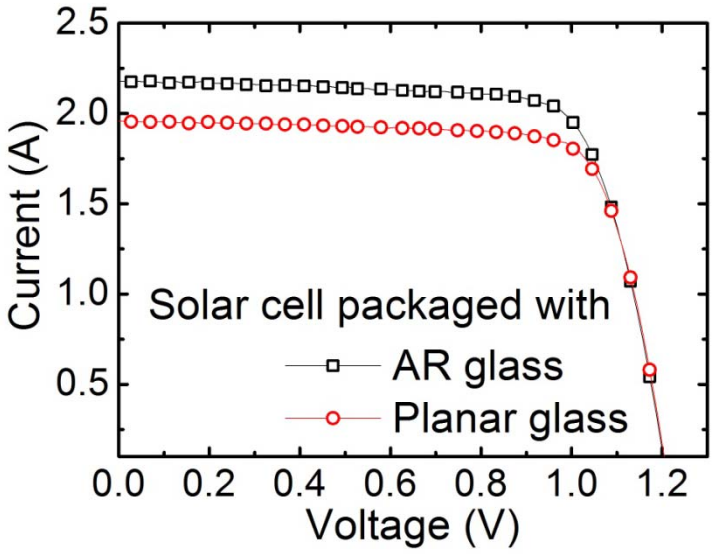

Figure 6.7 Indoor characterization data of solar cells packaged with an antireflective glass or a planar glass. *IV* curves of the solar cells with a patterned or planar front glass sheet, measured by a solar simulator.

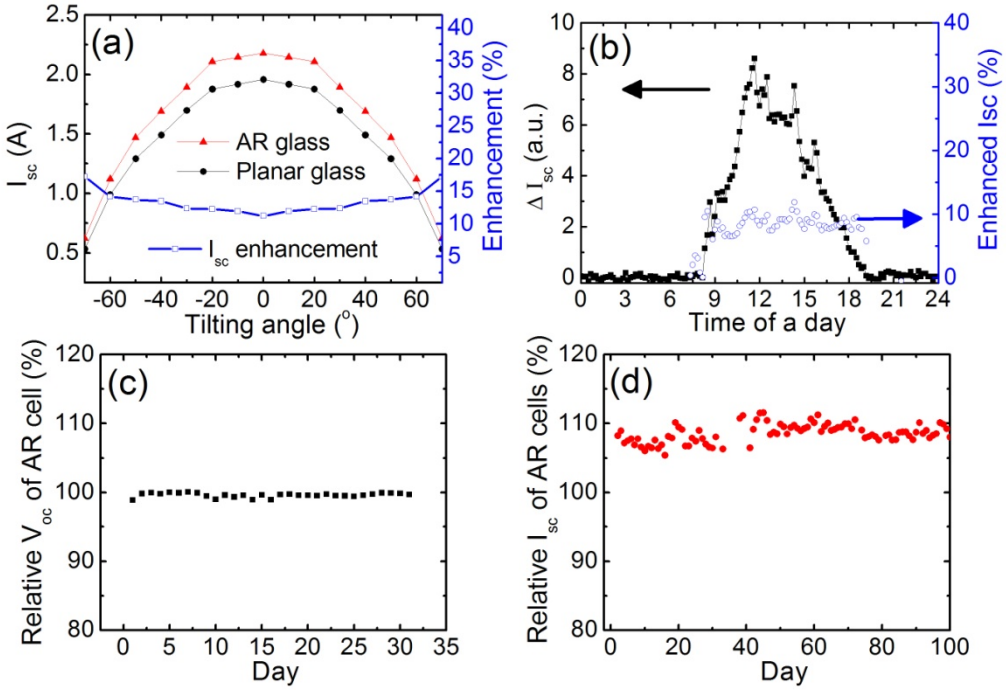

Figure 6.8 Outdoor characterization data of solar cells packaged with an antireflective glass or a planar glass. (a) Variation of short circuit current and its enhancement as a function of tilting angle of solar cells packaged with planar glass and antireflective glass. (b) Enhanced I_{sc} by the antireflective texturing and its enhancement factor over a day. (c, d) Long term variation of V_{oc} and I_{sc} of the antireflective glass cell, respectively, normalized with respect to the V_{oc} and I_{sc} of the planar glass cell.

Long term trends of V_{oc} and I_{sc} are shown in Figure 6.8(c) and (d), respectively. The values collected for a day are added to represent I_{sc} or V_{oc} of each day. The I_{sc} and V_{oc} of an antireflective glass solar cell are normalized by the I_{sc} and V_{oc} obtained from a planar glass solar cell, respectively. The normalized V_{oc} of the antireflective glass solar cell is almost the same as that of the planar glass solar cell during the monitoring periods. On the other hand, the antireflective glass cell shows ~9.03 ± 0.015% higher I_{sc} than the planar glass cell as shown in Figure 6.8(d). In addition, the antireflective property of the nanostructures persists in the outdoor measurement for more than 3 months without any cleaning of the glass due to the self-cleaning effect of the nanostructured glass.

6.4 Conclusion

We have demonstrated a modified anodizing method to fabricate an antireflective surface on a large area glass. The difficulty of thin film anodization on an insulating substrate is overcome by introducing grid line contacts, leading to complete anodization of 6×6 inch^2 aluminum films on glass substrates. The transferred nanoholes on the glass substrate exhibit broadband and omnidirectional antireflective properties, leading to an 11.34% improvement in the I_{sc} of a 5 inch solar cell and enhanced power conversion efficiency from 7.9% to 8.57%. Moreover, the enhanced optical properties persist for three months in an outdoor environment. The proposed anodizing method can be considered as an alternative technique for the fabrication of large area nanostructures, which can find applications in the photovoltaic industry.

Chapter 7: Conclusion and Future Researches

7.1 Summary

This thesis develops a new fabrication method and hybrid functionalities of a nanostructured glass to achieve higher performance of photovoltaic devices. It is found that nanostructures on a glass substrate induce an optically enhanced transmission and chemically high surface energy by the elevated surface roughness. The surface modification results in the antireflection and self-cleaning property, and thus increasing the photovoltaic performance of solar cells with the smart coating in outdoor environments.

First, we have confirmed that, by FDTD simulation studies, nanostructures show broadband and omnidirectional antireflective properties in spite of the homogeneous effective index profile of the cylindrical subwavelength structures. With the cone shape of nanostructures which has a gradual change of effective refractive index, we figured out its excellent antireflective properties.

Subsequently, based on the simulation works, antireflective coatings on glass substrates are fabricated by using anodizing followed by plasma etching. The hole-type nanostructures on the transparent glass enhance the transparency of the glass. The tapered nanoholes of sub-100 nm diameters lead to an increase in transmission due to a continuous variation of the filling fraction across the patterned layer. Improvement of optical transmittance in wide spectral and wide angular ranges is achieved, which can be directly applied to solar cell packaging for efficient light harvesting.

For further studies regarding the self-cleaning effect of the nanostructured surface, we have compared various nanostructured glasses with and without chemical functionalization. A long term outdoor test suggests that self-effects are practically more pronounced on the superhydrophilic surfaces than the other hydrophobic, hydrophilic, or superhydrophobic surfaces. The superhydrophilic surface is obtained by directly patterning of a glass surface without any further surface chemical treatment. It exhibits the self-cleaning effects for long term in outdoor environment. Our successful demonstration of

the self-cleaning and antireflective surface may find potential applications in various outdoor devices such as packing glasses of solar modules.

Lastly, we have demonstrated a modified anodizing method to fabricate an antireflective surface on a large area glass. The difficulty of thin film anodization on insulating substrates is overcome by introducing the grid line contacts, leading to a complete anodization of the 6×6 inch^2 aluminum film on a glass substrate. The transferred nanoholes onto the glass substrate provide the broadband and omnidirectional antireflective properties with self-cleaning property. The textured glass is packaged with a solar cell. The antireflection improves the short circuit current by ~11.34% compared to the planar glass cell, and increases the power conversion efficiency. Moreover, the enhanced optical properties continue under outdoor environments. The proposed anodizing method can be expected as an alternative nanolithography for scaling-up of the nanotexturing.

We have provided that the smart surface can work with real devices in real outdoor environments for long duration. The research activities presented in this thesis are limited to transparent glasses and its application for solar cell packaging. However, our results are applicable for every interface which needs low reflection. The technique for large area fabrication can be considered as a reliable candidate for mass production after fine tuning of the nanotexturing processes. Reducing the fabrication cost furthermore and compatibility with an existing the semiconductor fabrication process is the critical aspects for future works.

7.2 Suggestions for future works

This thesis focuses on developing a durable multifunctional surface coating as one of the technical solutions for photovoltaic devices to enhance the energy conversion efficiency. The present studies show that a nanotextured surface and surface functionalization with chemicals are promising methods for the multifunctional coating. However, these approaches suffer from issues such as durability and high cost for fabrication. In addition, the scaling-up for large area coatings is still not fully demonstrated and further examination should be carried out in order to apply the techniques in various conditions.

Some of the suggestions for future researches in the field of the advanced surface coating are highlighted below.

(1) To further improve the solar cell efficiency by reducing optical loss, integrating the antireflective layer into the solar cell is important for efficient photon manipulations. Not only the glass surface, but also the interface between glass/(transparent top electrode)/p-i-n active layers is one of the major reflective sources. While the double side nanotexturing can be easily applied on the packaging glass, giving rise to ~100% optical transmission through the glass, the nanotexturing in glass/(transparent top electrode)/active layer interfaces is not simple, since it may cause the degradation of electrical mobility in the top electrode or active region,[120] which can compensate the enhancement of optical transmission. The use of the antireflective layer should be followed by the careful study on how the nanotexturing influences on solar cell characteristics.

(2) The self-cleaning effect of a lotus leaf is based on the water washing mechanism. However, many of solar cells installed in a desert or in a dry region hardly benefit from the *wet* self-cleaning effect. In a dry area, wind can be an agent to carry the dust deposited on the solar modules. Anti-adhesive and anti-friction surfaces can play a role to achieve the *dry* self-cleaning. For example, polytetrafluoroethylene (PTFE, Teflon) is one of the materials used as a non-stick coating for pans and other cookwares preventing from a physical damage and sticking of dirt. Low adhesion force of Teflon can make it a good candidate for the dry self-cleaning purpose. However, blocking the light by the additional opaque layer should be resolved for solar cell applications.

(3) Last two decades, it is observed that solar cell prices fall 20% for every doubling of industry capacity. High-efficiency and innovation in fabrication process is of interest to decrease the cost of solar energy. Researchers should balance the cost of fabrication and the functionality of the materials. Most of present methods used to produce nanostructured surfaces are not compatible with large-scale fabrication which requires fast and low-cost processing. Thus, low-cost materials with a single-step fabrication process will be appreciated in the smart coating technology.

REFERENCES

[1] E.L. Wolf, Introduction, Nanophysics and Nanotechnology, Wiley-VCH Verlag GmbH, 2008, pp. 1.

[2] L. Ge, S. Sethi, L. Ci, P.M. Ajayan, A. Dhinojwala, Carbon nanotube-based synthetic gecko tapes, Proceedings of the National Academy of Sciences of the United States of America, **104** (2007) 10792.

[3] X.J. Feng, L. Jiang, Design and creation of superwetting/ antiwetting surfaces, Advanced Materials, **18** (2006) 3063.

[4] W. Barthlott, C. Neinhuis, Purity of the sacred lotus, or escape from contamination in biological surfaces, Planta, **202** (1997) 1.

[5] X. Yao, Y.L. Song, L. Jiang, Applications of Bio-Inspired Special Wettable Surfaces, Advanced Materials, **23** (2011) 719.

[6] X.J. Feng, L. Jiang, Design and creation of superwetting/antiwetting surfaces, Advanced Materials, **18** (2006) 3063.

[7] D.G. Stavenga, S. Foletti, G. Palasantzas, K. Arikawa, Light on the moth-eye corneal nipple array of butterflies, Proceedings of the Royal Society B-Biological Sciences, **273** (2006) 661.

[8] P. Vukusic, Natural photonics, Physics World, **17** (2004) 35.

[9] T.D. Happ, M. Kamp, A. Forchel, J.L. Gentner, L. Goldstein, Two-dimensional photonic crystal coupled-defect laser diode, Applied Physics Letters, **82** (2003) 4.

[10] C. Manolatou, M.J. Khan, S.H. Fan, P.R. Villeneuve, H.A. Haus, J.D. Joannopoulos, Coupling of modes analysis of resonant channel add-drop filters, IEEE Journal of Quantum Electronics, **35** (1999) 1322.

[11] P.B. Clapham, M.C. Hutley, Reduction of lens reflection by moth eye principle, Nature, **244** (1973) 281.

[12] P. Vukusic, J.R. Sambles, Photonic structures in biology, Nature, **424** (2003) 852.

[13] W.L. Min, B. Jiang, P. Jiang, Bioinspired self-cleaning antireflection coatings, Advanced Materials, **20** (2008) 3914.

[14] C.G. Bernhard, W.H. Miller, A corneal nipple pattern in insect compound eyes, Acta Physiologica Scandinavica, **56** (1962) 385.

[15] C.G. Bernhard, G. Gemne, Sallstro.J, Comparative ultrastructure of corneal surface topography in insects with aspects on phylogenesis and function, Zeitschrift Fur Vergleichende Physiologie, **67** (1970) 1.

[16] E. Hecht, Optics, 4th ed., Addison-Wesley, London, 2002.

[17] S. Chattopadhyay, Y.F. Huang, Y.J. Jen, A. Ganguly, K.H. Chen, L.C. Chen, Anti-reflecting and photonic nanostructures, Materials Science & Engineering R-Reports, **69** (2010) 1.

[18] S.L. Diedenhofen, G. Vecchi, R.E. Algra, A. Hartsuiker, O.L. Muskens, G. Immink, E. Bakkers, W.L. Vos, J.G. Rivas, Broad-band and omnidirectional antireflection coatings based on semiconductor nanorods, Advanced Materials, **21** (2009) 973.

[19] J. Krc, M. Zeman, S.L. Luxembourg, M. Topic, Modulated photonic-crystal structures as broadband back reflectors in thin-film solar cells, Applied Physics Letters, **94** (2009) 153501.

[20] D.H. Raguin, G.M. Morris, Analysis of antireflection-structured surfaces with continuous one-dimensional surface profiles, Applied Optics, **32** (1993) 2582.
[21] H.Y. Koo, D.K. Yi, S.J. Yoo, D.Y. Kim, A snowman-like array of colloidal dimers for antireflecting surfaces, Advanced Materials, **16** (2004) 274.
[22] C.H. Chiu, P.C. Yu, H.C. Kuo, C.C. Chen, T.C. Lu, S.C. Wang, S.H. Hsu, Y.J. Cheng, Y.C. Chang, Broadband and omnidirectional antireflection employing disordered GaN nanopillars, Optics Express, **16** (2008) 8748.
[23] J.Q. Xi, M.F. Schubert, J.K. Kim, E.F. Schubert, M.F. Chen, S.Y. Lin, W. Liu, J.A. Smart, Optical thin-film materials with low refractive index for broadband elimination of Fresnel reflection, Nature Photonics, **1** (2007) 176.
[24] W. Zhou, M. Tao, L. Chen, H. Yang, Microstructured surface design for omnidirectional antireflection coatings on solar cells, Journal of Applied Physics, **102** (2007) 103105.
[25] K. Nishioka, T. Sueto, N. Saito, Formation of antireflection nanostructure for silicon solar cells using catalysis of single nano-sized silver particle, Applied Surface Science, **255** (2009) 9504.
[26] S. Wang, X.Z. Yu, H.T. Fan, Simple lithographic approach for subwavelength structure antireflection, Applied Physics Letters, **91** (2007) 061105.
[27] C.H. Sun, P. Jiang, B. Jiang, Broadband moth-eye antireflection coatings on silicon, Applied Physics Letters, **92** (2008) 061112.
[28] P. Spinelli, M.A. Verschuuren, A. Polman, Broadband omnidirectional antireflection coating based on subwavelength surface Mie resonators, Nature Communications, **3** (2012) 692.
[29] Q. Chen, G. Hubbard, P.A. Shields, C. Liu, D.W.E. Allsopp, W.N. Wang, S. Abbott, Broadband moth-eye antireflection coatings fabricated by low-cost nanoimprinting, Applied Physics Letters, **94** (2009) 263118.
[30] B.S. Kim, W.K. Ju, M.W. Lee, S.G. Lee, O. Beom-Hoan, Optimized process of metal assisted silicon wet etching for antireflection layer, Microelectronic Engineering, **98** (2012) 395.
[31] G.-R. Lin, Y.-C. Chang, E.-S. Liu, H.-C. Kuo, H.-S. Lin, Low refractive index Si nanopillars on Si substrate, Applied Physics Letters, **90** (2007) 181923.
[32] C.T. Wu, F.H. Ko, C.H. Lin, Self-organized tantalum oxide nanopyramidal arrays for antireflective structure, Applied Physics Letters, **90** (2007) 171911.
[33] H. Sai, H. Fujii, K. Arafune, Y. Ohshita, M. Yamaguchi, Y. Kanamori, H. Yugami, Antireflective subwavelength structures on crystalline Si fabricated using directly formed anodic porous alumina masks, Applied Physics Letters, **88** (2006) 201116.
[34] A.P. Li, F. Muller, A. Birner, K. Nielsch, U. Gosele, Hexagonal pore arrays with a 50-420 nm interpore distance formed by self-organization in anodic alumina, Journal of Applied Physics, **84** (1998) 6023.
[35] Y.J. Lee, D.S. Ruby, D.W. Peters, B.B. McKenzie, J.W.P. Hsu, ZnO nanostructures as efficient antireflection layers in solar cells, Nano Letters, **8** (2008) 1501.

[36] J. Zhu, Z.F. Yu, G.F. Burkhard, C.M. Hsu, S.T. Connor, Y.Q. Xu, Q. Wang, M. McGehee, S.H. Fan, Y. Cui, Optical Absorption Enhancement in Amorphous Silicon Nanowire and Nanocone Arrays, Nano Letters, **9** (2009) 279.
[37] Y.M. Song, S.J. Jang, J.S. Yu, Y.T. Lee, Bioinspired Parabola Subwavelength Structures for Improved Broadband Antireflection, Small, **6** (2010) 984.
[38] Y.F. Huang, S. Chattopadhyay, Y.J. Jen, C.Y. Peng, T.A. Liu, Y.K. Hsu, C.L. Pan, H.C. Lo, C.H. Hsu, Y.H. Chang, C.S. Lee, K.H. Chen, L.C. Chen, Improved broadband and quasi-omnidirectional anti-reflection properties with biomimetic silicon nanostructures, Nature Nanotechnology, **2** (2007) 770.
[39] J. Park, S. Yoon, K. Kang, S. Jeon, Antireflection behavior of multidimensional nanostructures patterned using a conformable elastomeric phase mask in a single exposure step, Small, **6** (2010) 1981.
[40] S.J. Oh, S. Chhajed, D.J. Poxson, J. Cho, E.F. Schubert, S.J. Tark, D. Kim, J.K. Kim, Enhanced broadband and omni-directional performance of polycrystalline Si solar cells by using discrete multilayer antireflection coatings, Optics Express, **21** (2013) A157.
[41] J.H. Zhao, A.H. Wang, P. Campbell, M.A. Green, 22.7% efficient silicon photovoltaic modules with textured front surface, IEEE Transactions on Electron Devices, **46** (1999) 1495.
[42] P. Campbell, M.A. Green, Light trapping properties of pyramidally textured surfaces, Journal of Applied Physics, **62** (1987) 243.
[43] C.H. Henry, Limiting efficiencies of ideal single and multiple energy-gap terrestrial solar-cells, Journal of Applied Physics, **51** (1980) 4494.
[44] M.A. Green, The Path to 25% Silicon Solar Cell Efficiency: History of Silicon Cell Evolution, Progress in Photovoltaics, **17** (2009) 183.
[45] J. Zhu, C.M. Hsu, Z.F. Yu, S.H. Fan, Y. Cui, Nanodome solar cells with efficient light management and self-cleaning, Nano Letters, **10** (2010) 1979.
[46] T.-G. Chen, P. Yu, Y.-L. Tsai, C.-H. Shen, J.-M. Shieh, M.-A. Tsai, H.-C. Kuo, Nano-patterned glass superstrates with different aspect ratios for enhanced light harvesting in a-Si:H thin film solar cells, Optics Express, **20** (2012) A412.
[47] I.P. Parkin, R.G. Palgrave, Self-cleaning coatings, Journal of Materials Chemistry, **15** (2005) 1689.
[48] R. Blossey, Self-cleaning surfaces - virtual realities, Nature Materials, **2** (2003) 301.
[49] B.G. Prevo, E.W. Hon, O.D. Velev, Assembly and characterization of colloid-based antireflective coatings on multicrystalline silicon solar cells, Journal of Materials Chemistry, **17** (2007) 791.
[50] P. Forbes, Self-cleaning materials, Scientific American, **August** (2008) 88.
[51] R. Wang, K. Hashimoto, A. Fujishima, M. Chikuni, E. Kojima, A. Kitamura, M. Shimohigoshi, T. Watanabe, Light-induced amphiphilic surfaces, Nature, **388** (1997) 431.
[52] Y.F. Li, J.H. Zhang, S.J. Zhu, H.P. Dong, F. Jia, Z.H. Wang, Z.Q. Sun, L. Zhang, Y. Li, H.B. Li, W.Q. Xu, B. Yang, Biomimetic surfaces for high-performance optics, Advanced Materials, **21** (2009) 4731.

[53] R. Furstner, W. Barthlott, C. Neinhuis, P. Walzel, Wetting and self-cleaning properties of artificial superhydrophobic surfaces, Langmuir, **21** (2005) 956.
[54] R.N. Wenzel, Resistance of solid surfaces to wetting by water, Industrial and Engineering Chemistry, **28** (1936) 988.
[55] A.B.D. Cassie, S. Baxter, Wettability of porous surfaces, Transactions of the Faraday Society, **40** (1944) 0546.
[56] Y. Kwon, N. Patankar, J. Choi, J. Lee, Design of Surface Hierarchy for Extreme Hydrophobicity, Langmuir, **25** (2009) 6129.
[57] X.Y. Ling, I.Y. Phang, G.J. Vancso, J. Huskens, D.N. Reinhoudt, Stable and Transparent Superhydrophobic Nanoparticle Films, Langmuir, **25** (2009) 3260.
[58] C. Dorrer, J. Ruhe, Some thoughts on superhydrophobic wetting, Soft Matter, **5** (2009) 51.
[59] X. Zhang, F. Shi, J. Niu, Y.G. Jiang, Z.Q. Wang, Superhydrophobic surfaces: from structural control to functional application, Journal of Materials Chemistry, **18** (2008) 621.
[60] P. Roach, N.J. Shirtcliffe, M.I. Newton, Progess in superhydrophobic surface development, Soft Matter, **4** (2008) 224.
[61] F. Shi, X.X. Chen, L.Y. Wang, J. Niu, J.H. Yu, Z.Q. Wang, X. Zhang, Roselike microstructures formed by direct in situ hydrothermal synthesis: From superhydrophilicity to superhydrophobicity, Chemistry of Materials, **17** (2005) 6177.
[62] C.H. Xue, S.T. Jia, J. Zhang, L.Q. Tian, Superhydrophobic surfaces on cotton textiles by complex coating of silica nanoparticles and hydrophobization, Thin Solid Films, **517** (2009) 4593.
[63] W. Ming, D. Wu, R. van Benthem, G. de With, Superhydrophobic films from raspberry-like particles, Nano Letters, **5** (2005) 2298.
[64] S.S. Latthe, H. Imai, V. Ganesan, A.V. Rao, Superhydrophobic silica films by sol-gel co-precursor method, Applied Surface Science, **256** (2009) 217.
[65] Z.X. Li, Y.J. Xing, J.J. Dai, Superhydrophobic surfaces prepared from water glass and non-fluorinated alkylsilane on cotton substrates, Applied Surface Science, **254** (2008) 2131.
[66] B.X. Leng, Z.Z. Shao, G. de With, W.H. Ming, Superoleophobic Cotton Textiles, Langmuir, **25** (2009) 2456.
[67] B. Xu, Z.S. Cai, Fabrication of a superhydrophobic ZnO nanorod array film on cotton fabrics via a wet chemical route and hydrophobic modification, Applied Surface Science, **254** (2008) 5899.
[68] Y.B. Park, H. Im, M. Im, Y.K. Choi, Self-cleaning effect of highly water-repellent microshell structures for solar cell applications, Journal of Materials Chemistry, **21** (2011) 633.
[69] C.H. Xue, S.T. Jia, J. Zhang, J.Z. Ma, Large-area fabrication of superhydrophobic surfaces for practical applications: an overview, Science and Technology of Advanced Materials, **11** (2010) 033002.
[70] C.P. Collier, R.J. Saykally, J.J. Shiang, S.E. Henrichs, J.R. Heath, Reversible tuning of silver quantum dot monolayers through the metal-insulator transition, Science, **277** (1997) 1978.

[71] C.M. Hsu, S.T. Connor, M.X. Tang, Y. Cui, Wafer-scale silicon nanopillars and nanocones by Langmuir-Blodgett assembly and etching, Applied Physics Letters, **93** (2008) 133109.
[72] S.H. Ahn, L.J. Guo, Large-Area Roll-to-Roll and Roll-to-Plate Nanoimprint Lithography: A Step toward High-Throughput Application of Continuous Nanoimprinting, ACS Nano, **3** (2009) 2304.
[73] K.J. Morton, G. Nieberg, S.F. Bai, S.Y. Chou, Wafer-scale patterning of sub-40 nm diameter and high aspect ratio (> 50 : 1) silicon pillar arrays by nanoimprint and etching, Nanotechnology, **19** (2008) 345301.
[74] A. Nakajima, K. Hashimoto, T. Watanabe, K. Takai, G. Yamauchi, A. Fujishima, Transparent superhydrophobic thin films with self-cleaning properties, Langmuir, **16** (2000) 7044.
[75] J. Zimmermann, F.A. Reifler, U. Schrade, G.R.J. Artus, S. Seeger, Long term environmental durability of a superhydrophobic silicone nanofilament coating, Colloids and Surfaces a-Physicochemical and Engineering Aspects, **302** (2007) 234.
[76] N. Yamada, T. Ijiro, E. Okamoto, K. Hayashi, H. Masuda, Characterization of antireflection moth-eye film on crystalline silicon photovoltaic module, Optics Express, **19** (2011) A118.
[77] F. Xia, L. Jiang, Bio-inspired, smart, multiscale interfacial materials, Advanced Materials, **20** (2008) 2842.
[78] K.S. Yee, Numerical solution of initial boundary value problems involving maxwells equations in isotropic media, IEEE Transactions on Antennas and Propagation, **AP14** (1966) 302.
[79] A.F. Oskooi, D. Roundy, M. Ibanescu, P. Bermel, J.D. Joannopoulos, S.G. Johnson, MEEP: A flexible free-software package for electromagnetic simulations by the FDTD method, Computer Physics Communications, **181** (2010) 687.
[80] C. Oh, M.J. Escuti, Time-domain analysis of periodic anisotropic media at oblique incidence: an efficient FDTD implementation, Optics Express, **14** (2006) 11870.
[81] http://ab-initio.mit.edu/wiki/index.php/Meep
[82] J. Siejka, C. Ortega, O-18 study of field-assisted pore formation in compact anodic oxide-films on aluminum, Journal of the Electrochemical Society, **124** (1977) 883.
[83] F.Y. Li, L. Zhang, R.M. Metzger, On the growth of highly ordered pores in anodized aluminum oxide, Chemistry of Materials, **10** (1998) 2470.
[84] E. Thienot, F. Domingo, E. Cambril, C. Gosse, Reactive ion etching of glass for biochip applications: Composition effects and surface damages, Microelectronic Engineering, **83** (2006) 1155.
[85] P.W. Leech, Reactive ion etching of quartz and silica-based glasses in CF4/CHF3 plasmas, Vacuum, **55** (1999) 191.
[86] J.H. Park, N.E. Lee, J. Lee, J.S. Park, H.D. Park, Deep dry etching of borosilicate glass using SF6 and SF6/Ar inductively coupled plasmas, Microelectronic Engineering, **82** (2005) 119.
[87] K. Emery, Measurement and Characterization of Solar Cells and Modules, in Handbook of Photovoltaic Science and Engineering, in: Handbook of Photovoltaic Science and Engineering, John Wiley & Sons, Ltd, Chichester, UK., 2005.
[88] http://www.astm.org/

[89] J.P. Berenger, Perfectly matched layer for the FDTD solution of wave-structure interaction problems, IEEE Transactions on Antennas and Propagation, **44** (1996) 110.
[90] H. Xu, N. Lu, D. Qi, J. Hao, L. Gao, B. Zhang, L. Chi, Biomimetic Antireflective Si Nanopillar Arrays, Small, **4** (2008) 1972.
[91] M. Tao, W. Zhou, H. Yang, L. Chen, Surface texturing by solution deposition for omnidirectional antireflection, Applied Physics Letters, **91** (2007) 081118.
[92] P. Lalanne, G.M. Morris, Antireflection behavior of silicon subwavelength periodic structures for visible light, Nanotechnology, **8** (1997) 53.
[93] J.Y. Liang, H. Chik, A.J. Yin, J. Xu, Two-dimensional lateral superlattices of nanostructures: Nonlithographic formation by anodic membrane template, Journal of Applied Physics, **91** (2002) 2544.
[94] J.D. Plummer, M.D. Deal, P.B. Griffin, Silicon VLSI Technology - Fundamentals, Practice and Modeling, Prentice Hall, 2000.
[95] S. Grigoropoulos, E. Gogolides, A.D. Tserepi, A.G. Nassiopoulos, Highly anisotropic silicon reactive ion etching for nanofabrication using mixtures of SF6/CHF3 gases, Journal of Vacuum Science & Technology B, **15** (1997) 640.
[96] Y.H. Xiu, S. Zhang, V. Yelundur, A. Rohatgi, D.W. Hess, C.P. Wong, Superhydrophobic and low light reflectivity silicon surfaces fabricated by hierarchical etching, Langmuir, **24** (2008) 10421.
[97] M. Manca, A. Cannavale, L. De Marco, A.S. Arico, R. Cingolani, G. Gigli, Durable superhydrophobic and antireflective surfaces by trimethylsilanized silica nanoparticles-based sol-gel processing, Langmuir, **25** (2009) 6357.
[98] D. Lee, M.F. Rubner, R.E. Cohen, All-nanoparticle thin-film coatings, Nano Letters, **6** (2006) 2305.
[99] T. Verho, C. Bower, P. Andrew, S. Franssila, O. Ikkala, R.H.A. Ras, Mechanically durable superhydrophobic surfaces, Advanced Materials, **23** (2011) 673.
[100] Y.H. Xiu, Y. Liu, D.W. Hess, C.P. Wong, Mechanically robust superhydrophobicity on hierarchically structured Si surfaces, Nanotechnology, **21** (2010) 155705.
[101] J. Son, L.K. Verma, A.J. Danner, C.S. Bhatia, H. Yang, Enhancement of optical transmission with random nanohole structures, Optics Express, **19** (2011) A35.
[102] L.K. Verma, M. Sakhuja, J. Son, A.J. Danner, H. Yang, H.C. Zeng, C.S. Bhatia, Self-cleaning and antireflective packaging glass for solar modules, Renewable Energy, **36** (2011) 2489.
[103] N. Satyanarayana, S.K. Sinha, Tribology of PFPE overcoated self-assembled monolayers deposited on Si surface, Journal of Physics D-Applied Physics, **38** (2005) 3512.
[104] D. Quere, Wetting and roughness, Annual Review of Materials Research, **38** (2008) 71.
[105] X.M. Li, D. Reinhoudt, M. Crego-Calama, What do we need for a superhydrophobic surface? A review on the recent progress in the preparation of superhydrophobic surfaces, Chemical Society Reviews, **36** (2007) 1350.

[106] O.L. Muskens, S.L. Diedenhofen, M.H.M. van Weert, M.T. Borgstrom, E. Bakkers, J.G. Rivas, Epitaxial growth of aligned semiconductor nanowire metamaterials for photonic applications, Advanced Functional Materials, **18** (2008) 1039.
[107] http://app2.nea.gov.sg/weather_statistics.aspx
[108] M. Miwa, A. Nakajima, A. Fujishima, K. Hashimoto, T. Watanabe, Effects of the surface roughness on sliding angles of water droplets on superhydrophobic surfaces, Langmuir, **16** (2000) 5754.
[109] A.K. Gnanappa, C. O'Murchu, O. Slattery, F. Peters, T. O'Hara, B. Aszalós-Kiss, S.A.M. Tofail, Improved aging performance of vapor phase deposited hydrophobic self-assembled monolayers, Applied Surface Science, **257** (2011) 4331.
[110] B.E.A. Saleh, M.C. Teich, Fundamentals of Photonics, second ed., Wiley, Hoboken, 2007.
[111] Z.Y. Zeng, X. Huang, Z.Y. Yin, H. Li, Y. Chen, Q. Zhang, J. Ma, F. Boey, H. Zhang, Fabrication of Graphene Nanomesh by Using an Anodic Aluminum Oxide Membrane as a Template, Advanced Materials, **24** (2012) 4138.
[112] J. Zou, X.Y. Qi, L.W. Tan, B.J.H. Stadler, Large-scale ordering of porous Si using anodic aluminum oxide grown by directed self-assembly, Applied Physics Letters, **89** (2006) 093106.
[113] H.P. Wang, K.T. Tsai, K.Y. Lai, T.C. Wei, Y.L. Wang, J.H. He, Periodic Si nanopillar arrays by anodic aluminum oxide template and catalytic etching for broadband and omnidirectional light harvesting, Optics Express, **20** (2012) A94.
[114] S. Shukla, K.T. Kim, A. Baev, Y.K. Yoon, N.M. Litchinitser, P.N. Prasad, Fabrication and Characterization of Gold-Polymer Nanocomposite Plasmonic Nanoarrays in a Porous Alumina Template, ACS Nano, **4** (2010) 2249.
[115] H. Masuda, H. Yamada, M. Satoh, H. Asoh, M. Nakao, T. Tamamura, Highly ordered nanochannel-array architecture in anodic alumina, Applied Physics Letters, **71** (1997) 2770.
[116] F. Zacharatos, V. Gianneta, A.G. Nassiopoulou, Highly ordered hexagonally arranged nanostructures on silicon through a self-assembled silicon-integrated porous anodic alumina masking layer, Nanotechnology, **19** (2008) 495306.
[117] C.J. Yang, S.W. Liang, P.W. Wu, C. Chen, J.M. Shieh, Fabrication of anodic aluminum oxide film on large-area glass substrate, Electrochemical and Solid State Letters, **10** (2007) C69.
[118] J. Son, L.K. Verma, A.J. Danner, C.S. Bhatia, H. Yang, Enhancement of optical transmission with random nanohole structures, Optics Express, **19** (2011) A35.
[119] M. Sakhuja, J. Son, L.K. Verma, H. Yang, C.S. Bhatia, A.J. Danner, Omnidirectional study of nanostructured glass packaging for solar modules, Prog. Photovolt: Res. Appl., **doi: 10.1002/pip.2276** (2012).
[120] H.B.T. Li, R.H. Franken, J.K. Rath, R.E.I. Schropp, Structural defects caused by a rough substrate and their influence on the performance of hydrogenated nano-crystalline silicon n-i-p solar cells, Solar Energy Materials and Solar Cells, **93** (2009) 338.

APPENDIX I: MEEP Script

```
;---------------define the paremeters ----------------------------------------
(reset-meep)
(use-output-directory)
;-- source setting
(define-param aaa 1)
(define-param wl 555)
(define-param fcen (/ aaa wl))
(define-param df 0.0018);300nm to 700nm
(define-param source-component Ez)
(define-param nfreq 500)
(define-param theta_deg 0)
; -- total structure
(define-param dpml 1)
(define-param y_spacer 30)
(define-param ne_spacer (* -1 y_spacer))
(define-param sx 30)
(define-param sy (+ (* 2 dpml) (* 6 y_spacer)))
(define-param sz 30)
 (define-param t_ox 9) ; // 0.003 - 0.018 // 0.05-0.35
 (define-param peri 30)
(define-param res 3); 10/10? = 1nm 1000/35 = 28.57nm 1000/25 = 40nm
;-- substrate - silicon
(define sio2 (make dielectric (epsilon (* 1.46 1.46))))
(define al2o3 (make dielectric (epsilon (* 1.78 1.78))))
;-- other settings
(define-param ref? false)
;-- source tilting
(define ((pw-amp k x0) x)
 (exp (* 0+1i (vector3-dot k (vector3+ x x0)))) ) ;exp[ik(x+x0)] k has direction
and according to c=1, k=lambda
(define theta_rad (/ (* pi theta_deg) 180)) ;x0 = (0 ? 0)
(define-param kdir (vector3 (sin theta_rad) (cos theta_rad)))
(define k (vector3-scale (* 2 pi fcen) (unit-vector3 kdir)))
;--------------------set the necessary parameters-----------------------------------?
(set! k-point (vector3 0 0 0))
(set! ensure-periodicity true)
(set! pml-layers (list (make pml (thickness dpml)(direction Y) )))
(set-param! resolution res)
;--------------------define the computational cell size-----------------------------
(set! geometry-lattice (make lattice (size sx sy sz)))
;--------------------define the structure(surface aspect ratio)----------------------
(if (not ref?)
(set! geometry
 (append
; (geometric-objects-duplicates (vector3 peri 0) 0 (/ sx peri)
 (list
          (make block
```

```
        ;(center (* -0.5 sx) (+ (* 0.5 t_gpn) (* 0.5 t_ox) ne_spacer))
        (center 0 (+ (* 0.5 t_gpn) (* 0.5 t_ox) ne_spacer) 0)
        (size sx t_ox sz)
        ;(size sx t_ox)
        (material al2o3))

        ;(make block
        ;(center (* -0.5 sx) (- (* -0.25 sy) (* 0.5 (+ t_ox t_gpn (* 0.5 h_au))) ))
        ;(center 0 (- (* -0.25 sy) (* 0.5 (+ t_ox t_gpn (* 0.5 h_au))) ))
        ;(size peri (- (* 0.5 sy) (* 0.5 h_au) t_ox t_gpn))
        ;(size sx (- (* 0.5 sy) (* 0.5 h_au) t_ox t_gpn))
        ;(material mysio2)) )))))
))));)
;--------------------source setting -------------------------------------
(set! sources
 (list
 (make source
        (src (make gaussian-src (frequency fcen) (fwidth df) ))
        (component source-component)
        (center 0 (* 2 y_spacer) 0)
        (size sx 0 sz)
;       (amp-func (pw-amp k (vector3 0 (* 2 y_spacer) )))
)))
;--------------------detecting point? -------------------------------------
(define det_m1 (add-flux fcen df nfreq (make flux-region
        (center 0 (* -2 y_spacer) 0)
        (direction Y)
        (size sx 0 sz) )))
(define det_p1 (add-flux fcen df nfreq (make flux-region
        (center 0 y_spacer 0)
        (direction Y)
        (size sx 0 sz) )))
 (if ref?
 (run-sources+
 (stop-when-fields-decayed 500 source-component (vector3 0 (* -2 y_spacer)
0) 1e-3))
 (run-sources+
 (stop-when-fields-decayed 500 source-component (vector3 0 (* -2 y_spacer)
0) 1e-3)
 (at-beginning output-epsilon)
 ;(at-every 10 (output-png source-component "-c dkbluered")) ))
))(display-fluxes det_p1 det_m1)
;------------------------ END -------------------------------
```

APPENDIX II: Publications

[1] Jaesung Son, Mridul Sakhuja, Aaron J. Danner, Chranjit S. Bhatia, and Hyunsoo Yang, “Large scale antireflective glass texturing using grid contacts in anodization methods,” Solar energy materials and solar cells **116** 9-13 (2013)

[2] Mridul Sakhuja, Jaesung Son, Lalit K. Verma, Hyunsoo Yang, Charanjit S. Bhatia, Aaron J. Danner. “Omnidirectional study of nanostructured glass packaging for solar modules” Progress in photovoltaics, on-line early published. (2012)

[3] Jaesung Son, Shreya Kundu, Lalit K. Verma, Mridul Sakhuja, Aaron J. Danner, Charanjit S. Bhatia, and Hyunsoo Yang, “A practical superhydrophilic self cleaning and anti-reflective surface for outdoor photovoltaic applications,” Solar energy materials and solar cells **98** 46-51 (2011)

[4] Lalit K. Verma, Mridul Sakhuja, Jaesung Son, Aaron J. Danner, Hyunsoo Yang, and Charanjit S. Bhatia, “Self-cleaning and antireflective packaging glass for solar modules,” Renewable energy **36** 2489-2493 (2011)

[5] Jaesung Son, Lalit K. Verma, Aaron J. Danner, Charanjit S. Bhatia, and Hyunsoo Yang, "Enhancement of optical transmission with random nanohole structures," Optics Express **19** A35-A40 (2010)

[6] Jaesung Son, Lalit K. Verma, Aaron J. Danner, Charanjit S. Bhatia, and Hyunsoo Yang, “Omnidirectional optical transmission by optimized structures of solar cells,” Proc. 35th IEEE PVSC 1577 (2010)